

AD-A285 622

Dist: A
ATION PAGEForm Approved
OMB No. 0704-0188

①

average 1 hour per response, including the time for reviewing instructions, searching existing data sources, ing the collection of information. Send comments regarding this burden estimate or any other aspect of this 1. to Washington Headquarters Services, Directorate for Information Operations and Reports, 1215 Jefferson of Management and Budget, Paperwork Reduction Project (0704-0188), Washington, DC 20503

1. AGENCY USE ONLY (Leave blank)		2. REPORT DATE 14 JUL 94		3. REPORT TYPE AND DATES COVERED Final Report - 15 DEC 90 - 14 MAY 94	
4. TITLE AND SUBTITLE Computational Studies of Laminar to Turbulence Transition				5. FUNDING NUMBERS PE - 61102F PR - 2307 SA - BS C - 0014 F49620-91- C-0014	
6. AUTHOR(S) Mujeeb R. Malik & Fei Li				8. PERFORMING ORGANIZATION REPORT NUMBER HTC-FR-9405 AFOSR-TR- 94 0645	
7. PERFORMING ORGANIZATION NAME(S) AND ADDRESS(ES) High Technology Corporation 28 Research Drive Hampton, VA 23666				10. SPONSORING/MONITORING AGENCY REPORT NUMBER F49620-91- C-0014	
9. SPONSORING/MONITORING AGENCY NAME(S) AND ADDRESS(ES) AFOSR/NA Building 410 Bolling AFB, DC 20032-6448				11. SUPPLEMENTARY NOTES N/A DTIC OCT 20 1994 D	
12a. DISTRIBUTION/AVAILABILITY STATEMENT Approved for public release; distribution is unlimited. DTIC QUALIFIED TO BE RELEASED				12b. DISTRIBUTION CODE 132A 94-32623 A 	
13. ABSTRACT (Maximum 200 words) Nonlinear evolution of Görtler and crossflow vortices is investigated. The associated secondary instabilities of these streamwise vortices are also studied. The Görtler vortex is found to be subject to two types of secondary modes: a sinuous mode and a varicose mode similar to that observed in the experiments. The growth rate of the sinuous mode is higher initially but the varicose mode becomes more unstable in the downstream. It is also found that crossflow vortices are subject to a high frequency secondary instability prior to breakdown, as found in experiments performed on swept wings. In agreement with the experiments, our calculations show that the frequency of this secondary instability, which resides on top of the crossflow vortex, is an order of magnitude higher than the frequency of the most amplified traveling crossflow disturbances. The interaction of stationary and traveling disturbances is also considered. These studies have been carried out by using parabolized stability equations (PSE) and a two-dimensional (2D) eigenvalue approach. The mathematical nature of PSE approximation is also discussed					
14. SUBJECT TERMS Gortler vortices, crossflow vortices, secondary instability, parabolized stability equations, 2D eigenvalue problem				15. NUMBER OF PAGES 130	
17. SECURITY CLASSIFICATION OF REPORT Unclassified				18. SECURITY CLASSIFICATION OF THIS PAGE Unclassified	
19. SECURITY CLASSIFICATION OF ABSTRACT Unclassified				20. LIMITATION OF ABSTRACT UL	

TABLE OF CONTENTS

Introduction	1
 Part A. On the Breakdown of Görtler Vortices: Nonlinear Development and Secondary Instabilities	 3
Abstract	4
1. Introduction	4
2. Problem Formulation for Nonlinear Steady and Unsteady Disturbances	6
3. Nonlinear Development of Steady Görtler Vortices	9
4. Linear Inviscid Secondary Instability	13
4.1 Governing Equations	13
4.2 Results of Secondary Instability Calculations.....	14
5. Nonlinear Development of Unsteady Disturbances	17
6. Conclusions	19
References.....	20
 Part B. Crossflow Disturbances in Three-Dimensional Boundary Layers: Nonlinear Development, Wave Interaction and Secondary Instability	 47
Abstract	48
1. Introduction	48
2. The Swept Hiemenz Problem	51
2.1 The Basic Flow	51
3. PSE Analysis for 3D Boundary Layers	53
4. Linear and Nonlinear Stability Analysis and Wave Interaction	56
4.1 Quasi-Parallel Linear Stability	56
4.2 Nonparallel Effects	58
4.3 Nonlinear Development of Stationary Crossflow Vortices	59
4.4 Stationary and Traveling Wave Interaction	61
4.5 Effect of Nonlinear Disturbances on Skin Friction	64
5. High Frequency Secondary Instability.....	65
6. Conclusions	68
References.....	69

Part C. On the Nature of PSE Approximation	109
Abstract	110
1. Introduction	110
2. Mathematical Nature of PSE	114
3. Stability of the Marching Procedure	116
4. Application to Blasius Boundary Layer	119
5. Conclusions	121
References	121

Accession For	
NTIS CRA&I	<input checked="checked" type="checkbox"/>
DTIC TAB	<input type="checkbox"/>
Unannounced	<input type="checkbox"/>
Justification	
By	
Distribution /	
Availability Codes	
Dist	Avail and/or Special
A-1	

COMPUTATIONAL STUDIES OF LAMINAR TO TURBULENCE TRANSITION

Introduction

The subject of laminar/turbulent transition is of fundamental and practical importance in fluid mechanics. An indepth knowledge of transition mechanism is needed not only for boundary/shear layer control but also for understanding of turbulence. Depending upon the state of the boundary layer, various instability mechanisms such as Tollmien-Schlichting (TS), crossflow and Görtler may be operative. The present day transition prediction methodology is based upon linear stability theory in the form of e^N method. This technique works well in a specialized parameter space involving extremely "clean" flows. However, depending upon the flow conditions, various instabilities referred to above could interact. In case of such wave-interactions, the transition prediction methodology, based solely upon linear stability theory, would fail. Therefore, it is of interest to study possible wave interactions and devise new transition prediction criterion under such circumstances.

The early stages of breakdown of Tollmien-Schlichting waves to turbulence in a two-dimensional flat plate boundary layer are now relatively well understood due to careful laboratory experiments, (Klebanoff et al. 1962, Nishioka et al. 1980) ingenious numerical simulations (Zang and Hussaini 1985, Hussaini 1987, Spalart and Yang 1987, Fasel et al. 1987), and analytical studies (Herbert 1988, Kachanov 1987). However, our knowledge of transition mechanism in three-dimensional boundary layers and flow where primary instability mechanism is other than TS is relatively limited.

A swept wing boundary layer or a boundary layer on a body at an angle of attack is susceptible to both crossflow and TS type instabilities. While the former results due to inflectional instability of the crossflow velocity profiles, the latter is a viscous instability of the streamwise profiles. Another boundary-layer where two types of instabilities exist is that formed on a concavely curved plate. Here, counter-rotating steady Görtler vortices form due to centrifugal instability. Given that the Reynolds number is high enough, TS instability may also be present. Nonlinear development of Görtler vortices and Görtler/TS interaction is again a problem of both fundamental and potentially practical importance.

The objective of the present study is to understand physical mechanisms leading to transition and identify any new instability mechanisms involved in these flows. A numerical study is carried out to investigate how a steady Görtler vortex breaks down to turbulence. The study reveals various stages involved including the nonlinear development of Görtler vortex, secondary instabilities leading to the development of unsteadiness and the final breakdown.

In order to investigate crossflow instability, we consider a model swept-wing boundary-layer and study the development of stationary as well as traveling disturbances and their nonlinear interaction. It is also found that prior to laminar-turbulent transition, the three-dimensional boundary

layer is subject to a high-frequency secondary instability, which is in agreement with the experiments.

Two approaches have been used in the above studies. For nonlinear evolution and wave-wave interaction, we utilize parabolized stability equations (PSE). For secondary instability, we employ two-dimensional (2D) eigenvalue approach.

The final report is divided into three parts:

A. On the Breakdown of Görtler Vortices: Nonlinear Development and Secondary Instabilities

This describes nonlinear evolution of Görtler vortices and their breakdown via various secondary instability mechanisms.

B. Crossflow Disturbances in Three-Dimensional Boundary Layers: Nonlinear Development, Wave Interaction and Secondary Instability

This describes nonlinear evolution of crossflow disturbances, wave-wave interaction and a high-frequency secondary instability prior to laminar-turbulent breakdown.

C. On the Nature of PSE Approximation

Since the PSE approach is used in the above physical problems, it is important to investigate the mathematical nature of the approximation. In this part, we explore the parametric boundaries within which PSE approximation is valid and results in a stable numerical solution. This knowledge is used when we employ this approach in the above problems.

References

- Fasel, H. F., Rist, U., and Konzelmann, U., 1987 "Numerical Investigation of the Three-Dimensional Development in Boundary-Layer Transition," AIAA Paper No. 87-1203.
- Herbert, T., 1988 "Secondary Instability of Boundary Layers," *Ann. Rev. Fluid Mech.* **20**, pp. 487-526.
- Hussaini, M. Y., 1987 "Stability, Transition and Turbulence," Supercomputing in Aerospace, NASA CP 2454, pp. 211-220.
- Kachanov, Y. S., 1987 "On the Resonant Nature of the Breakdown of a Laminar Boundary Layer," *J. Fluid Mech.* **184**, pp. 43-74.
- Klebanoff, P. S., Tidstrom, K. D., and Sargent, L. M., 1962 "The Three-Dimensional Nature of Boundary-Layer Instability," *J. Fluid Mech.* **12**, pp. 1-34.
- Nishioka, M., Asai, M., Iida, S., 1980 "An Experimental Investigation of Secondary Instability," Laminar-Turbulent Transition, ed. R. Eppler, H. Fasel, pp. 37-46, Berlin: Springer-Verlag.
- Spalart, P. R. and Yang, K. S., 1987 "Numerical Simulation of Ribbon-Induced Transition in Blasius Flow," *J. Fluid Mech.* **178**, pp. 345-365.
- Zang, T. A. and Hussaini, M. Y., 1985 "Numerical Experiments on Subcritical Transition Mechanisms," AIAA Paper No. 85-0296.

PART A.

**On the Breakdown of Görtler Vortices: Nonlinear Development
and Secondary Instabilities**

Abstract

Nonlinear development of stationary Görtler vortices in an incompressible boundary layer is studied by solving the parabolic partial differential equations. It is found that due to the pumping action of the steady counter-rotating vortices, wall shear stress decreases rapidly in the peak plane but, unlike the result of Hall (1990), it does not go to zero and there is no flow reversal. Instead, as the Görtler vortex saturates the mean flow correction mode dominates and causes the wall shear in the peak plane to begin to rise again. A highly distorted mean flow field is set up due to the vortex action where the streamwise velocity \bar{u} depends strongly not only on y (wall normal) but also on the z (spanwise) coordinate. The inviscid instability of this flow field is analyzed by solving the two-dimensional eigenvalue problem associated with the governing partial differential equation. It is found that the flow field is subject to odd and even (with respect to the Görtler vortex) unstable modes. The odd mode which was also found by Hall & Horseman (1991) is initially more unstable. However, there exists an even mode which has higher growth rate further downstream. The nonlinear development of these secondary instability modes is studied by solving the (viscous) partial differential equations under a parabolizing approximation. The odd mode leads to the well-known sinuous mode of breakdown while the even mode leads to the horse-shoe type vortex structure. This helps explain experimental observations that Görtler vortices breakdown sometimes by sinuous motion and sometime by developing a horse-shoe vortex structure. The details of these breakdown mechanisms are presented.

1. Introduction

Two-dimensional boundary-layer flow over a concavely curved wall is subject to Görtler instability due to the action of centrifugal force and results in the formation of counter-rotating streamwise vortices. Görtler vortices play a dominant role in boundary-layer transition in many aerodynamic flows such as on turbine blades and supersonic nozzle walls (e.g., Beckwith et al. 1984). Due to their technological importance, Görtler vortices have been the subject of a number of investigations (for a recent review, see Floryan, 1991). Görtler vortices are steady and the question how they might breakdown to turbulent motion is a problem of fundamental interest in fluid mechanics. This problem may also serve as a model for the longitudinal vortices in turbulent boundary layers. In this work, we will study the nonlinear development of Görtler vortices, their linear secondary instability characteristics and the nonlinear growth of two important modes of secondary instability up to the breakdown stage.

Experimental investigations have revealed two distinct types of secondary instabilities when the primary instability (the Görtler vortex) is sufficiently developed. Bippes (1978) made detailed observations of the Görtler vortex breakdown using the hydrogen-bubble visualization technique in

the Görtler number (G_θ) range of approximately 3 to 9 (based upon momentum thickness θ) where G_θ is defined as

$$G_\theta = R_\theta \sqrt{\theta |\kappa^\dagger|}, \quad (1.1)$$

κ^\dagger being the surface curvature and R_θ the Reynolds number based upon momentum thickness. Bippes found that the initial amplification of the Görtler vortices agreed with linear theory and, later, sinuous oscillations developed, which ultimately led to turbulence. Aihara & Koyama (1981) conducted flow visualization studies as well as hot-wire measurements of Görtler vortices in Görtler number (G_θ) range between 7.7 and 15. They found that a different type of secondary instability, i.e., the horse-shoe vortex type (also called the varicose instability), was responsible for transition. Ito (1985) also found this symmetric mode of breakdown in his experiment conducted in the Görtler number range between 5.5 and 12.4. Swearingen & Blackwelder (1987) (referred to as SB hereafter) studied the Görtler vortices using smoke-wire and hot-wire techniques in the Görtler number range between 0.5 and 10. They observed that both the sinuous and the horse-shoe types of secondary instabilities were present in the transition process and found that the sinuous mode was the stronger of the two. In their experiment, the unsteady secondary instability fluctuations correlated better with the spanwise velocity gradients than with the normal velocity gradient. Unsteady motion in Görtler vortices was also observed by Peerhossaini & Wesfried (1988).

Numerical simulations were carried out by a number of researchers for Görtler vortices under the same conditions as the experiment of SB. Sabry & Liu (1991) studied the key features of steady Görtler vortex development by using a temporal analogy in which the growth of time-dependent streamwise vortices are related to the spatial case through a chosen advection velocity. Good agreements with SB were found before the unsteady oscillations became important. Liu & Domaradzki (1993) used a similar approach and analyzed the steady and unsteady nonlinear evolution of Görtler vortices. Temporal Navier-Stokes approach was earlier used by Malik (1986) and Malik & Hussaini (1990) to study Görtler/Tollmien-Schlichting wave interaction. Since the physical problem is spatial, temporal approach can, at best, provide qualitative results and there is no a priori justification for this approximation. Spatial simulations of the Görtler vortex were performed by Hall (1988, 1990) and by Hall & Horseman (1991). Agreement with the experiment of SB was obtained for the early stages of Görtler vortex development. However, Hall (1990) and Hall & Horseman (1991) found that the wall-shear in the "peak-plane" crossed zero to become negative at some downstream location, indicating the existence of a region of reverse flow. They attributed the rise in wall-shear in the experiment of SB to the nonlinear interaction of unsteady oscillations and the steady Görtler vortex. However, spatial calculations carried out by Lee & Liu (1992) did not find any flow reversal.

Various theoretical attempts at the secondary instability of the Görtler vortex illuminated the important role the sinuous and the varicose modes play in transition to turbulence. Sabry, Yu & Liu (1990) used 1-dimensional local inflectional velocity profiles to analyze the secondary instability characteristics of Görtler vortices and found that the sinuous type disturbance would prevail over the varicose type. Hall & Horseman (1991) derived a partial differential equation governing the inviscid secondary instability for a mean flow which varied strongly in two directions. They identified the 2-dimensional odd and even eigenfunctions of this equation as representing the sinuous and varicose types of secondary instability of Görtler vortex, respectively. They also found that the odd mode grows faster than the even mode. In the numerical simulation of Liu & Domaradzki (1993), the sinuous mode was also found to be stronger than the varicose mode. Secondary instability analysis of Görtler and crossflow disturbances was made by Malik and Li (1993a).

All these numerical investigations of secondary instability seem to point to one fact, i.e., the sinuous mode is the dominant mode and is chiefly responsible for the transition to turbulence. Why do some experiments (e.g., Aihara & Koyama, 1981) show the presence of only the varicose mode? Examining the above cited numerical results closely, we find that most of these calculations were carried out for either a limited range of wavelengths or a limited number of streamwise locations. In Hall & Horseman (1991), for example, the secondary instability calculations were computed almost exclusively at $x = 100$ cm. In Liu & Domaradzki (1993), the computational box had streamwise dimension of either 2 cm or 2.2 cm, which essentially fixed the streamwise wavelength. Furthermore, a comparison of the "mushroom" structure obtained by Hall & Horseman (1991) on the one hand and Lee & Liu (1992) and Liu & Domaradzki (1993) on the other shows that the basic flow state used for secondary instability computations are different. In the results of Hall & Horseman (1991), the "mushroom" lacks the very thin "stem" shown in the results of other researchers.

In this paper, we will first study the nonlinear development of the Görtler vortex and analyze various modes of secondary instability. Rayleigh's criterion for the inviscid instability of one-dimensional velocity profile is well-known. However, its extension to two-dimensional flow has not been considered. We will, therefore, derive a necessary condition for inviscid instability of mean flows which strongly depend upon two space variables. We also study nonlinear evolution of the secondary instability modes using parabolized stability equations (PSE). Section 2 describes the parabolized stability equation formulation which describes all stages of the vortex development. Section 3 deals with the nonlinear development of steady Görtler vortices while sections 4 & 5 analyzes the linear secondary instability and its nonlinear evolution, respectively.

2. Problem Formulation for Nonlinear Steady and Unsteady Disturbances

We consider a two-dimensional zero pressure gradient boundary-layer flow over a concave surface whose constant radius of curvature $r^\dagger = 1/\kappa^\dagger$. The streamwise, wall-normal and the

spanwise coordinates are denoted as $x = X / \ell_0$, $y = Y / \ell_0$ and $z = Z / \ell_0$, respectively ($y = 0$ denotes the wall), where the length scale ℓ_0 will be prescribed later.

Let the x , y and z components of the velocity and pressure be given by

$$(u^\dagger, v^\dagger, w^\dagger) = U_\epsilon \{U(x, y) + u(x, y, z, t), V(x, y) + v(x, y, z, t), 0 + w(x, y, z, t)\}$$

$$p^\dagger = \rho U_\epsilon^2 (P + p(x, y, z, t))$$

where the superscript \dagger represents a dimensional quantity and U_ϵ is the velocity scale. Here U and V are mean flow velocity components obtained by solving the Blasius equation whereas u , v , w represent the perturbation velocity components in x , y , z directions, respectively. Similarly, P and p represent the mean and perturbation pressures. We assume that Reynolds number, R , is large and that the radius of curvature is much larger than the boundary-layer thickness, δ (i.e., $k^\dagger \delta \ll 1$). In this case, if $\kappa = \kappa^\dagger \ell_0$, the equations governing the perturbation quantities are

$$\frac{\partial u}{\partial t} + U \frac{\partial u}{\partial x} + u \frac{\partial U}{\partial x} + V \frac{\partial u}{\partial y} + v \frac{\partial U}{\partial y} + \kappa(Uv + Vu) + \frac{\partial p}{\partial x} - \frac{1}{R} \nabla^2 u = N_1 \quad (2.1)$$

$$\frac{\partial v}{\partial t} + U \frac{\partial v}{\partial x} + u \frac{\partial V}{\partial x} + V \frac{\partial v}{\partial y} + v \frac{\partial V}{\partial y} - 2\kappa Uu + \frac{\partial p}{\partial y} - \frac{1}{R} \nabla^2 v = N_2 \quad (2.2)$$

$$\frac{\partial w}{\partial t} + U \frac{\partial w}{\partial x} + V \frac{\partial w}{\partial y} + \frac{\partial p}{\partial z} - \frac{1}{R} \nabla^2 w = N_3 \quad (2.3)$$

$$\frac{\partial u}{\partial x} + \frac{\partial v}{\partial y} + \frac{\partial w}{\partial z} + \kappa v = 0 \quad (2.4)$$

where N_1 , N_2 and N_3 represent the nonlinear terms

$$N_1 = -u \frac{\partial u}{\partial x} - v \frac{\partial u}{\partial y} - w \frac{\partial u}{\partial z} - \kappa uv$$

$$N_2 = -u \frac{\partial v}{\partial x} - v \frac{\partial v}{\partial y} - w \frac{\partial v}{\partial z} + \kappa v^2$$

$$N_3 = -u \frac{\partial w}{\partial x} - v \frac{\partial w}{\partial y} - w \frac{\partial w}{\partial z}$$

and

$$\nabla^2 = \frac{\partial^2}{\partial x^2} + \frac{\partial^2}{\partial y^2} + \frac{\partial^2}{\partial z^2} + \kappa \frac{\partial}{\partial y}$$

The boundary conditions are

$$u = v = w = 0 \quad \text{at} \quad y = 0 \quad \text{and} \quad u \rightarrow 0, \quad v \rightarrow V_m(x), \quad w \rightarrow 0, \quad \text{as} \quad y \rightarrow \infty$$

where V_m signifies a nonzero value. Periodic boundary conditions are imposed in the spanwise direction. Here, ℓ_0 and U_e are constants so as to define Reynolds number R as

$$R = \frac{U_e \ell_0}{\nu}$$

where the length scale $\ell_0 = \sqrt{\frac{\nu X_0}{U_e}}$, X_0 being the location (dimensional) of a reference streamwise station, and ν the kinematic viscosity. Another important parameter which is a measure of the wall curvature is the Görtler number G defined as $G = R\sqrt{|\kappa|}$. The reason why ν does not go to zero outside the boundary layer is that the vertical velocity vanishes for all Fourier modes (see (2.5) below) except the mean-flow correction mode.

We use the method of parabolized stability equations (PSE) for our computations. Here, we follow the formulation of Malik & Li (1993b) (see also Malik et al. (1994)) and let $\phi = (u, v, w, p)$ be the disturbance vector and assume that the disturbance takes the form

$$\phi = \sum_m \sum_n \hat{\phi}_{mn}(x, y) \exp \left\{ i \int_{x_0}^x \alpha_{mn}(\xi) d\xi + i n \beta z - i m \omega t \right\} \quad (2.5)$$

where α_{mn} and β are the x and z wave numbers, ω is the perturbation frequency and $\hat{\phi}_{mn}$ is the amplitude function for the mode $(m\omega, n\beta)$. Substituting Eq (2.5) into Eqs (2.1) to (2.4), we obtain a set of equations with $\hat{\phi}_{mn}$ and α_{mn} as unknowns. Since, there are now more unknowns (namely, α_{mn}) than the equations, another condition is needed for the closure of the system. Since the basic flow is slow-varying in the streamwise direction, a condition on $\hat{\phi}_{mn}$ is imposed such that most of the waviness and growth of the perturbation is absorbed into the exponential function in Eq (2.5), making the amplitude function $\hat{\phi}_{mn}$ slowly-varying with respect to x . The terms containing $\frac{\partial^2 \hat{\phi}_{mn}}{\partial x^2}$ can thus be dropped and the only second derivatives left in the governing equations are those with respect to y . These new stability equations are parabolized in the sense of parabolized Navier-Stokes (PNS) equation for mean flow computations. The condition for choosing α_{mn} and minimizing the streamwise variation of the amplitude function can take several forms. In the present work, we choose α_{mn} to be such that the following integral vanishes.

$$\int_0^\infty \left(\hat{u}^*, \hat{v}^*, \hat{w}^* \right) \frac{\partial}{\partial x} \begin{pmatrix} \hat{u} \\ \hat{v} \\ \hat{w} \end{pmatrix} dy = 0 \quad (2.6)$$

where $*$ denotes complex conjugate. The PSE can be written in matrix form as

$$L_0 \hat{\phi}_{mn} + L_1 \frac{\partial \hat{\phi}_{mn}}{\partial y} + L_2 \frac{\partial^2 \hat{\phi}_{mn}}{\partial y^2} + L_3 \frac{\partial \hat{\phi}_{mn}}{\partial x} = N_{mn} \quad (2.7)$$

$$F(\hat{\phi}_{mn}, \alpha_{mn}) = 0 \quad (2.8)$$

where the coefficient matrices contain the Blasius flow quantities as well as α_{mn} , β and ω . Eq (2.8) is a general form of Eq (2.6). The matrix operators $L_0 - L_3$ and N_{mn} are given in Appendix I. The boundary conditions are

$$\hat{u}_{mn} = \hat{v}_{mn} = \hat{w}_{mn} = 0 \quad \text{at} \quad y = 0 \quad (2.9a)$$

$$\hat{u}_{mn}, \hat{v}_{mn} (\text{except for } m = n = 0), \hat{w}_{mn} \rightarrow 0 \quad \text{as} \quad y \rightarrow \infty \quad (2.9b)$$

No boundary condition is required for $\hat{v}(\infty)$ when $m = n = 0$.

We discretize the PSE using discrete Fourier transforms in the spanwise direction and in time. In the direction normal to the wall, we use the fourth-order compact difference scheme (Malik, Chuang & Hussaini, 1982) which requires that (2.7) be written as a system of first-order equations. Numerical computation starts at some streamwise location x_0 where velocity components are prescribed for a given wavenumber α_{mn} ; the velocities and pressure at $x_0 + dx$ are calculated using backward Euler discretization. If Eq (2.8) were not satisfied, a new α_{mn} would be chosen and the equations solved again. This iterative process continues until Eq (2.8) is satisfied, and the computation proceeds to the next streamwise location. During this iterative process, nonlinear terms are also updated and one makes sure that they are converged before the solution proceeds downstream.

3. Nonlinear Development of Steady Görtler Vortices

In this section, we analyze the nonlinear development of streamwise stationary Görtler vortices ($\omega = \alpha = 0$). In the limit $R \rightarrow \infty$, and $\kappa \rightarrow 0$ with G held fixed, and by rescaling the dependent and independent variables ($V = O(1/R)U$, $(v, w) = O(1/R)u$, $y = O(1/R)x$) the parabolic equations derived by Hall (1983, 1988) can be recovered from (2.1–2.4). In Hall (1988), a further step is taken to eliminate the spanwise velocity and the pressure from the linear terms in Eq (2.7), resulting in a coupled system of fourth-order and second-order equations. However, we will solve Eq (2.7) directly in the primitive $(\hat{u}, \hat{v}, \hat{w}, \hat{p})$ formulation, except that the condition imposed on α (2.8) is not applied since α is identically 0.

The flow parameters used in the present analysis are taken from the experiment of SB. The radius of curvature of the concave surface is 320 cm and free stream velocity is 500 cm/s. The streamwise range of interest in our analysis lies approximately in $10 < X \text{ (cm)} < 120$, in which the Reynolds number based on the distance from the leading edge ($Re = R^2$) ranges from 3.3×10^4 to 4×10^5 and the Görtler number G_θ ranges from 1.3 to 8.3. The Blasius equations are solved to obtain the basic flow (U, V) for the vortex stability analysis. The calculation is started at $X_0 = 10$ cm for the disturbance wavelength $\lambda_z = 1.8$ cm and initial amplitude of $\hat{u} = 0.0187 U'_e$ estimated from

the experimental data of SB. At this stage, our aim is to analyze the steady nonlinear Görtler vortices; therefore, we only allow zero-frequency modes to be present. Unsteady modes will be taken into account later when we compute the development of secondary instabilities. The number of spanwise Fourier modes used in the z -direction is 11 (i.e., n goes from -10 to 10 in (2.5)), and the streamwise marching step-size is 0.82158 cm. Therefore, approximately 130 marching steps are taken in the streamwise direction. The number of wall-normal steps is 121. The solution was tested by changing the number of grid points and it was found to be grid-independent.

Attempt is made to compare with the experiment of SB in this paper. A few words of explanation are needed in order to clarify the manner in which comparisons are made. There is uncertainty in the experiment of SB (and in any experiment, in general) with regards to the spanwise wavelength of the Görtler vortices. As noted by SB, this wavelength varies across the span and its statistical average is 2.3 cm. The detailed measurements, however, are made for a pair of vortices with a spanwise wavelength of about 1.8 cm which, in fact, is close to the most amplified Görtler vortex according to linear theory. There is also a fair amount of scatter in the data in the "peak" region of the vortices for localized quantities such as the wall-shear. Our computation is performed with a constant spanwise wavelength, which is fixed at 1.8 cm. We could choose different wavelengths and initial amplitudes to obtain a whole range of results from which the best comparison with experiment can be found, but we would have little to gain from this. As Hall & Horseman (1991) pointed out that the inherent non-uniqueness of the Görtler problem might be present in the experiment as well and the exact features of the experiment itself might not be precisely reproducible. Consequently, our comparisons with the experiment are confined to the qualitative features and trends of the Görtler vortex development which are relatively insensitive to moderate variations in parameters such as wavelengths and initial amplitudes.

The experiment of SB (as well as others) produced "mushroom-like" structures for the streamwise velocity due to the pumping action of the counter-rotating vortices. The contours of the streamwise velocity at various downstream locations computed in the present analysis are shown in Figure 1. In the early stages of the development, the amplitude of u perturbation is small and the velocity contours show a wavy spanwise structure. As the Görtler vortices gather strength at relatively large distances downstream the same "mushroom" structures observed in the experiment of SB are clearly seen. The regions in the neighborhood of the centerlines of the "mushrooms" are referred to as "peak" regions where the streamwise velocity is relatively low; and the regions between the "mushrooms" are referred to as "valley" regions where the streamwise velocity is relatively high. The streamwise velocity profiles at the peak and the valley are shown in Figure 2. It will be shown later that the high shear layer region up in the peak plane will become subject to a particular mode of secondary instability. The spanwise variation of the streamwise velocity component at fixed y is

given in Figure 3. Again, the inflected profiles will be subject to another mode of secondary instability.

The energy in each Fourier mode is shown in Figure 4. Here, energy is defined as

$$E_n = \int_0^{\infty} \left(|\hat{u}_n|^2 + |\hat{v}_n|^2 + |\hat{w}_n|^2 \right) dy \quad (3.1a)$$

where $n > 0$, and

$$E_0 = \frac{1}{2} \int_0^{\infty} \left(|\hat{u}_0|^2 + |\hat{w}_0|^2 \right) dy \quad (3.1b)$$

Initially, the Görtler vortex (mode 1) develops approximately linearly, but later on it begins to saturate. Due to nonlinearity, higher harmonics (mode 2,3,...) and mean flow distortion mode (mode 0) are generated. Among these, first the mode 0 and 2 have about the same energy, but at approximately $X = 75$ cm, the energy in the mean flow correction mode takes over that of the fundamental, and hence, the mean flow correction mode becomes the dominant mode, as also found by Hall and Lakin (1988) for the small wavelength Görtler vortices. This has important physical consequences, which will be explained later. Farther downstream, the energy in each mode begins to level off, approaching saturation. Although the energy in modes 2 and higher remains much lower than that of the fundamental, they all are important in the development of the narrow neck structure of the mushroom seen in Figure 1(d).

We now consider the wall shear in the peak and the valley plane. Figure 5 shows the computed normal wall shear in these regions, together with the experimental data of SB. Initially, the shear at the peak and at the valley decreases and increases, respectively, due to the slow-down and speed-up of streamwise velocity at the respective locations. Farther downstream, the shear at the peak turns around and starts to increase at approximately $X = 70$. It has been argued by Hall (1990) that the rise in shear is solely due to nonlinear interaction of steady and unsteady disturbances, without which the shear would continue to decrease and eventually leads to flow reversal near the wall. However, in SB, the amplitude of the unsteady fluctuations at this stage is, at least, one order of magnitude smaller than that of the steady Görtler vortex and it is unlikely that such drastic change in flow character is caused by these unsteady fluctuations. The normal wall shear at the peak is larger compared with the experiment of SB. Using a spanwise wavelength of 2.3 cm instead of 1.8 cm gives a much better comparison. We point out that Lee & Liu (1992) used a lower initial amplitude for the wavelength for $\lambda_z = 1.8$ cm and showed better agreement with experiment for wall shear. We point out that in our calculations, the increase in the shear stress is independent of the initial conditions and the location where they are imposed.

Now we explore the reason why the wall shear at the peak region turns around and starts to increase at approximately $X = 70$ cm for $\lambda_z = 1.8$ cm. This location is very close to the point where the energy in the mean flow correction mode takes over that of the fundamental ($X = 72$ cm). Also plotted in Figure 5 is the streamwise mean wall-shear, which is entirely due to the mean flow correction to which all the harmonics contribute. The mean wall shear at large distances downstream has rather large positive amplitude. Therefore, the explanation for the wall shear turn-around lies in the fact that, while the Görtler vortices try to slow down the fluid in the peak region, the mean flow correction tries to accelerate it. As the mean flow correction becomes more and more significant and eventually dominant, the wall shear has a large contribution from the mean flow correction mode, which overpowers the other modes to produce an increase in the streamwise velocity in the peak plane, resulting in the increase in wall shear. Figure 6 shows the computed streamwise velocity profiles along the peak region at various streamwise locations. It clearly shows (see also Figure 2) that even though the profiles are highly inflectional, the near wall behavior of the velocity would not give rise to negative shear. The domination of the mean flow correction mode also explains why the shear stress cannot go to zero and cause flow reversal.

The evolution of displacement thickness is shown in Figure 7. The computed results agree well with the experiment of SB up to about $X = 100$ cm where unsteady oscillations in the experiment become important. The displacement thickness decreases at the valley because of the high speed fluid brought down to the region near the wall by the Görtler vortices. In the peak region, the displacement thickness increases much faster than the corresponding displacement thickness of the Blasius boundary layer because of the low speed fluid brought into the upper regions of the boundary layer.

The present computations showed many of the qualitative features of the experimentally observed Görtler vortices. However, for an understanding of the breakdown of these vortices due to secondary instabilities, we have to consider unsteady modes. We will use the steady Görtler vortex flow field generated above as the basic flow state for our secondary instability analysis given in the next section. Thus, if u_G , v_G , w_G are the perturbation velocities due to the Görtler vortex, the new mean flow whose stability will be analyzed in the next section is

$$\bar{u} = U + u_G \quad (3.2a)$$

$$\bar{v} = V + v_G \quad (3.2b)$$

$$\bar{w} = W + w_G \quad (3.2c)$$

4. Linear Inviscid Secondary Instability

4.1 Governing equations

We assume that the streamwise variation of the new mean flow $(\bar{u}, \bar{v}, \bar{w})$ is small compared with the wavelength of the secondary disturbance. This assumption can be justified a posteriori from the results. Therefore, the linear secondary oscillation can be written as

$$\psi(x, y, z, t) = \hat{\psi}(y, z)e^{i(\alpha x - \omega t)}, \quad (4.1)$$

where $\psi = (u_s, v_s, w_s, p_s)$ and $\hat{\psi} = (\hat{u}_s, \hat{v}_s, \hat{w}_s, \hat{p}_s)$; α is the wavenumber, ω is the oscillation frequency, and the subscript s indicates secondary instability. Here, we consider only the temporal instability; therefore α is real and ω is complex. The flow field is unstable to disturbances if $\omega_i > 0$.

We note that $\bar{v}(y, z)$ and $\bar{w}(y, z)$ are much smaller than $\bar{u}(y, z)$. Then, following Hall & Horseman (1991), the equations governing the linear secondary instability are

$$i\alpha\hat{u}_s + \frac{\partial\hat{v}_s}{\partial y} + \frac{\partial\hat{w}_s}{\partial z} = 0 \quad (4.2)$$

$$i\alpha(\bar{u} - c)\hat{u}_s + \frac{\partial\bar{u}}{\partial y}\hat{v}_s + \frac{\partial\bar{u}}{\partial z}\hat{w}_s = -i\alpha\hat{p}_s \quad (4.3)$$

$$i\alpha(\bar{u} - c)\hat{v}_s = -\frac{\partial\hat{p}_s}{\partial y} \quad (4.4)$$

$$i\alpha(\bar{u} - c)\hat{w}_s = -\frac{\partial\hat{p}_s}{\partial z} \quad (4.5)$$

where $c = \omega/\alpha$ is the (complex) disturbance phase velocity. Eliminating $\hat{u}_s, \hat{v}_s, \hat{w}_s$, we obtain the equation governing the secondary pressure oscillation (after dropping subscript s):

$$\left(\frac{\partial^2}{\partial y^2} + \frac{\partial^2}{\partial z^2} - \alpha^2 \right) \hat{p} - \frac{2\bar{u}_y \hat{p}_y}{\bar{u} - c} - \frac{2\bar{u}_z \hat{p}_z}{\bar{u} - c} = 0 \quad (4.6)$$

The boundary conditions are

$$y = 0, \quad \hat{p}_y(y, z) = 0 \quad (4.7a)$$

$$y \rightarrow \infty, \quad \hat{p}(y, z) \rightarrow 0 \quad (4.7b)$$

and

$$\hat{p}(y, z) = \hat{p}(y, z + \lambda_z) \quad (4.8)$$

where λ_z is the Görtler vortex wavelength.

Equations (4.6–4.8) constitute an eigenvalue problem which is solved by using a Chebyshev collocation method in the y direction and a Fourier collocation method in the z direction with

appropriate grid stretchings in both directions to concentrate more collocation points in regions of high gradients. Furthermore, since the basic flow state is symmetric, the eigenfunctions can be split into families of even and odd modes. For the even mode, $\hat{p}(y,z) = \hat{p}(y,-z)$ and for the odd mode, $\hat{p}(y,z) = -\hat{p}(y,-z)$. Taking advantage of the symmetry conditions, we reduce the size of the resulting discretized system by approximately half. The discretized system can be represented in the form

$$A\phi = \omega B\phi \quad (4.9)$$

where B is a diagonal matrix and A is a square matrix of size $N_y(N_z/2 + 1)$, where N_y and N_z are the number of collocation points in y and z directions, respectively. This eigenvalue problem is solved by the QR method which yields all the eigenvalues of the discretized system (4.9). Throughout the computations, we use $N_y = 85$ and $N_z = 32$.

4.2 Results of Secondary Instability Calculations

During the early stage of the Görtler vortex development, the quantity $\nabla^2 \bar{u}$ is negative everywhere in the (y,z) -plane. At approximately $X = 40$ cm, a region of positive $\nabla^2 \bar{u}$ begins to appear near the wall. Therefore, according to the necessary condition for instability (i.e. $\nabla^2 \bar{u} = 0$ somewhere in the flow field), the Görtler vortex for the initial conditions prescribed in §3 is stable to secondary disturbances for $X < 40$ cm. We note that we have not shown whether the above condition is also a sufficient condition for instability.

We start our 2-D eigenvalue computations at $X = 65$ cm, where the high frequency oscillations are moderately unstable. Hence, we avoid the difficulty associated with the singularity due to neutral disturbances. The growth rate variation with the streamwise wavenumber at various streamwise locations between $X = 65$ cm and $X = 100$ cm, normalized with scales at $X = 10$ cm, is shown in Figure 8. The general trend is that the secondary oscillations become more unstable as the Görtler vortices become stronger downstream. The maximum growth rate at each streamwise location occurs at streamwise wavenumbers approximately between 0.2 and 0.3, corresponding to wavelengths between 1.2 and 1.7 cm. The Blasius boundary layer thickness in the absence of the Görtler vortices in the range between $X = 65$ cm and $X = 100$ cm is approximately between 0.7 and 0.9 cm. This shows that the wavelength of the secondary instabilities is of the order of boundary-layer thickness. Therefore, our assumption that the basic flow state variation is negligible over the distance of one wavelength is, indeed, justified. We can visually extrapolate the growth rate curves and see that, in this streamwise range, the highest wave number where secondary instability occurs is approximately 0.5, corresponding to a wavelength of 0.69 cm.

We now consider the variation of the maximum growth rate of the secondary instabilities with streamwise distance. In order to show that the secondary instability grows much faster than the Görtler vortex, we convert the temporal growth rate to the spatial one by using group velocity

transformation. The use of group velocity to transform temporal growth to spatial growth is well known for boundary-layer instabilities (Gaster 1962, Nayfeh & Padhye 1979). The value of group velocity $\partial\omega_r/\partial\alpha$ varies with x and lies in the range of 0.6 to 0.72. Figure 9 shows the spatial maximum growth rate of the most unstable even and odd modes, as well as the spatial growth rate of the Görtler vortex. The odd mode begins to become significant from approximately $X = 65$ cm, and the even mode roughly from $X = 75$ cm. An important feature we discover here is that, although the odd mode is the first to become unstable, the even mode takes over at roughly $X = 82$ cm to become the most unstable mode. The growth rate of the secondary instability is an order of magnitude higher than that of the nonlinear Görtler vortex.

The frequency and wavenumber of the secondary instability corresponding to the maximum growth rate at various streamwise locations are given in Table 1. We see that the frequencies vary greatly from one streamwise station to the next. The experimentally observed frequency of 130 Hz may not be that of the most unstable wave at large downstream distances. The relatively lower frequency waves (around 100 Hz) become unstable first. When the region of higher frequency waves is reached, the laminar basic flow state may have already been destroyed by the nonlinear growth of secondary instabilities and the higher frequency waves may not have a chance to manifest themselves. The temporal direct numerical simulation of Liu & Domaradzki (1993) has a computational box which restricts the maximum wavelength to 2.0 cm. According to Table 1, the frequency of most amplified disturbance is just above 160 Hz (their calculation gives about 200 Hz).

Table 1. Frequency and wavelength of the secondary instability modes

Odd Mode			Even Mode		
$X(\text{cm})$	$f(\text{Hz})$	Wavelength (cm)	$X(\text{cm})$	$f(\text{Hz})$	Wavelength (cm)
65.0	67.1	4.59	79.8	181.7	1.66
70.0	87.8	3.57	82.3	194.8	1.56
74.9	108.8	2.93	84.9	210.7	1.47
82.3	141.2	2.38	89.7	243.2	1.34
84.9	161.6	2.07	94.6	271.3	1.27
89.7	202.1	1.70			
94.6	243.0	1.47			

The calculations of Hall & Horseman (1991) were almost exclusively for the basic flow state at $X = 100$ cm. They found that the fastest growing wave (odd mode) has a frequency of about 110 Hz and a wavelength of about 3 cm. This would compare well with our results at about $X = 75$ cm. This can be

explained by noting the fact that their disturbed flow state amplitude is apparently lower than ours at corresponding streamwise locations; at $X = 100$ cm, our calculation in Figure 1 shows a thin neck while their $\bar{u}(y,z)$ plot does not show this and resembles more with the structure shown in our Figure 2(b).

We now consider the eigenfunctions of these secondary instability modes at $X = 95$ cm. The wavelength chosen here is 1.53 cm, close to the fastest growing odd and even modes at this downstream location. In addition to the most unstable odd and even modes, a second even mode is also considered. The contours of velocity eigenfunction $|\hat{u}_s|$ at $X = 95$ cm are shown as solid lines in Figure 10, together with basic flow state $\bar{u}(y,z)$ as dashed lines in the background. The eigenfunctions are normalized so that the maximum $|\hat{u}_s|$ has an amplitude of unity. The contours plotted are from 0.1 to 0.9 in intervals of 0.1, and $\bar{u}(y,z)$ contours plotted are from 0.1 to 0.9 in intervals of $0.1 U_e$. One feature to notice is that the phase speeds, c_r , of the modes shown in Figure 10 are all close to $0.7 U_e$, and the amplitudes of these modes are concentrated in the neighborhood of the manifold $\bar{u}(y,z) = 0.7 U_e$. This manifold would be the critical layer in the case of neutral stability.

The contours shown in Figure 10 bear some similarity to those obtained by Hall & Horseman (1991) despite the difference between the basic flow states in their work and the present work. The odd mode has two dominant peaks, one on either side of the peak plane. In the case of the even modes, the second even mode has three dominant peaks similar to that shown in Figure 6 (a) of Hall & Horseman (1991) for the only even mode they analyzed in their work. The most unstable single-peak even mode was not mentioned in Hall & Horseman (1991). Considering the fact that the growth rate of the first odd mode is about 1.7 times that of the second even mode and that, in the work of Hall & Horseman (1991), the odd mode grows almost twice as fast as the even mode, we are led to believe that the three-peak even mode analyzed by Hall & Horseman (1991) was actually the second unstable even mode, and the first unstable even mode was missed because they used a shooting technique to compute the eigenvalues. In our study, we use a global method which finds all the eigenvalues of the discretized problem.

The contours of $|\hat{u}_s|$ for the odd mode bears striking similarity to the streamwise rms fluctuations shown in Figure 16 of the temporal simulation of Liu & Domaradzki (1993), suggesting that this mode indeed plays an important role in the break-up of Görtler vortices.

From the eigenfunctions, we see a definite relationship between instability and inflection in the velocity profiles. Figure 11 shows contours of vertical and horizontal velocity gradients \bar{u}_y and \bar{u}_z . The inflection in the velocity profiles occurs at points where the velocity gradient is maximum. The amplitudes of the eigenfunctions concentrate near the regions of maximum velocity gradient. Furthermore, the most unstable even mode is clearly associated with the vertical velocity gradient,

the most unstable odd mode is associated with the horizontal velocity gradient and the second most unstable even mode is associated with both gradients.

We have analyzed eigenmodes which are unstable at different streamwise locations if the base flow of Görtler vortex is free of unsteady perturbations of large amplitude. It will be shown in the next section that nonlinearity will cause the rms amplitude of the secondary instability to be modified.

Finally, we point out that the relative importance of odd and even modes may depend upon the flow parameters (such as Görtler number, wave number, etc.) which govern the evolution of the steady vortices. However, the general "shape" of the eigenfunctions and their association with the vertical or spanwise velocity gradients should remain the same.

5. Nonlinear Development of Unsteady Disturbances

We now solve Eqs. (2.7–2.8) to study nonlinear evolution of the steady as well as unsteady disturbances. The spatial secondary instability computations for the even and odd modes are started at streamwise locations where the respective modes are moderately unstable. Since exact initial conditions are difficult to obtain, we use the eigenfunctions obtained from inviscid linear secondary instability analysis to approximate these conditions. Calculations show that transients decay very fast. The initial amplitude assigned to these disturbances is small enough (of $O(10^{-5})$ in \hat{u}_s for both odd and even modes) to ensure that the initial evolution of the secondary instability is linear.

We first discuss the computations for the odd mode. These calculations are performed in the following way. We start the calculations at $X = 10\text{cm}$ for only the steady disturbances. These calculations are carried up to $X = 75\text{ cm}$ where the unsteady odd mode disturbances are introduced. The frequency of the fundamental secondary instability is chosen to be 110 Hz, very close to the most unstable odd mode at that location (109 Hz). The number of Fourier modes is 11 in the spanwise direction ($-10 \leq n \leq 10$) and 8 in time ($-7 \leq m \leq 7$). Figure 12 shows contours of streamwise rms fluctuations at four streamwise locations downstream of the starting location. Initially, the shape of amplitude distribution very much resembles the local eigenfunctions analyzed in the last section. Later on, at larger x , nonlinearity causes the amplitude distribution to become fatter, beginning to fill up the y - z plane. The maximum amplitude reaches about 20 percent of the free stream velocity, U_e . There are two regions of high amplitude: one near the wall and the other away from the wall. Initially the region near the boundary-layer edge has higher amplitude, but as the disturbances evolve downstream the near-wall region attains higher amplitude. The contours of streamwise mean flow (time averaged flow) at corresponding streamwise locations are shown in Figure 13. The changes in the "mushroom" structure from that without the high frequency oscillations far downstream are profound (compare with Figure 1(c)). The top of the "mushroom" becomes flatter due to the fact that strong unsteady oscillations smear out the differences in velocity gradients. As

the oscillations get stronger, the "thin neck" region of the "mushroom", where low speed fluid lifts up, becomes confined to the neighborhood close to the wall. The experiments of SB show similar structure of the vortices prior to breakdown, except that in their experiment vortices tend to lose symmetry about the peak plane. Some of our calculations suggest that such loss of symmetry is linked to the unsymmetric initial disturbance field.

We now carry out computations for the even mode, which is introduced at the streamwise location $X = 82$ cm. The frequency of the fundamental secondary instability is taken to be 195 Hz, which is the frequency of the most unstable even mode at that location. The number of Fourier modes is the same as in the odd mode case. In the early linear stage, the distribution of amplitude of the streamwise rms fluctuation is concentrated in the region away from the wall. Nonlinear interaction brings the perturbation level near the wall. The rms values of streamwise fluctuations and the mean flow are shown in Figures 14 and Figure 15, respectively.

In their numerical simulation, Liu & Domaradzki (1993) observed that the oscillation frequency of the vertical velocity is twice that of the spanwise velocity in the low speed region, while the two frequencies are the same away from that region. This is also found to be the case in the present computations for the odd mode. Figure 16 shows the vertical and spanwise velocity fluctuations at two fixed locations in space, one in the low speed region, the other away from it. Counting the number of dominant peaks, we can observe the difference in frequency in the low speed region. This phenomenon can be explained by considering the spatial symmetry preservation property of the fundamental secondary instability and its harmonics. Initially, the only mode present is the fundamental with frequency, say, f . In the odd mode case, the vertical velocity fluctuation for the fundamental mode is odd with respect to the line of symmetry of the background "mushroom" structure, while the spanwise velocity fluctuation is even. It can be mathematically verified that the symmetry properties of the harmonics obey the following rule: for the vertical velocity, modes with frequencies $2f$, $4f$, $6f$, etc. are even, while modes with frequencies $3f$, $5f$, $7f$, etc. are odd; for the spanwise velocity, modes with frequencies $2f$, $4f$, $6f$, etc. are odd, while modes with frequencies $3f$, $5f$, $7f$, etc. are even. These symmetry properties are preserved as the flow develops downstream. Suppose we place a velocity probe somewhere along the line of symmetry of the background "mushroom" structure, we cannot detect the amplitude of the fundamental mode of the vertical velocity since it is odd and, therefore, has zero-amplitude there. The lowest frequency mode that can be detected is the $2f$ mode of the vertical velocity. The lowest frequency mode of the spanwise velocity that can be detected is the fundamental mode. Hence, it appears that, in the peak region, the frequency of the vertical velocity is twice that of the spanwise velocity. Once we move away from the peak region, the fundamental modes of both the vertical and the spanwise velocities can be detected, therefore, the same frequencies are observed.

We define the energy associated with frequency, mf , as

$$E_m = \sum_{n=-\infty}^{\infty} \int_0^{\infty} (|\hat{u}_{mn}|^2 + |\hat{v}_{mn}|^2 + |\hat{w}_{mn}|^2) dy \quad (5.1a)$$

for $m > 0$, and

$$E_0 = \sum_{n=1}^{\infty} \left\{ \int_0^{\infty} (|\hat{u}_{0n}|^2 + |\hat{v}_{0n}|^2 + |\hat{w}_{0n}|^2) dy \right\} + \frac{1}{2} \int_0^{\infty} (|\hat{u}_{00}|^2 + |\hat{v}_{00}|^2) dy \quad (5.1b)$$

and plot it in Fig. 17 as a function of down stream distance for both the sinuous and the varicose secondary instability. The change in the zero-frequency mode is relatively slow. The energy curves of the fundamental-frequency modes for both type of secondary instabilities are roughly straight lines over a considerable range of streamwise distance before the energies in the harmonics become significant, indicating the rapid exponential growth.

We plot the instantaneous streamwise velocity contours in the x - z plane at $y = 1.08$ cm (Figure 18). We see that the odd mode perturbs the Görtler vortices in a wavy (or sinuous) manner, while the even mode breaks up the otherwise straight contours of Görtler vortices into series of knotty structures associated with the "horse-shoe" vortex mode of breakdown. At large downstream distances, more and more small scale structures begin to appear, as the flow heads for transition to turbulence.

In Fig. 19, we plot the instantaneous streamwise velocity (snapshots at three fixed times) in the y - z plane at $x = 101$ cm for the sinuous mode. Comparison with Fig. 1 clearly shows the effect of unsteady disturbances on the Görtler vortex. The unsteady motion computed here is qualitatively similar to that observed in the experiments (e.g., Peerhossaini & Wesfreid (1988)).

Finally, we point out that, as in the case of the steady Görtler vortex discussed earlier, quantitative one-to-one comparison with the experiment of SB is made difficult by the uncertainty in the initial amplitude of the secondary instability and the spanwise variation of Görtler vortex wavelength in the experiment. For example, the computed isocontours of streamwise velocity for the odd mode at $x = 102.3$ cm shown in Fig. 13 agree much better with results of SB at 110 cm than at 100 cm.

6. Conclusions

Computation of the nonlinear development of steady Görtler vortices, their stability characteristics with respect to high frequency secondary disturbances and the nonlinear spatial development of the secondary instabilities are carried out. Qualitative agreement with the experiment of Swearingen & Blackwelder (1987) (SB) is obtained. It is found that the wall shear in

the peak plane begins to increase at a sufficiently large downstream distance due to the nonlinear interaction of the stationary modes even before the unsteady oscillations become strong. The cause of this phenomenon is the fact that the mean flow correction mode ultimately becomes the dominant mode and overcomes the effort of the Görtler vortices to slow down the flow in the peak region. The energy in each stationary mode eventually approaches saturation. The computed "mushroom" structures bear strong resemblance to those obtained in the experiment of SB.

For this particular basic flow state which is set up due to the Görtler vortices, the temporal secondary instability analysis is carried out using a 2-D eigenvalue approach associated with the governing partial differential equations. For the conditions of the experiment of SB, the odd mode of secondary instability begins to show up at approximately $X = 60$ cm, the even mode becomes unstable later at approximately $70 \text{ cm} < X < 75 \text{ cm}$. At about $X = 82$ cm, the even mode becomes more unstable than the odd mode. Comparisons of the amplitude distributions of eigenfunctions with the distributions of vertical and spanwise shear gradients clearly indicate the close association of the most unstable even mode with the vertical shear and the most unstable odd mode with the spanwise shear.

The nonlinear, spatial development of the odd and even modes of secondary instability is computed using the PSE method. The odd and even modes give rise to the sinuous instability and the varicose instability, respectively. Either mode can lead to the breakdown of Görtler vortices. The two-fold difference between the frequency of the vertical velocity and that of the spanwise velocity oscillations found by Liu & Domaradzki (1993) is simply due to the fact that the fundamental mode of the vertical velocity has zero amplitude at the line of symmetry of the "mushroom" for the sinuous instability and the high frequency in the vertical velocity they detected was, in fact, for the harmonic. Prior to breakdown to turbulence, the nonlinear interaction among the steady and unsteady modes eventually make Görtler vortices to oscillate sinuously in the plane parallel to the plate or cause them to develop horse-shoe type structures which travel downstream.

References

- Aihara, Y. and Koyama, H., 1981 "Secondary Instability of Görtler Vortices: Formation of Periodic Three-Dimensional Coherent Structures," *Trans. Japan Soc. Aero. Space Sci.*, Vol. 24, pp. 78-94.
- Beckwith, I. E., Malik, M. R., Chen, F.-J., and Bushnell, D. M., 1984 "Effects of Nozzle Design Parameters on the Extent of Quiet Test Flow at Mach 3.5," IUTAM Symposium on Laminar-Turbulent Transition, V. V. Kozlov, ed., pp. 589-600, Novosibirsk, USSR, Springer-Verlag.
- Bippes, H., 1978 "Experimental Study of the Laminar-Turbulent Transition of a Concave Wall in a Parallel Flow," NASA TM-75243.
- Floryan, J. M., 1991 "On the Görtler Vortex Instability of Boundary Layers," *Prog. Aerospace Sci.*, Vol. 28, pp. 235-271.

- Gaster, M., 1962 "A Note on the Relation Between Temporally Increasing and Spatially Increasing Disturbances in Hydrodynamic Stability," *J. Fluid Mech.*, Vol. 14, pp. 222-224.
- Hall, P., 1990 "Görtler Vortices in Growing Boundary Layers: The Leading Edge Receptivity Problem, Linear Growth, and Nonlinear Breakdown Stage," *Mathematika*, Vol. 37, pp. 151-189.
- Hall P. and Horseman, N. J., 1991 "The Linear Inviscid Secondary Instability of Longitudinal Vortex Structures in Boundary Layers" *J. Fluid Mech.*, Vol. 232, pp. 357-375.
- Hall, P., 1983 "The Linear Development of Gortler Vortices in Growing Boundary Layer," *J. Fluid Mech.*, Vol. 30, pp. 41-58.
- Hall, P. and Lakin, W. D., 1988 "The Fully Nonlinear Development of Görtler Vortices in Growing Boundary Layers," *Proc. R. Soc. Lond.*, Vol. A 415, pp. 421-444.
- Hall, P., 1988 "The Nonlinear Development of Görtler Vortices in Growing Boundary Layers," *J. Fluid Mech.*, Vol. 193, pp. 243-266.
- Ito, A., 1985 "Breakdown Structure of Longitudinal Vortices Along a Concave Wall," *J. Japan Soc. Aero. Space Sci.*, Vol. 33, pp. 116-173.
- Lee, K. and Liu, J. T. C., 1992 "On the Growth of Mushroomlike Structure in Nonlinear Spatially Developing Goertler Vortex Flow," *Phys. Fluids A*, Vol. 4, No. 1, pp. 95-103.
- Liu, W. and Domaradzki, J. A., 1993 "Direct Numerical Simulation of Transition to Turbulence in Görtler Flow," *J. Fluid Mech.*, Vol. 246, pp. 267-299.
- Malik, M. R., 1986 "Wave-Interaction in Three-Dimensional Boundary Layers," AIAA Paper No. 86-1129.
- Malik, M. R. and Hussaini, M. Y., 1990 "Numerical Simulation of Interactions between Görtler Vortices and Tollmien-Schlichting Waves," *J. Fluid Mech.*, Vol. 210, pp. 183-199.
- Malik, M. R. and Li, F., 1993a "Secondary Instability of Görtler and Crossflow Vortices," in *Proceedings of the International Symposium on Aerospace and Fluid Science*, Institute of Fluid Science, Tohoku University, Sendai, Japan, pp. 460-477
- Malik, M. R. and Li, F., 1993b "Transition Studies for Swept Wing Flows Using PSE," AIAA-No. 93-0077.
- Malik, M. R., Li, F., and Chang C.-L., 1994 "Crossflow Disturbances in Three-Dimensional Boundary Layers: Nonlinear Development, Wave Interaction and Secondary Instability," *J. Fluid Mech.*, Vol. 268, pp. 1-36.
- Malik, M. R., Chuang, S., and Hussaini, M. Y., 1982 "Accurate Numerical Solution of Compressible Stability Equations," *ZAMP*, Vol. 33, pp. 189-201.
- Nayfeh, A. H. and Padhye, A., 1979 "The Relation Between Temporal and Spatial Stability in Three-Dimensional Flows," *AIAA J.*, Vol. 17, pp. 1084-1090.
- Peerhossaini, H. and Wesfreid, J. E., 1988 "On the Inner Structure of Streamwise Görtler Rolls," *Int. J. Heat Fluid Flow*, Vol. 9, pp. 12-18.
- Sabry, A. S., Yu, X., and Liu, J. T. C., 1990 "Secondary Instabilities of Three-Dimensional Inflectional Velocity Profiles Resulting from Longitudinal Vorticity Elements in Boundary Layers,"

IUTAM Symp. on *Laminar-Turbulent Transition*, D. Arnal & R. Michel, eds., pp. 441-451, Toulouse, France, Springer-Verlag.

Sabry, A. S. and Liu, J. T. C., 1991 "Longitudinal Vorticity Elements in Boundary Layers" Nonlinear Development from Initial Görtler Vortices as Prototype Problem," *J. Fluid Mech.*, Vol. 231, pp. 615-663.

Swearingen, J. D. and Blackwelder, R. F., 1987 "The Growth and Breakdown of Streamwise Vortices in the Presence of a Wall," *J. Fluid Mech.*, Vol. 182, pp. 255-290.

Appendix I

Let $\Delta = -im\omega + i\alpha_{mn}U + \frac{\alpha_{mn}^2}{R} - \frac{i}{R} \frac{d\alpha_{mn}}{dx}$, then

$$L_0 = \begin{bmatrix} \Delta + \frac{\partial U}{\partial x} + \kappa V & \frac{\partial U}{\partial y} + \kappa U & 0 & i\alpha_{mn} \\ \frac{\partial V}{\partial x} - 2\kappa U & \Delta + \frac{\partial V}{\partial y} & 0 & 0 \\ 0 & 0 & \Delta & in\beta \\ i\alpha_{mn} & \kappa & in\beta & 0 \end{bmatrix}$$

$$L_1 = \begin{bmatrix} V - \frac{\kappa}{R} & 0 & 0 & 0 \\ 0 & V - \frac{\kappa}{R} & 0 & 1 \\ 0 & 0 & V - \frac{\kappa}{R} & 0 \\ 0 & 1 & 0 & 0 \end{bmatrix}$$

$$L_2 = \begin{bmatrix} -\frac{1}{R} & 0 & 0 & 0 \\ 0 & -\frac{1}{R} & 0 & 0 \\ 0 & 0 & -\frac{1}{R} & 0 \\ 0 & 0 & 0 & 0 \end{bmatrix}$$

$$L_3 = \begin{bmatrix} U - \frac{2i\alpha_{mn}}{R} & 0 & 0 & 1 \\ 0 & U - \frac{2i\alpha_{mn}}{R} & 0 & 0 \\ 0 & 0 & U - \frac{2i\alpha_{mn}}{R} & 0 \\ 1 & 0 & 0 & 0 \end{bmatrix}$$

N_{mn} is the Fourier transform of $(N_1, N_2, N_3, 0)^T$ in Eq. (2.1) to (2.4).

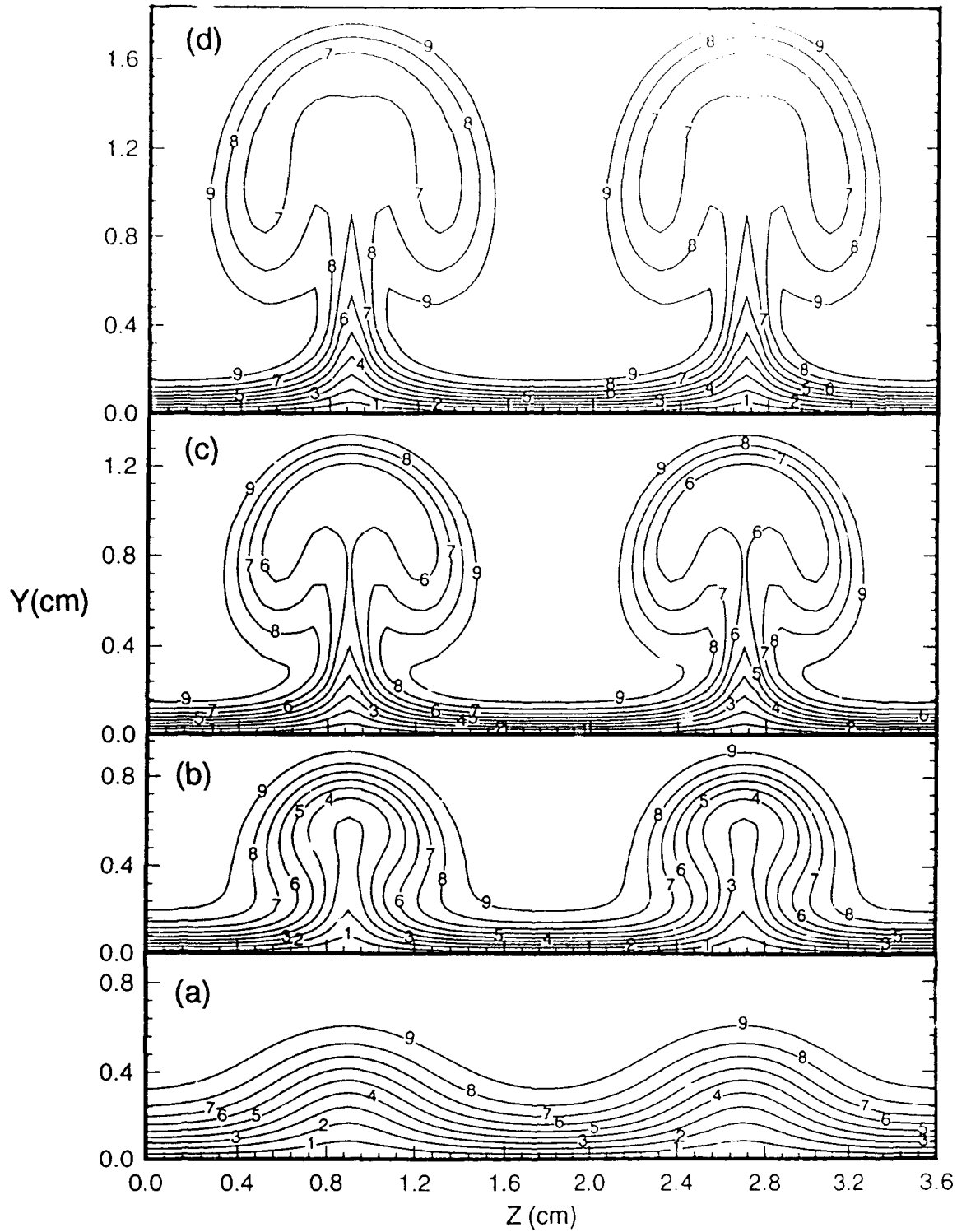


Fig. 1. Variation of streamwise velocity in the Y - Z plane due to the presence of Görtler vortices at (a) $X = 60.1$, (b) 79.8 , (c) 100.4 and (d) 120.1 cm. Two spanwise wavelengths are shown and contours range from $u/v_e = 0.1$ to 0.9 in increments of 0.1 .

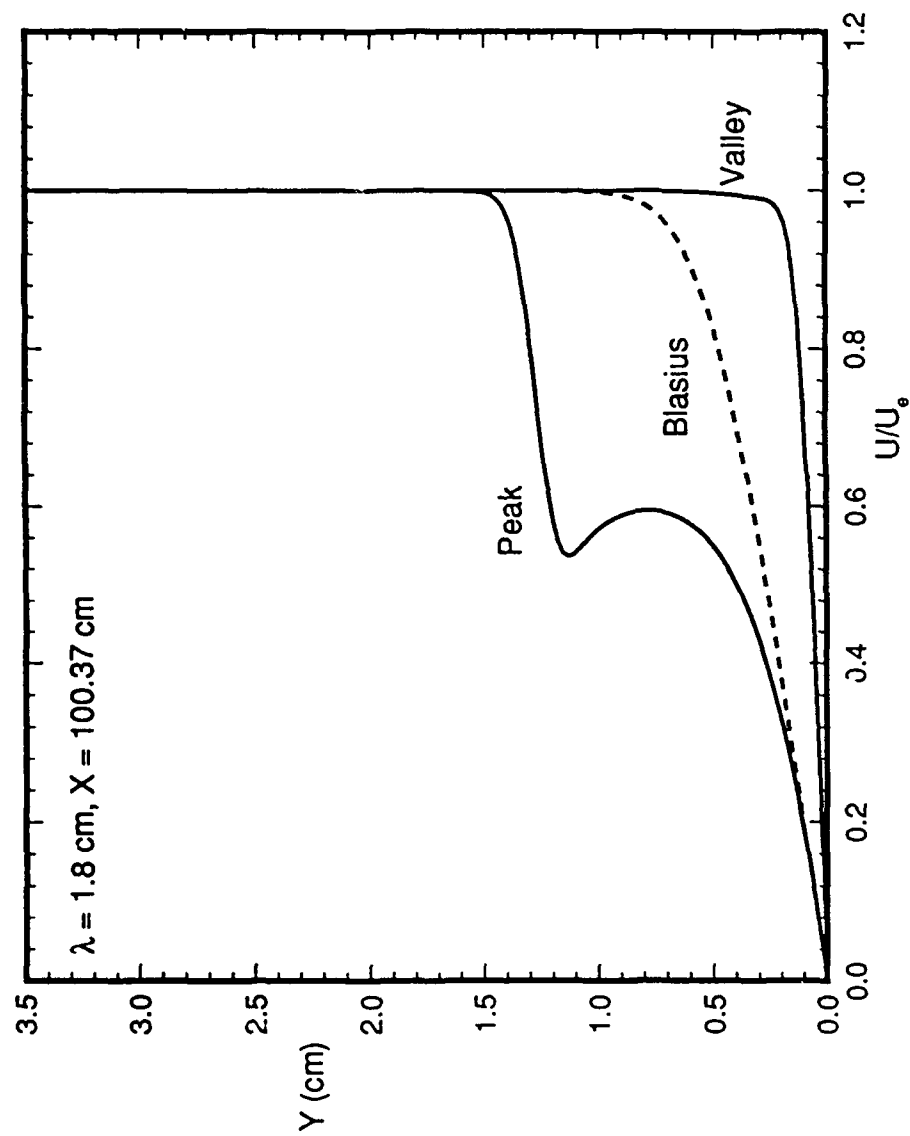


Fig. 2. Streamwise velocity profiles in the peak and the valley plane.

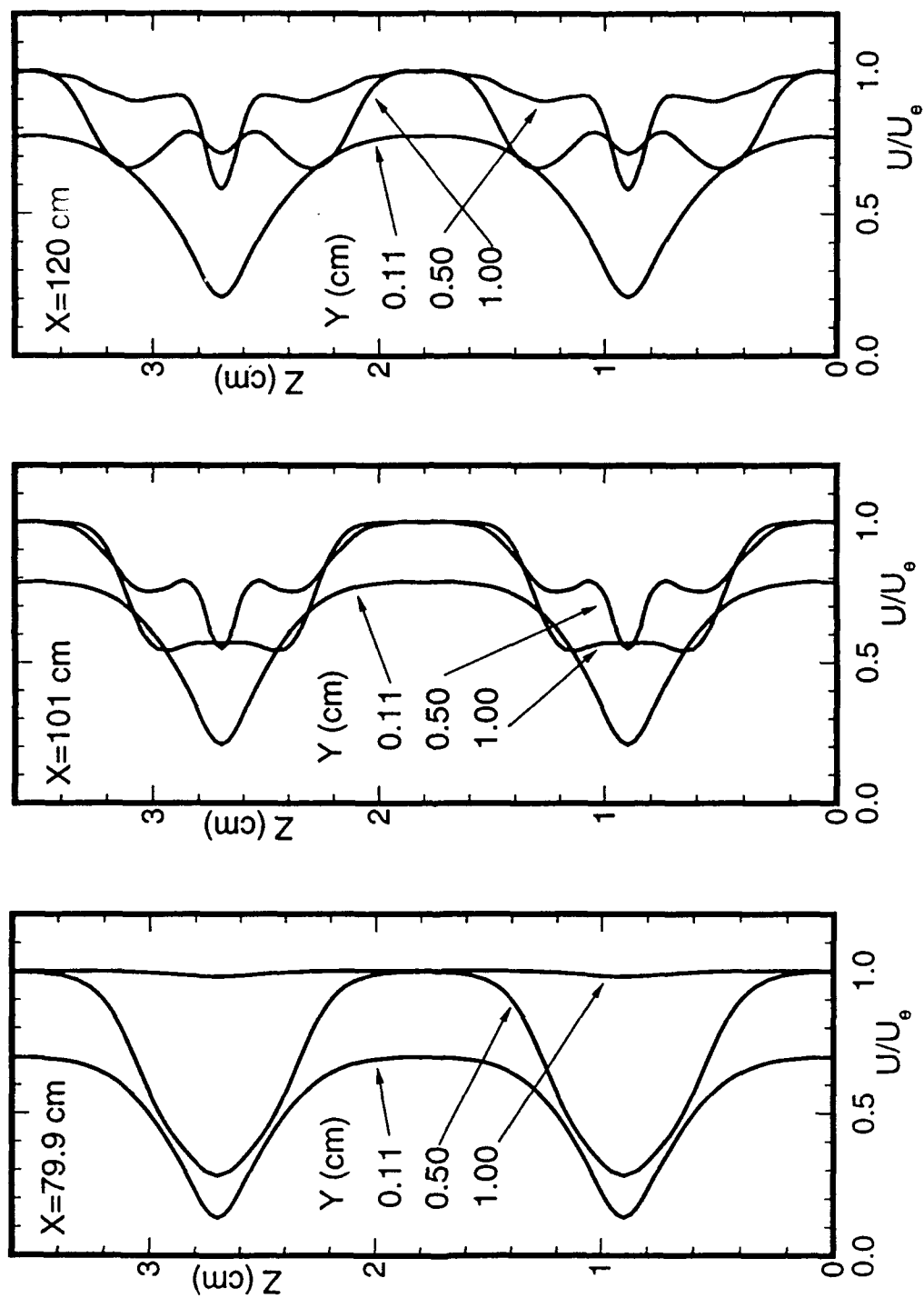


Fig. 3. Spanwise variation of streamwise velocity at fixed Y and three streamwise locations.

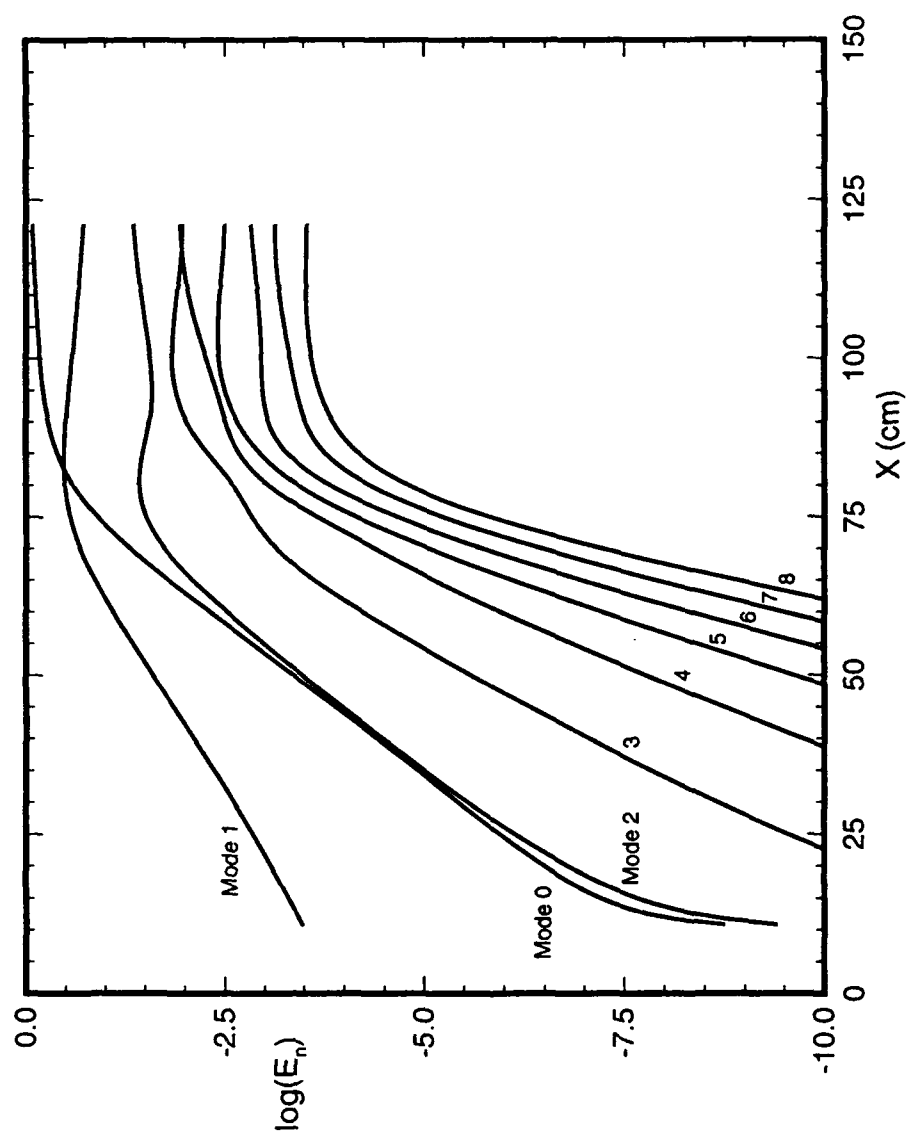


Fig. 4. Evolution of disturbance energy for various spanwise Fourier modes.

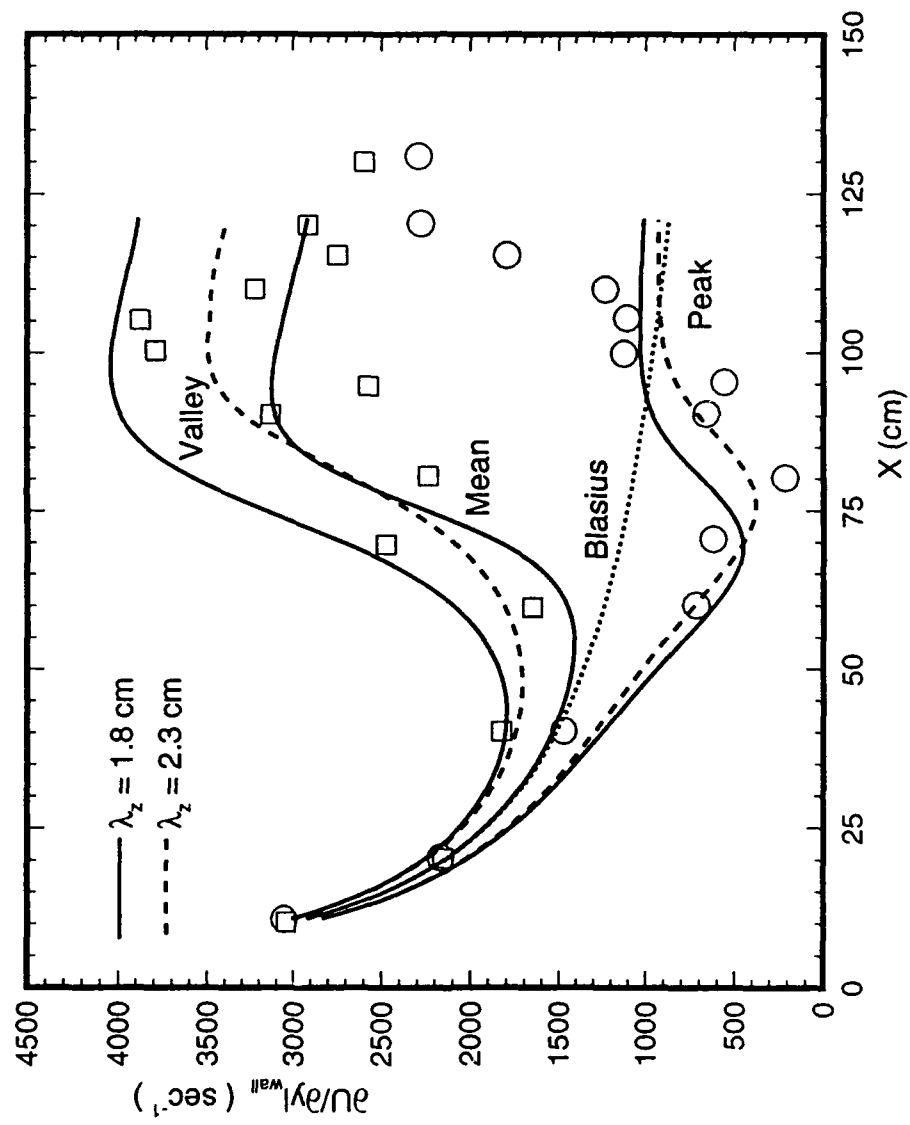


Fig. 5. Normal wall shear at the peak and the valley. Symbols represent the experimental data of SB.

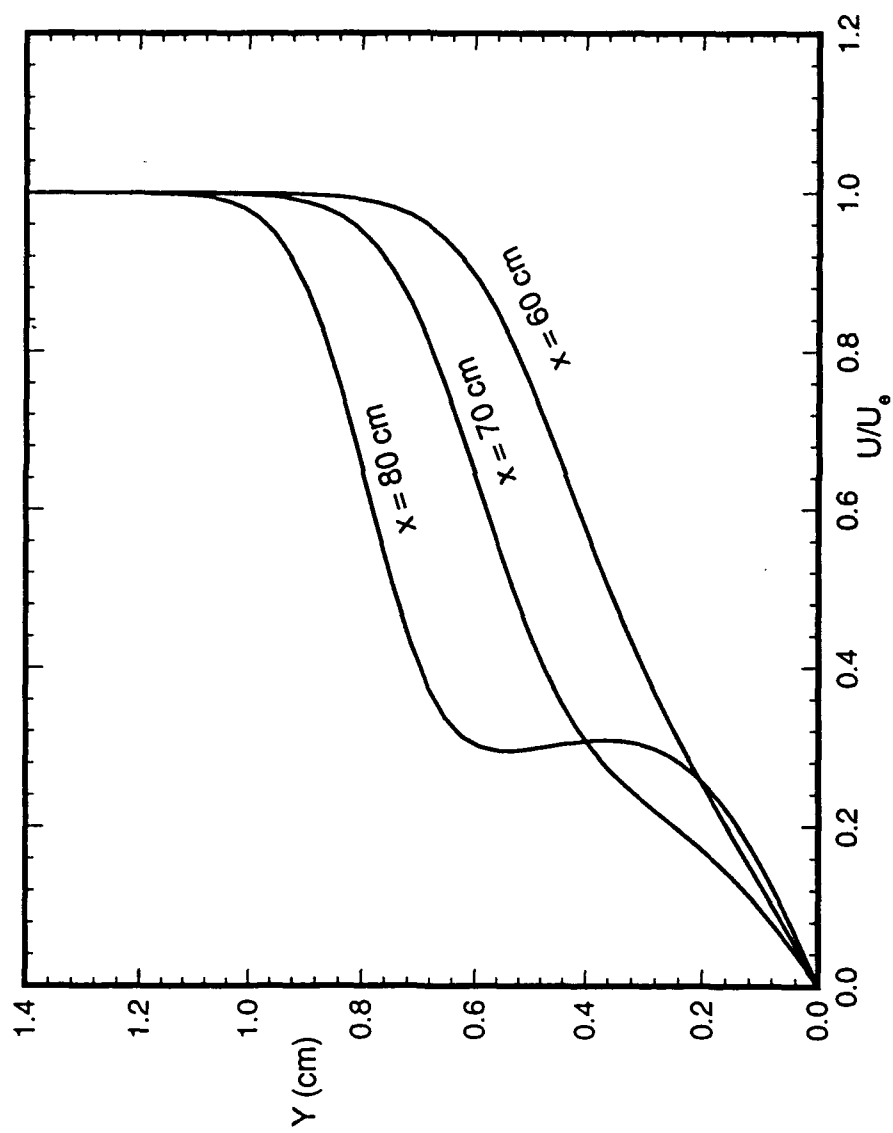


Fig. 6. Streamwise velocity profiles along the peak at various streamwise locations.

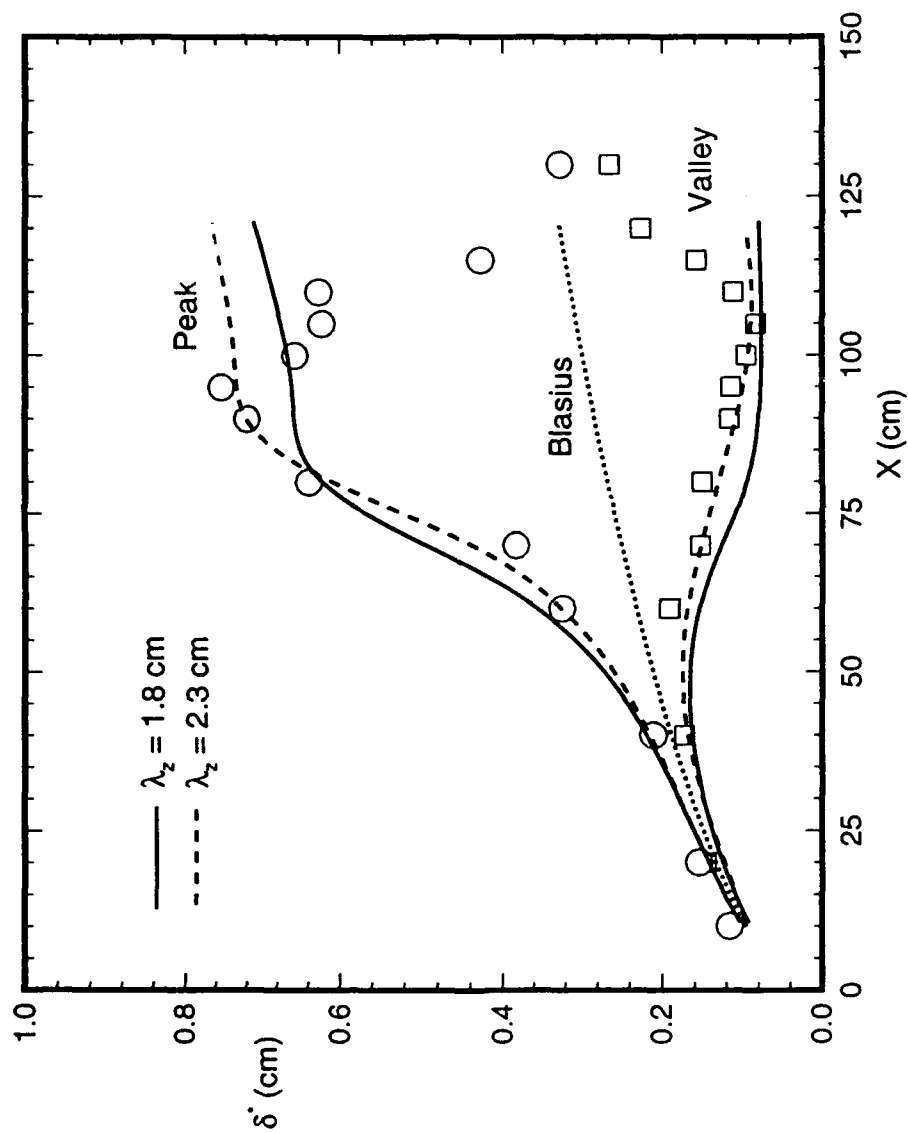
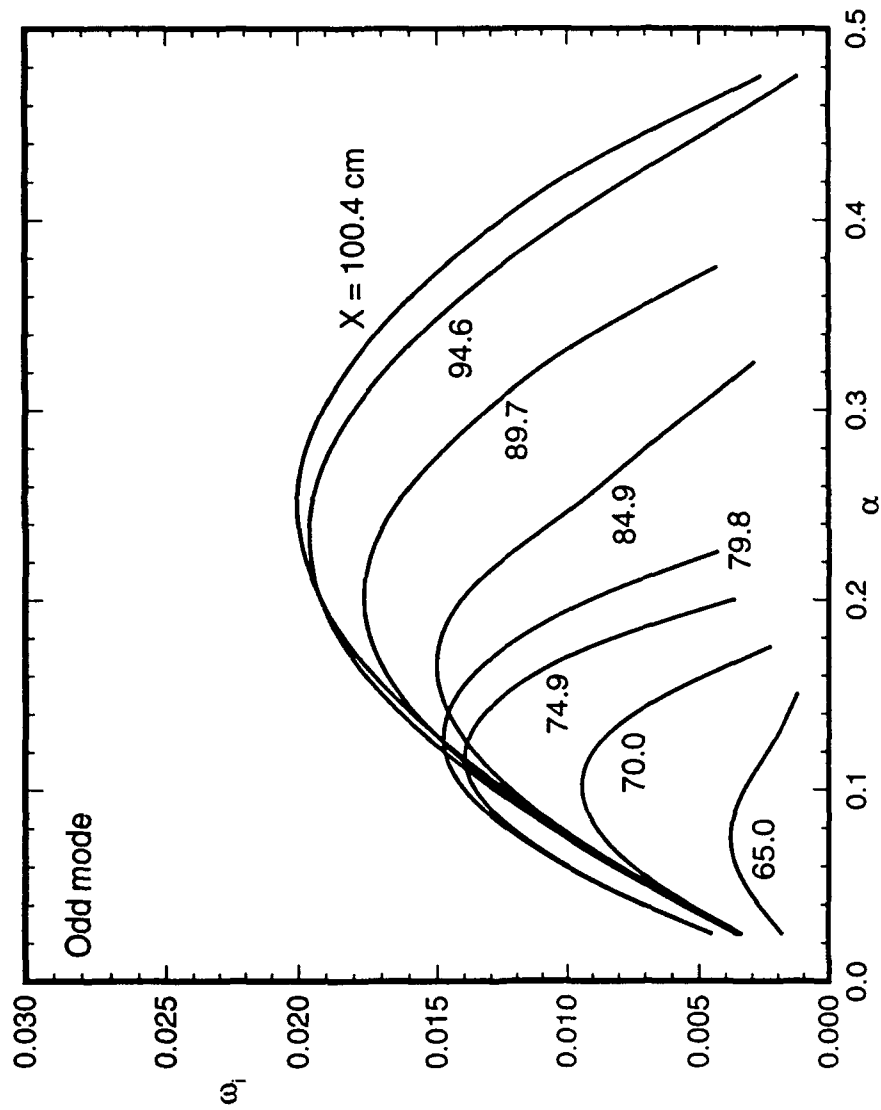
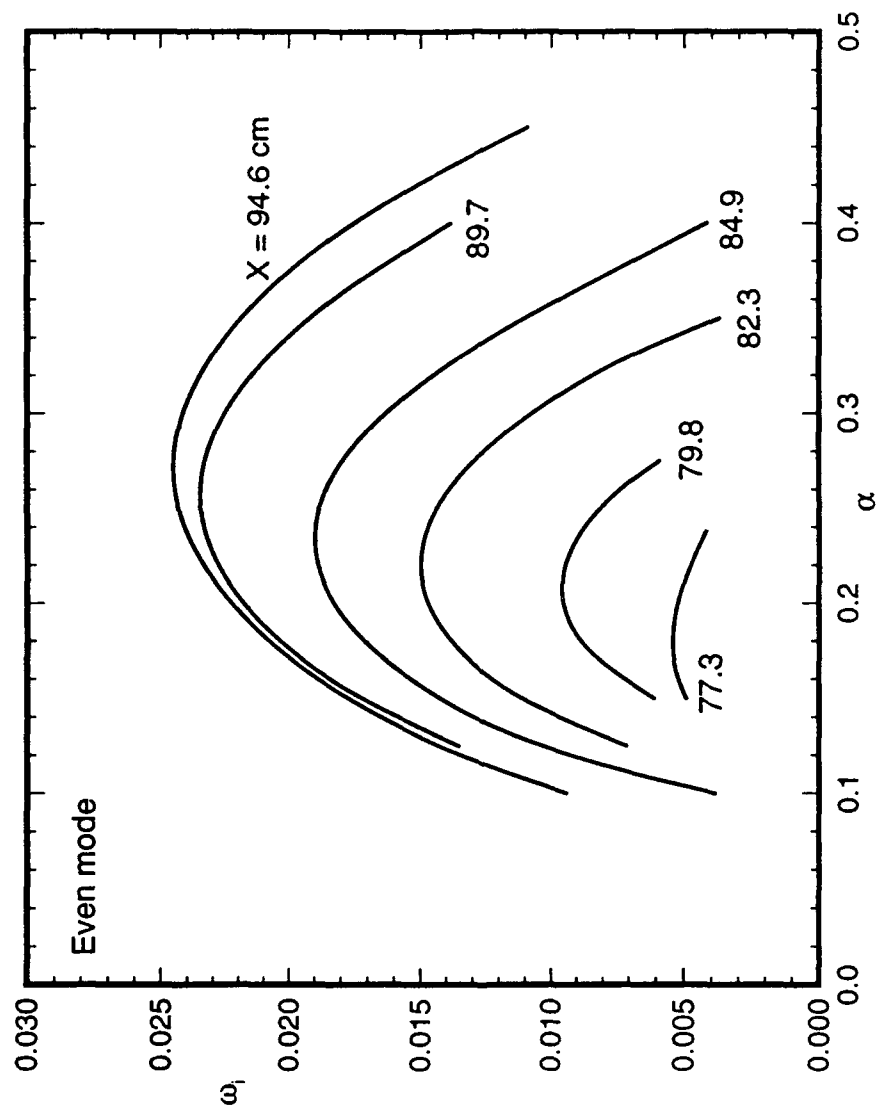


Fig. 7. Evolution of displacement thickness at the peak and the valley. Symbols represent the experimental data of SB.



(a) Odd Mode

Fig. 8. Secondary instability temporal growth rate variation with spanwise wave number at various streamwise locations.



(b) Even Mode

Fig. 8. Concluded.

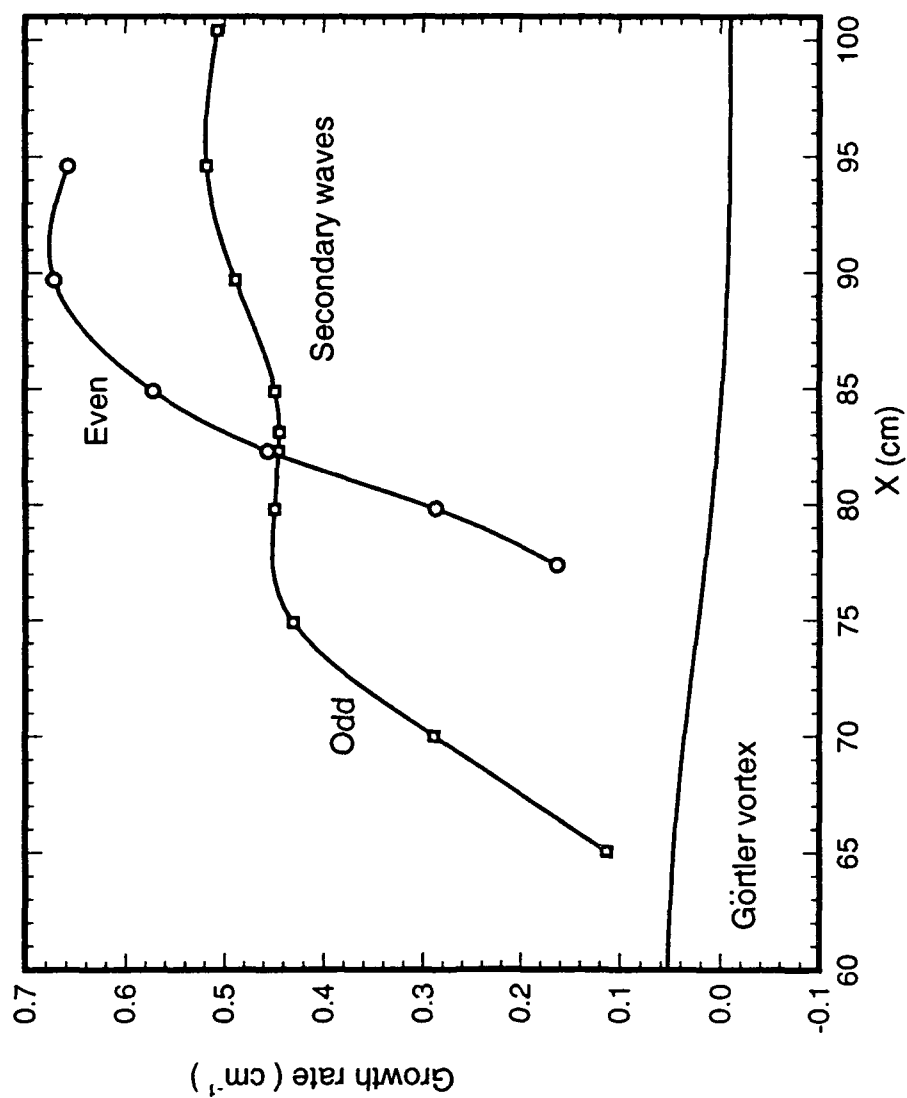
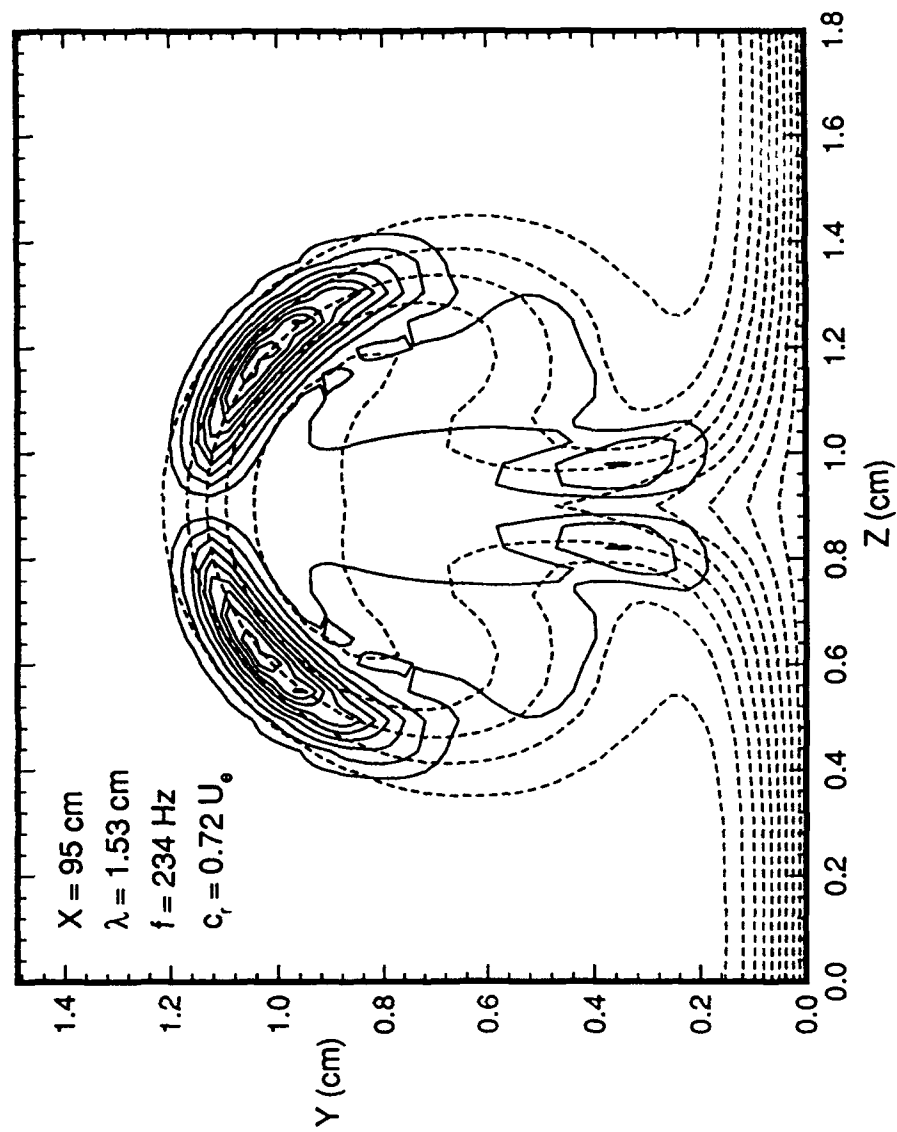
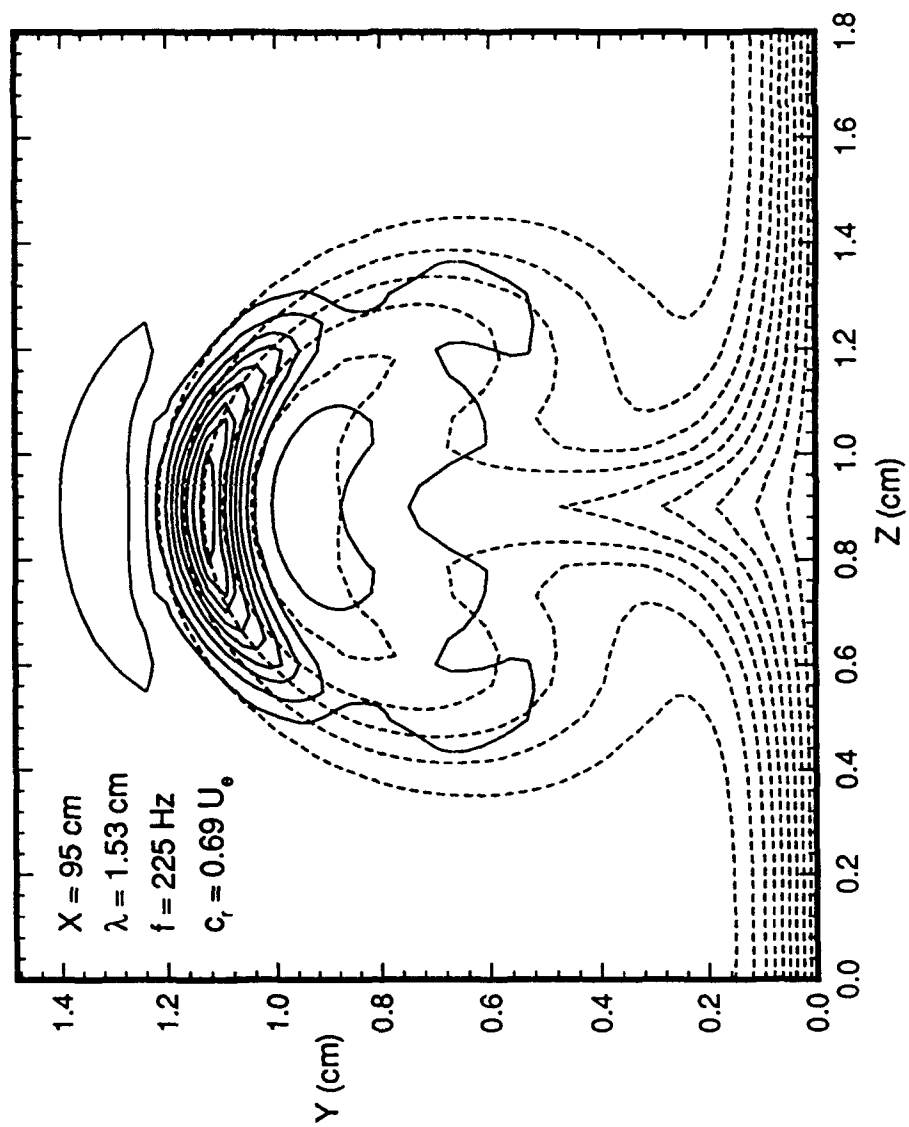


Fig. 9. Maximum spatial growth rate of the odd and even modes at various streamwise locations, compared with the growth rate of the Görtler vortex.



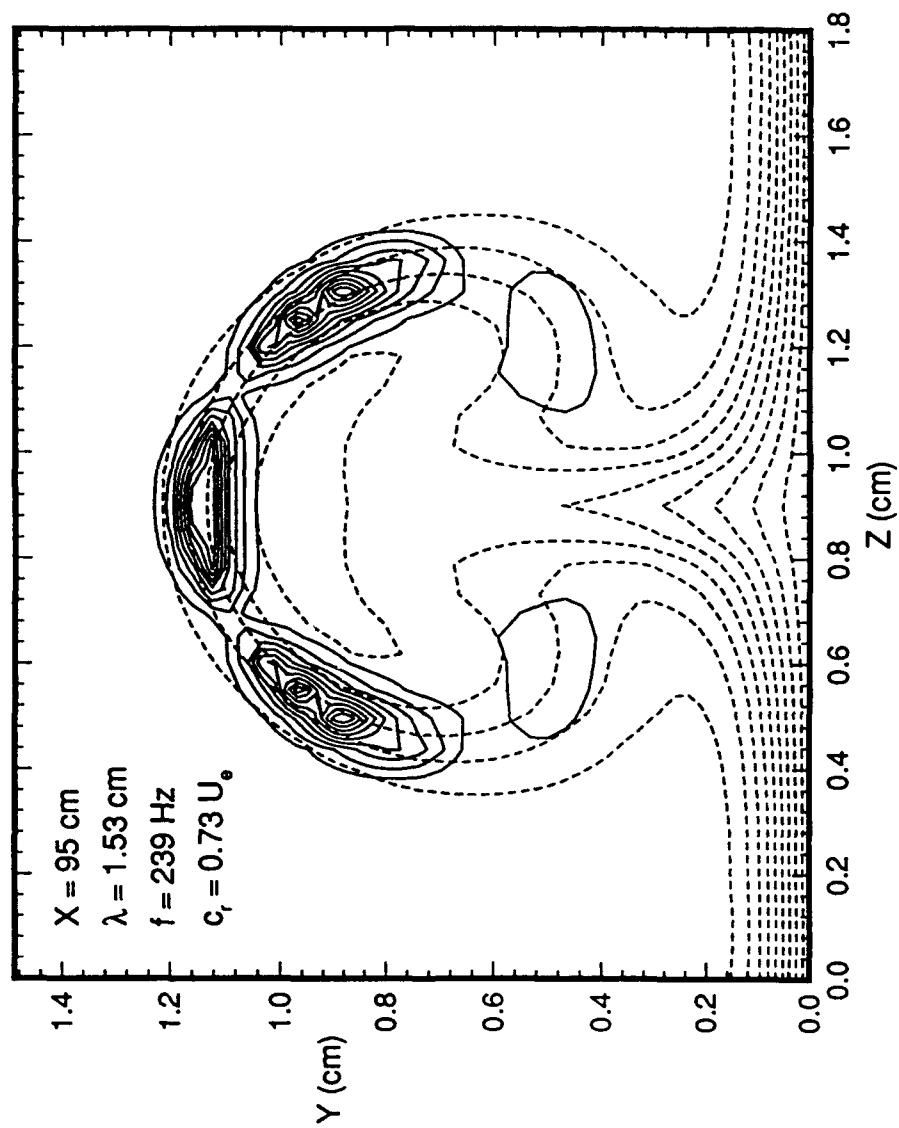
(a) Most Unstable Odd Mode

Fig. 10. Streamwise velocity eigenfunctions of secondary instability at $X = 95 \text{ cm}$.



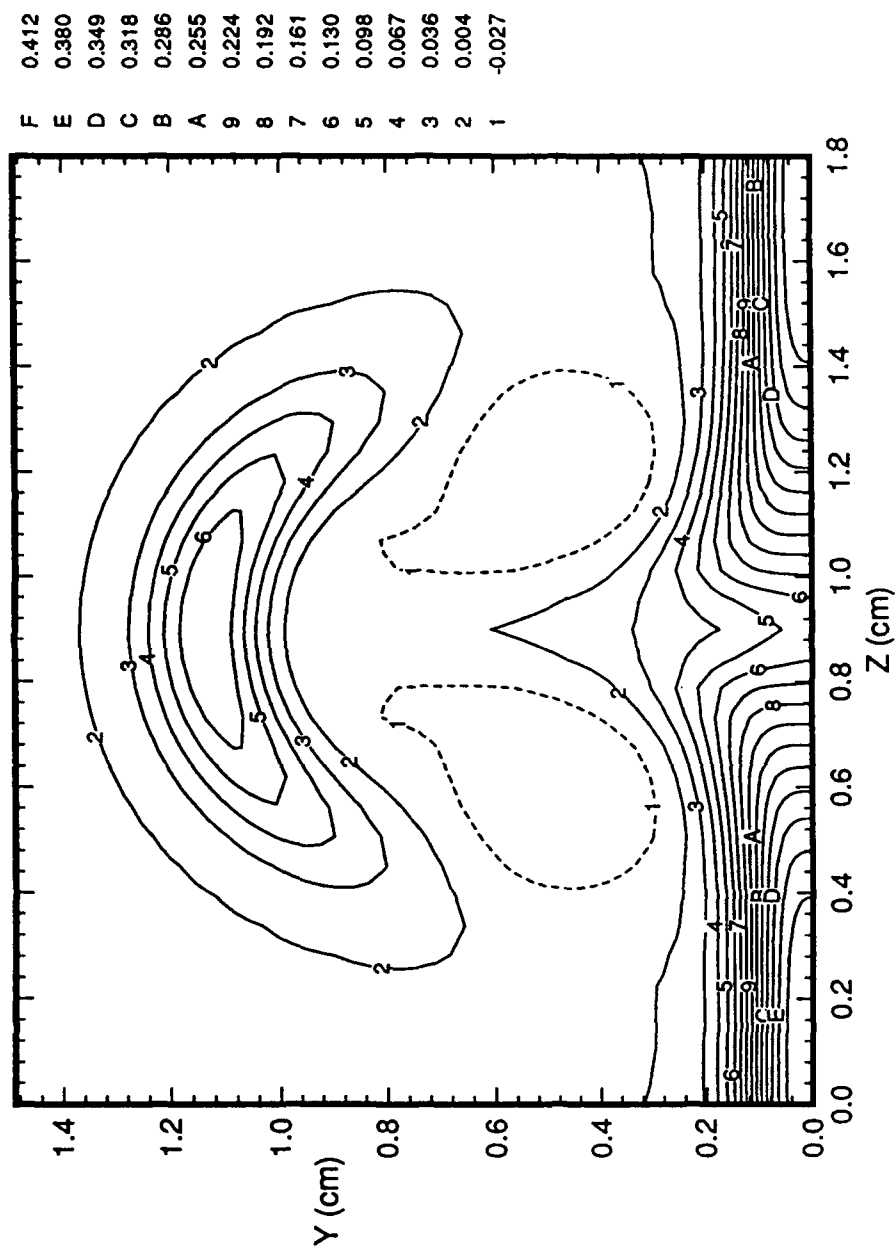
(b) Most Unstable Even Mode

Fig. 10. Continued.



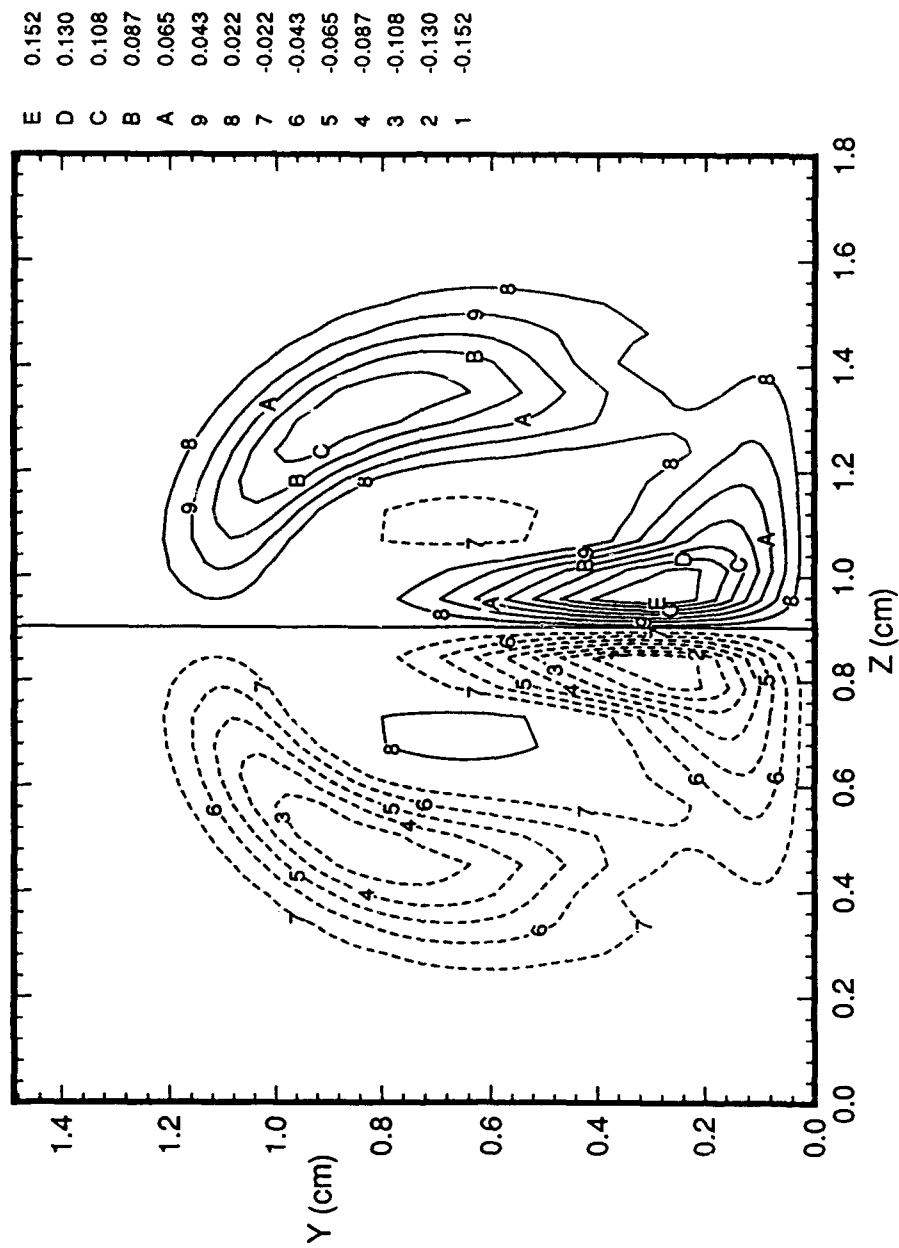
(c) Second Most Unstable Even Mode

Fig. 10. Concluded.



(a) $\partial \bar{u} / \partial Y$

Fig. 11. Variations of vertical and spanwise velocity gradients at $X = 95$ cm.



(b) $\partial \bar{u} / \partial Z$.

Figure 11. Concluded.

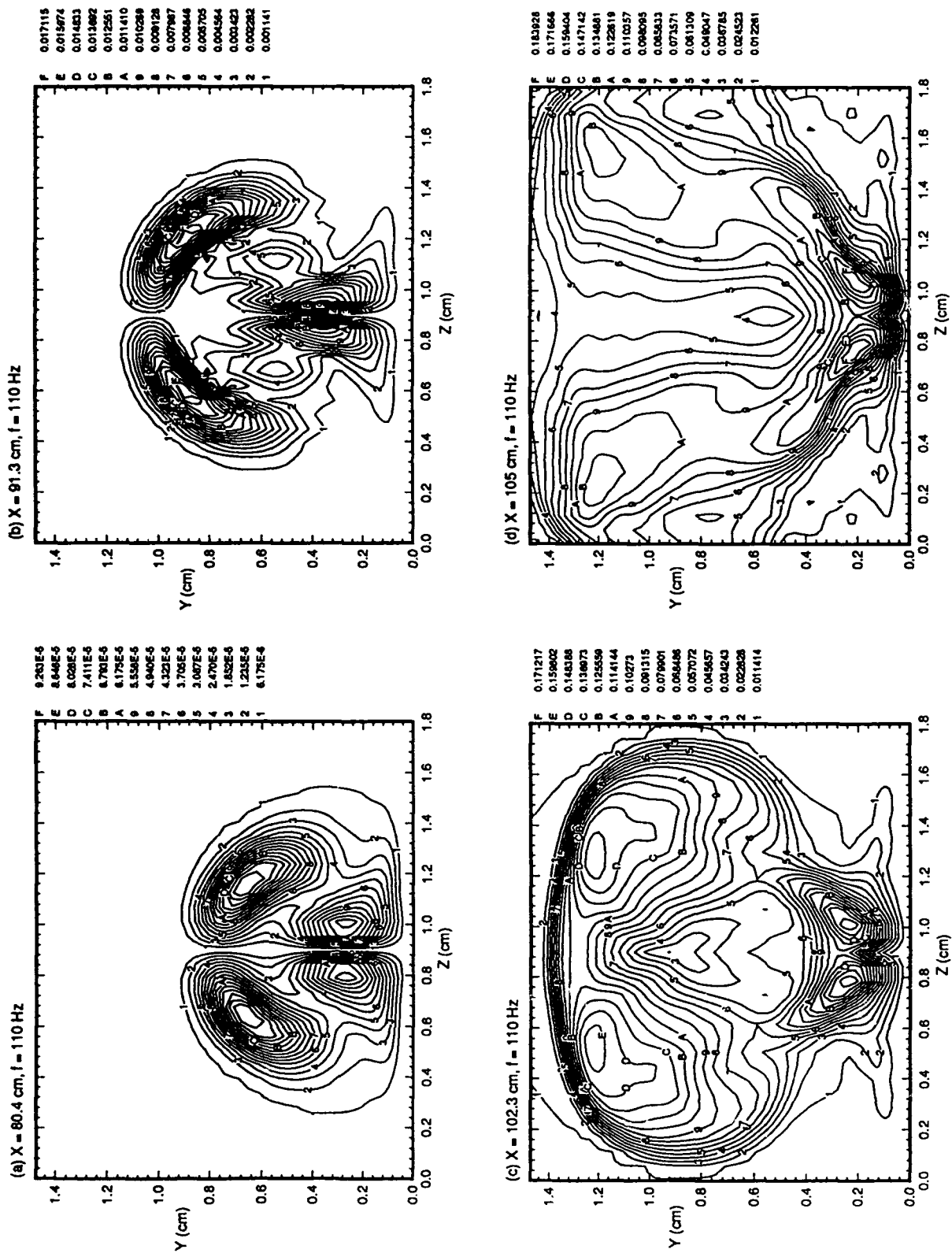


Fig. 12. Variation of rms streamwise velocity fluctuations in the Y - Z plane for the odd mode (a) $X = 80.4$ cm; (b) $X = 91.3$ cm; (c) $X = 102.3$ cm; (d) $X = 105$ cm.

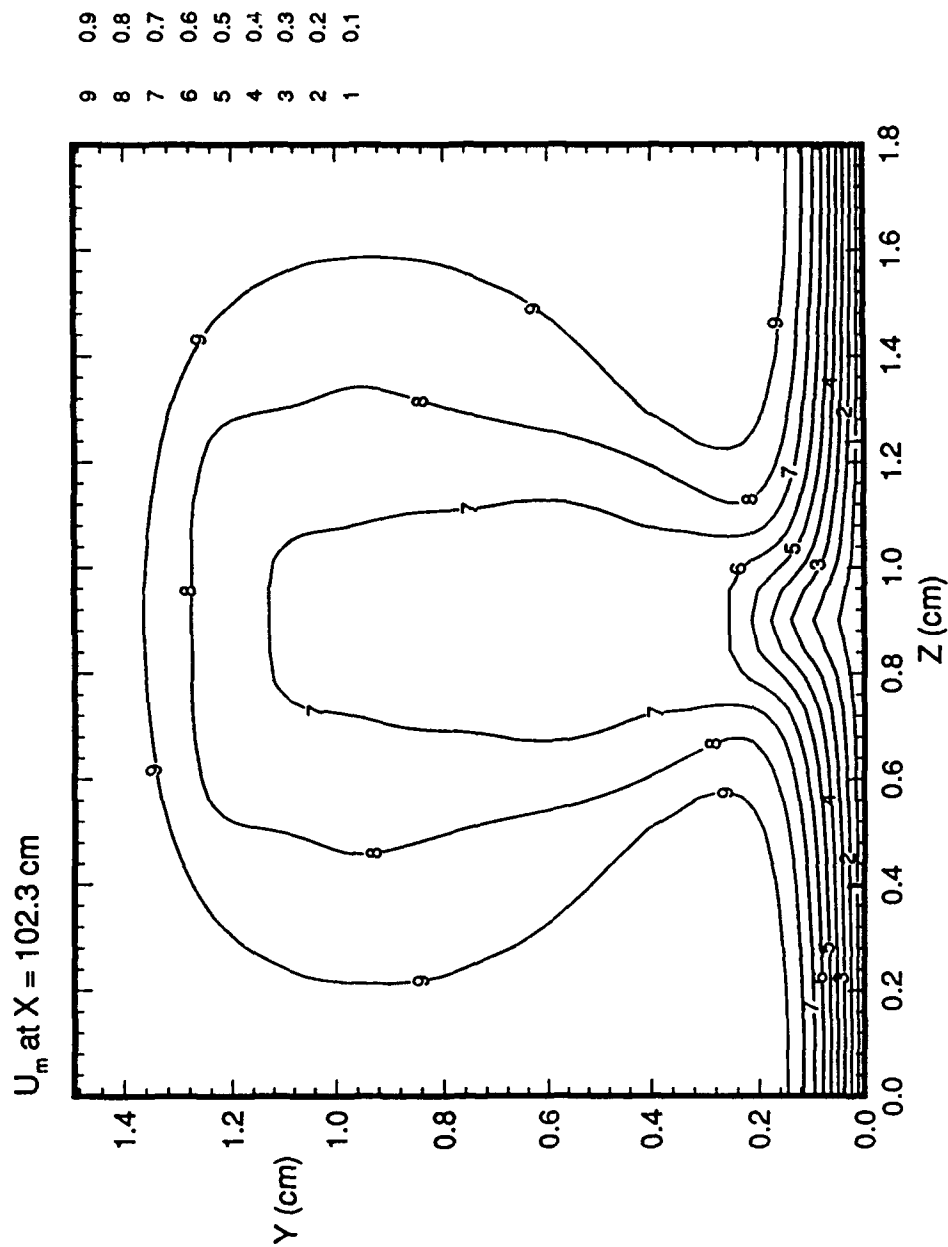


Fig. 13. Variation of time-averaged streamwise velocity in the Y-Z plane at X = 102.3 cm. Odd mode.

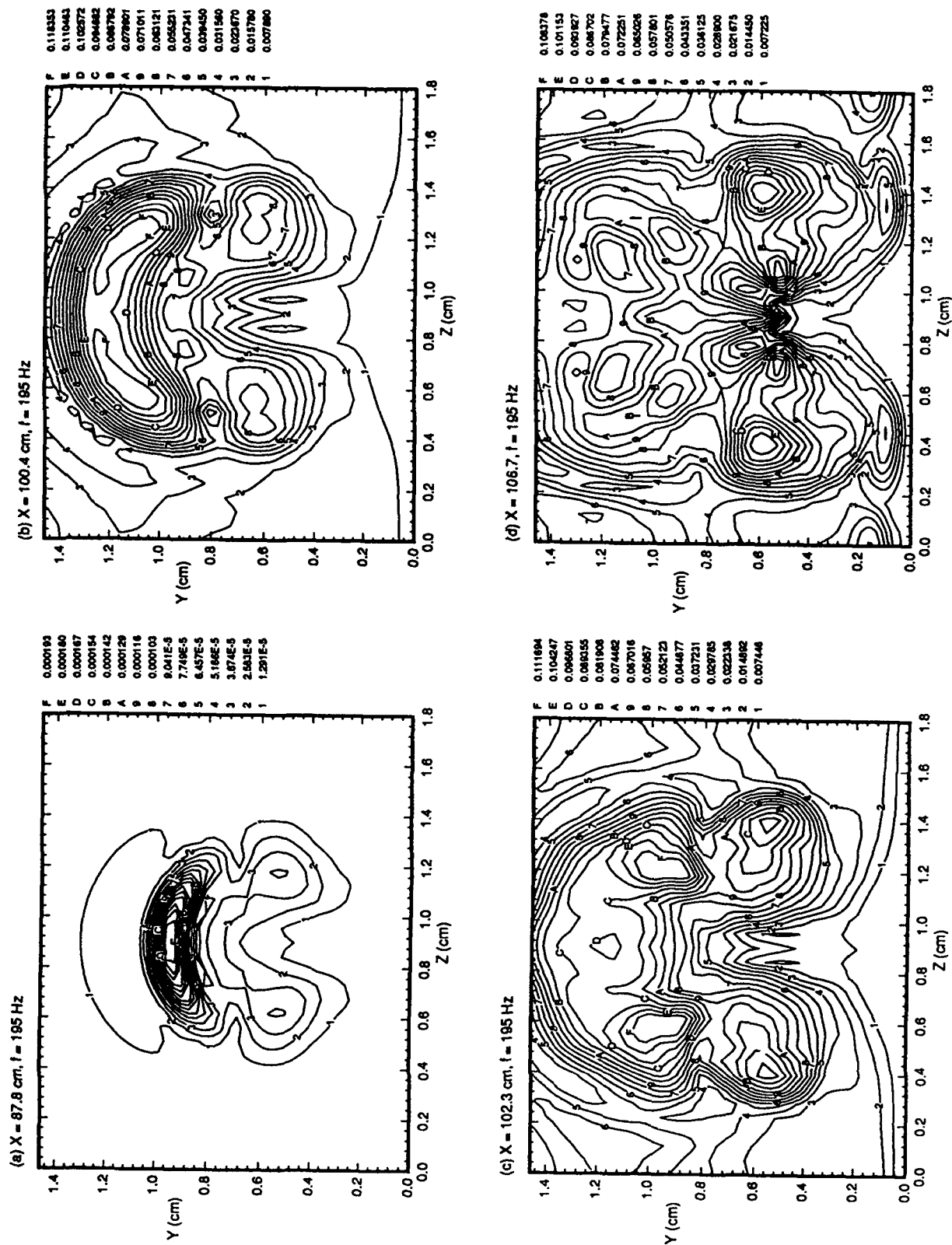


Fig. 14. Variation of rms streamwise velocity fluctuations in Y - Z plane for the even mode (a) $X = 87.8$ cm; (b) $X = 100.4$ cm; (c) $X = 102.3$ cm; (d) $X = 106.7$ cm.

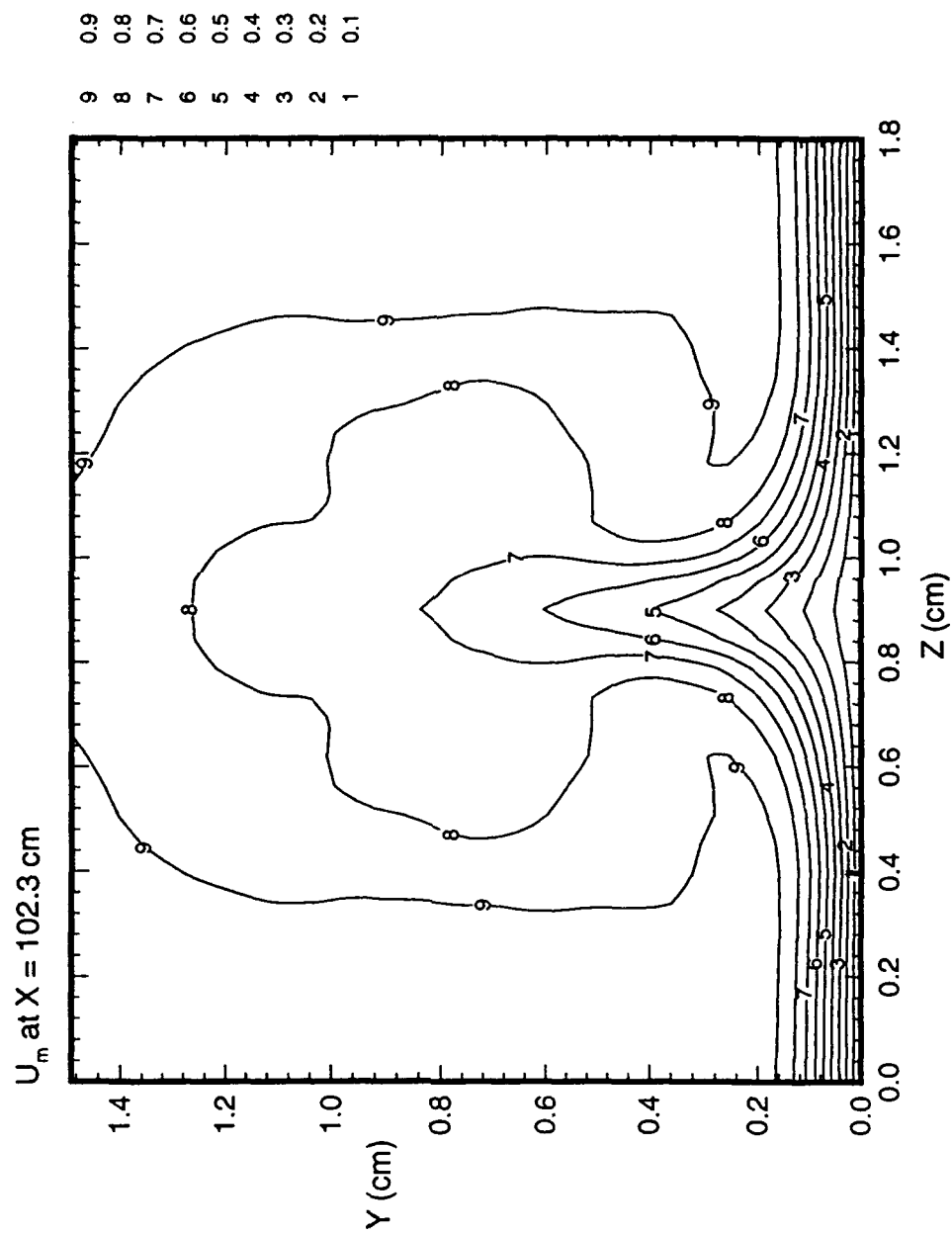


Fig. 15. Variation of the time-averaged streamwise velocity in y - z plane at $X = 102.3$ cm for the even mode.

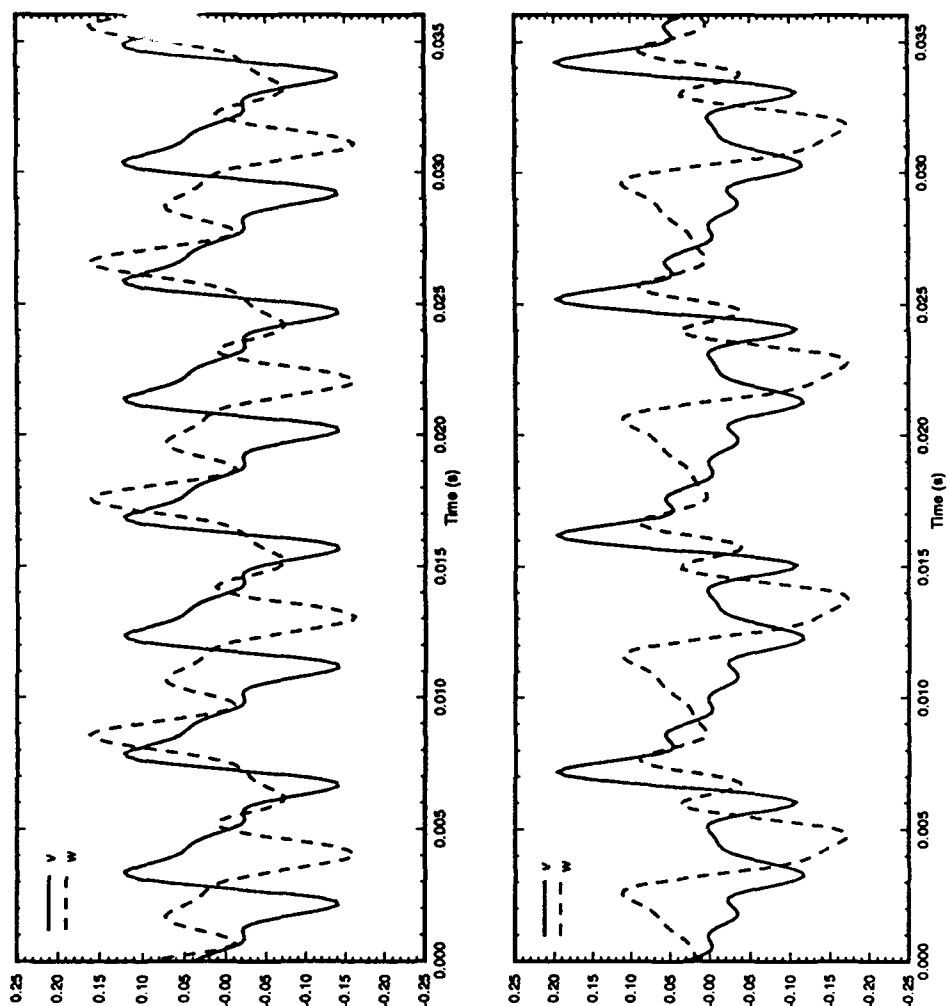
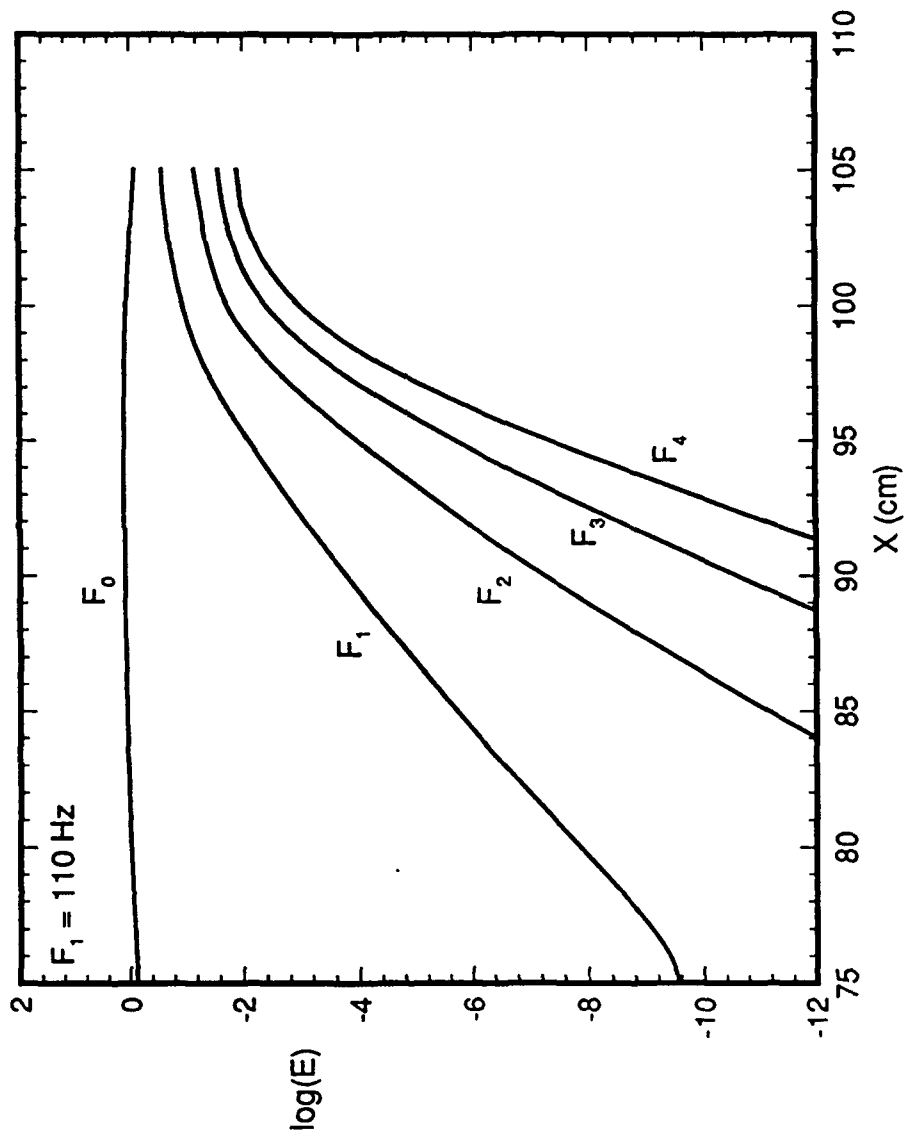
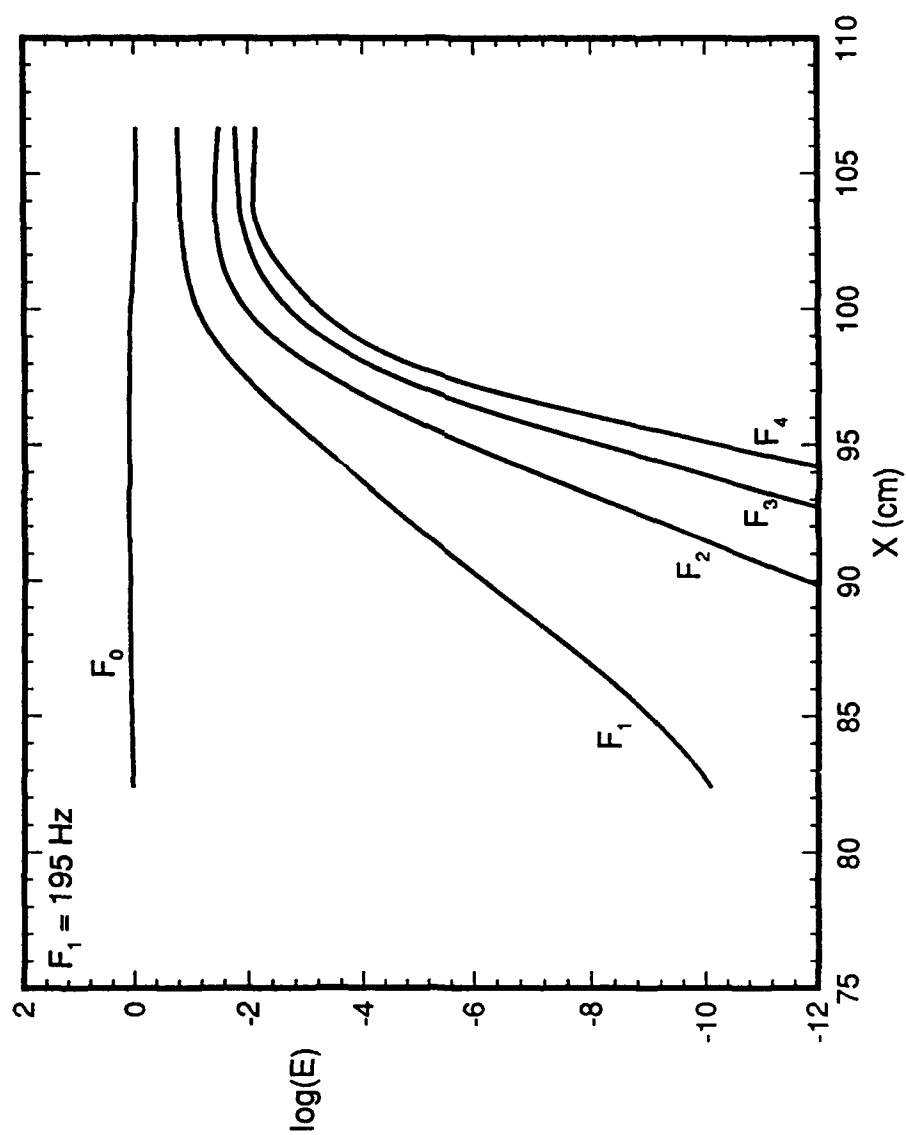


Fig. 16. Vertical and spanwise velocity fluctuations with time at $X = 105$ cm and $Y = 1.29$ cm. Upper graph for fluctuations at the peak. Lower graph for fluctuations at $Z = \lambda/4$ away from the peak.



(a) Sinuous Mode (odd)

Fig. 17. Energy associated with various frequencies.



(b) Varicose mode (even).

Fig. 17. Concluded.

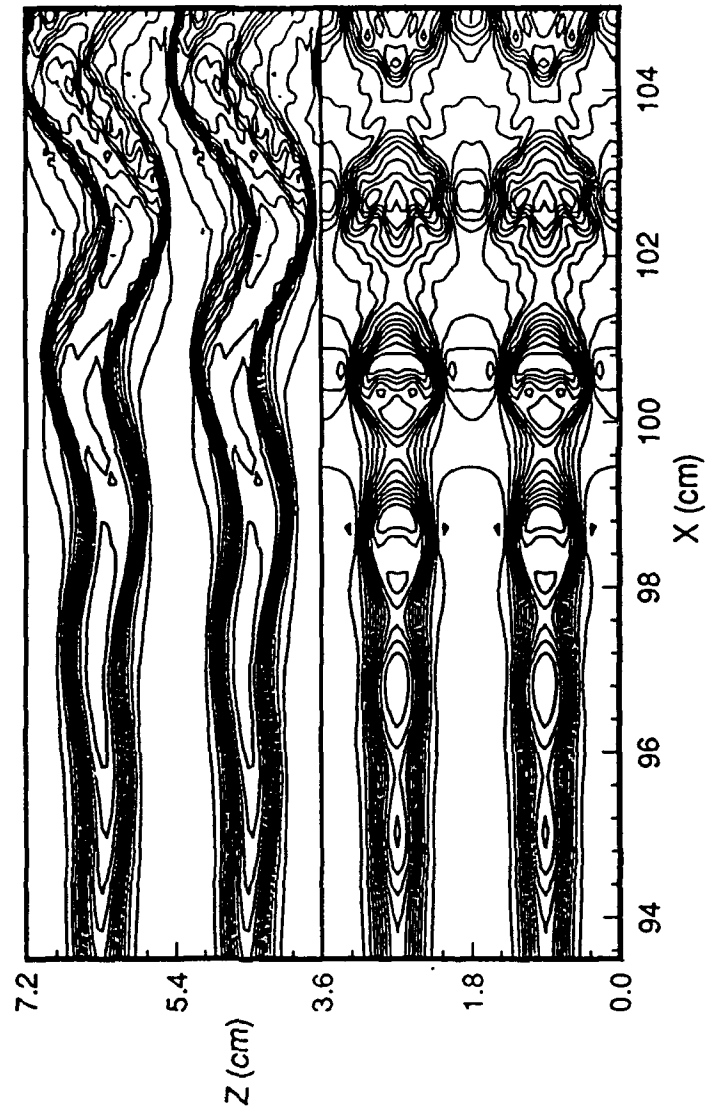


Fig. 18. Instantaneous streamwise velocity in the X - Z plane at $Y = 1.08$ cm. Upper half — sinusoidal mode (odd), Lower half — varicose mode (even).

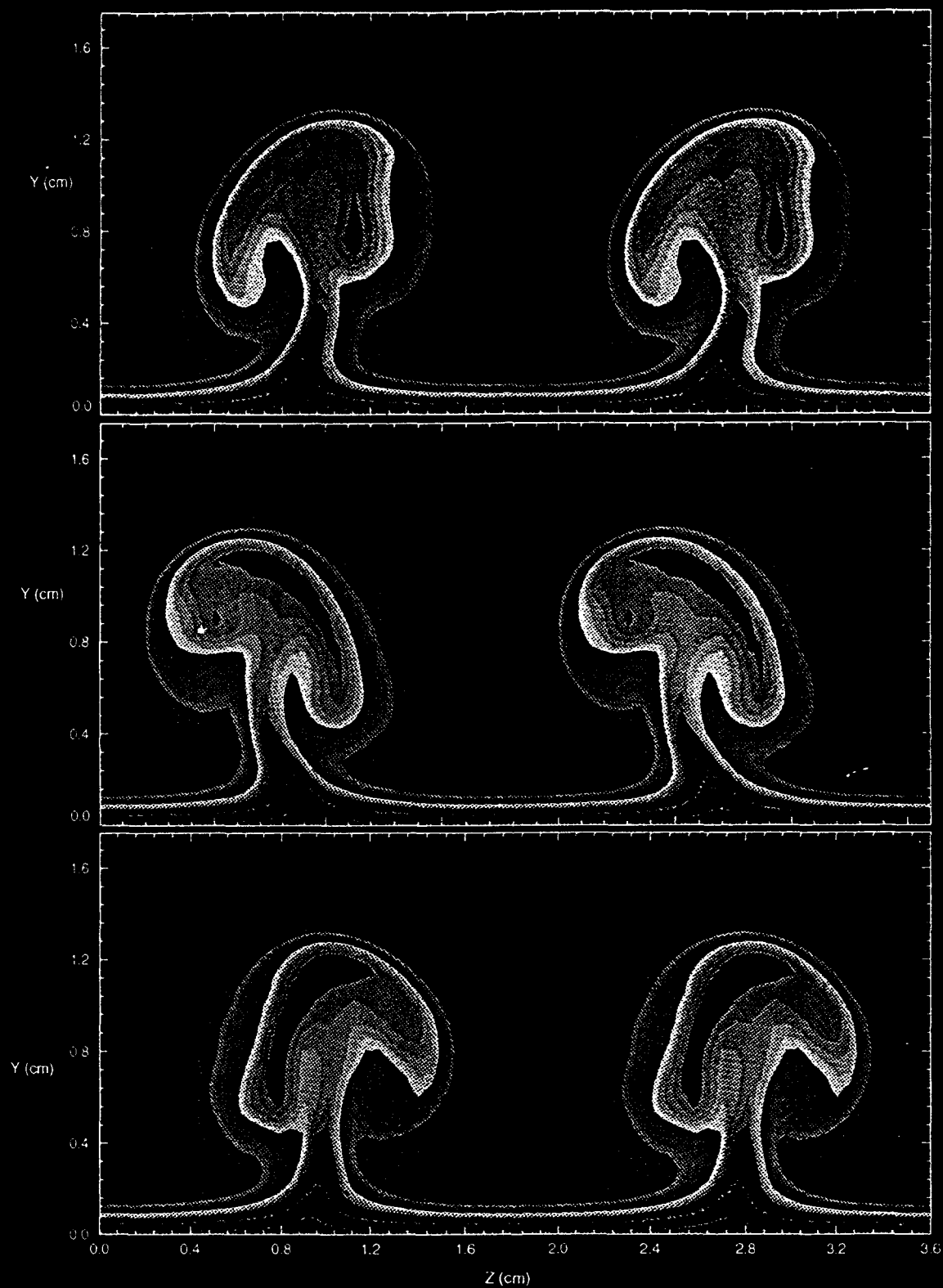


Fig. 19. Instantaneous streamwise velocity in the y - z plane for the sinuous mode ($f = 110$ Hz): top, $t = 0$; middle, $t = 2\pi/3\omega$, bottom, $t = 4\pi/3\omega$.

PART B

Crossflow Disturbances in Three-Dimensional Boundary Layers: Nonlinear Development, Wave Interaction and Secondary Instability

Abstract

Nonlinear stability of a model swept-wing boundary layer, subject to crossflow instability, is investigated by numerically solving the governing partial differential equations. The three-dimensional boundary layer is unstable to both stationary and traveling crossflow disturbances. Nonlinear calculations have been carried out for stationary vortices and the computed wall vorticity pattern results in streamwise streaks which resemble quite well with the surface oil-flow visualizations in swept-wing experiments. Other features of the stationary vortex development (half-mushroom structure, inflected velocity profiles, vortex doubling, etc.) are also captured in these calculations. Nonlinear interaction of the stationary and traveling waves is also studied. When initial amplitude of the stationary vortex is large as compared to the traveling mode, the stationary vortex dominates most of the downstream development. When the two modes have the same initial amplitude, the traveling mode dominates the downstream development owing to its higher growth rate. It is also found that, prior to laminar/turbulent transition, the three-dimensional boundary layer is subject to a high frequency secondary instability which is in agreement with the experiments of Poll (1985) and Kohama, Saric & Hoos (1991). The frequency of this secondary instability, which resides on top of the stationary crossflow vortex, is an order of magnitude higher than the frequency of the most amplified traveling crossflow mode.

1. Introduction

In swept-wing flows, chordwise pressure-gradient near the leading edge causes inviscid streamlines to be curved in the planes parallel to the wing surface. Associated with this streamline curvature is a pressure gradient which acts in a direction normal to the streamlines and introduces a secondary flow within the boundary-layer. This secondary flow, commonly known as crossflow, is subject to inviscid instability due to the presence of an inflection point (Gregory, Stuart & Walker 1955) and is the main cause of transition in swept-wing flows. Thus, this problem is not only of fundamental importance in fluid mechanics but also of prime significance in laminar flow control (LFC) design of swept-wings.

Crossflow instability often results in the formation of stationary corotating vortices commonly called crossflow vortices. This phenomenon is observed in swept-wing boundary layers as well as in other geometries such as rotating disks and cones. How the stationary crossflow vortices lead to turbulence remains unanswered. Traveling crossflow disturbances are also possible and the role of traveling vs. stationary disturbances is a question which needs to be investigated. Another problem which is of interest in swept-wing flows is the possibility of interaction between the inviscid crossflow disturbances and viscous streamwise instability. Crossflow disturbances are amplified in the negative pressure rise region near the wing leading edge, while Tollmien-Schlichting (TS) waves

(viscous instability of streamwise profiles) are amplified in the flat pressure region of the wing midchord. The possible interaction of these two types of disturbances may be quite significant in the successful design of LFC wings.

Experimental investigations into the nature of the swept-wing boundary-layer instability, at its linear and nonlinear stage, have been carried out by Bippes and coworkers (see, Bippes (1991), Müller & Bippes (1988), Müller (1989)) at DLR, by Saric and coworkers (see, Dagenhart *et al.* (1989), Saric, Dagenhart & Mousseux (1989), Kohama, Saric & Hoos (1991)) at Arizona State University and by Arnal and coworkers (see Arnal & Juillen (1987)) at ONERA/CERT. Experiments at DLR were performed on a swept-plate model with an imposed pressure gradient. A displacement body above the plate was used to generate the c_p distribution which varied almost linearly with chordwise distance. Saric and Arnal used infinite-swept aerofoils in their low-speed experiments.

Both stationary and traveling crossflow disturbances were observed in these experiments, as well as in the experiment of Poll (1985) on a swept cylinder. Müller & Bippes (1988) found that the stationary vortices, as well as traveling disturbances, reached nonlinear saturation in their experiment. However, they did not notice any explosive secondary instability leading to transition. On the other hand, Kohama, Saric & Hoos (1991) observed a high frequency secondary instability prior to transition in their swept-wing experiment where pressure gradient remained favorable ruling out any possibility of TS wave amplification. The frequency of this secondary instability was an order of magnitude higher than the frequency of the most amplified traveling disturbance given by the linear theory. They concluded that, even though the traveling crossflow disturbances are observed, the transition process in this three-dimensional boundary layer is dominated by the stationary vortices and the associated secondary instability. Poll (1985) had also observed a high frequency disturbance in his swept-cylinder experiment.

Müller & Bippes (1988) also studied the effect of free-stream turbulence on the instability behavior in their experiment. They found that at "low" levels (.05 percent) of free stream turbulence, stationary disturbances amplified to large amplitudes but these large amplitudes of the stationary vortices did not necessarily lead to early transition. The experiments performed in wind tunnels with higher turbulence levels (.15 and .3 percent) showed weaker growth of stationary disturbances but earlier transition due to stronger traveling disturbances. They concluded that traveling waves, and not the stationary vortices, play the major role in the transition process. Their experimental results also seem to suggest an early nonlinear interaction between stationary and traveling crossflow disturbances.

Theoretical investigations into linear and nonlinear stability of three-dimensional boundary layers have been carried out by Balachandar, Streett & Malik (1992), Fischer & Dallmann (1991), Malik (1986), Meyer & Kleiser (1988) and Reed (1987). Fischer and Dallman used secondary instability theory and Meyer and Kleiser used direct simulation of Navier-Stokes equations to study the swept-

plate experiment of Müller & Bippes (1988). Fischer and Dallmann argued that the traveling disturbances observed in the DLR experiment are secondary disturbances of the mean flow modulated by the stationary vortices and should not be thought of as the primary instability of the three-dimensional boundary-layer flow. Direct numerical simulation of Meyer and Kleiser found nonlinear equilibrium states for stationary as well as traveling disturbances, in agreement with the DLR experiment. Similar equilibrium states for stationary vortices were computed by Malik (1986) in rotating-disk boundary layer. Balachandar, Streett & Malik (1992) performed a secondary instability analysis of the rotating-disk boundary layer where the stationary vortices constituted the primary instability. They were able to find a high-frequency secondary instability similar to the one observed by Kohama (1984,1987) in a rotating-disk boundary layer.

All these experimental and theoretical investigations consider a class of mean flows which is only unstable to inflectional crossflow disturbances and do not support TS wave amplification. Results from various experiments appear to suggest that for this class of flow, there are at least two possible scenarios for transition. If free-stream turbulence level is very small, i.e., the initial amplitude of the nonstationary disturbances is small relative to the stationary disturbances, which most certainly are introduced at local surface imperfections, then stationary disturbances dominate the initial stage of the disturbance growth leading to a high-frequency secondary instability resulting in final breakdown. When the initial amplitude of the traveling modes is not small, nonlinear interaction between these traveling modes and stationary vortices is present and the character of the final breakdown is influenced by the relative amplitudes of the stationary vortices and the traveling modes. The other class of flow where TS waves could amplify is also of technological importance but has not been studied either experimentally or theoretically.

The objective of this research is to study various wave-interaction mechanisms and laminar-flow breakdown in three-dimensional boundary layers. Previous linear and nonlinear theoretical investigations have been performed by using parallel-flow approximation and have been local in nature. This study includes nonparallel effects and sets up the problem within the framework of nonlinear parabolized stability equations (PSE). Intermodal interaction and the effect of initial conditions can also be studied by using this approach. Basic insight into the physical mechanisms involved in swept-wing flow transition can be achieved by considering simple model flows. One such flow is the swept Hiemenz flow in which the interaction of stationary and traveling crossflow disturbances can be studied. In this paper we study linear and nonlinear crossflow disturbances as well as the interaction between stationary and traveling modes. We also study secondary instability of the three-dimensional mean flow modulated by the stationary vortices. Section 2 describes the basic flow for the swept Hiemenz problem and the associated PSE analysis is given in § 3. The results for linear and nonlinear stability analysis and wave interactions are given in § 4. Section 5 describes the results from secondary instability analysis and the conclusions are given in § 6.

2. The Swept Hiemenz Problem

The flow past a circular cylinder, outside the viscous boundary-layer, can be represented as

$$U_{\infty} = cx^* + c_1x^{*3} + c_2x^{*5} + \dots \quad (2.1)$$

where U_{∞} is the velocity along the coordinate x^* and c, c_1 , etc. are constants. In the two-dimensional stagnation-point flow, only the first term in the series (2.1) is retained and, hence, the velocity U_{∞} increases linearly with distance x^* , i.e.,

$$U_{\infty} = cx^* \quad (2.2)$$

If we consider the Cartesian coordinate system x^*, y^*, z^* , then (2.2) gives the far-field ($y^* \rightarrow \infty$) solution of the impinging flow on a plate along x^* which we define here by $y^* = 0$. The associated viscous problem was first investigated by Hiemenz who found an exact solution which is named after him. This stagnation flow was found to be stable to infinitesimally small disturbances propagating along z^* by Wilson & Gladwell (1978).

The swept Hiemenz problem is constructed by introducing a velocity component W_{∞} along the z^* axis which amounts to changing the inclination of the impinging stream with respect to z^* . The flow is symmetric about the line $x^* = 0$ which is called the attachment-line. Linear and nonlinear stability of the attachment-line boundary-layer has been studied by Hall, Malik & Poll (1984) and Spalart (1988). In this paper we study the stability of this flow for $x^* > 0$ as was recently done by Spalart (1989) using full Navier-Stokes equations.

2.1. The basic flow

We consider the flow of a viscous incompressible fluid of kinematic viscosity ν . Let $\ell = \sqrt{\nu/c}$ be a typical thickness of the boundary layer which is used here as the length scale. We note that ℓ is independent of x^* . Thus, we have the scaled coordinates x, y, z given as

$$(x, y, z) = \left(\frac{x^*}{\ell}, \frac{y^*}{\ell}, \frac{z^*}{\ell} \right).$$

We also define two Reynolds numbers R and \bar{R} where

$$R = \frac{U_{\infty}\ell}{\nu} \quad (2.3)$$

$$\bar{R} = \frac{W_{\infty}\ell}{\nu} \quad (2.4)$$

From (2.2) and (2.3), it follows that

$$R = \frac{x^*}{\ell} = x \quad (2.5)$$

The local angle of the inviscid streamline θ , with respect to the x -axis, is given as

$$\theta = \text{atan}\left(\frac{W_\infty}{U_\infty}\right) = \text{atan}\left(\frac{\bar{R}}{R}\right) \quad (2.6)$$

We now look for a solution to the Navier-Stokes equations which satisfies the following conditions

$$u^* = v^* = w^* = 0, \quad y^* = 0 \quad (2.7)$$

$$u^* \rightarrow U_\infty, \quad w^* \rightarrow W_\infty, \quad y^* \rightarrow \infty \quad (2.8)$$

where u^*, v^*, w^* are velocity components in the x^*, y^*, z^* directions, respectively. It is convenient to define a stream function Φ so that

$$u^* = \frac{\partial \Phi}{\partial y^*}, \quad v^* = -\frac{\partial \Phi}{\partial x^*}$$

and

$$\Phi = x^* \sqrt{c\nu} f(y).$$

If we use W_∞ as the velocity scale, then

$$\bar{u} = \frac{u^*}{W_\infty} = \frac{x}{R} f'(y) \quad (2.9)$$

$$\bar{v} = \frac{v^*}{W_\infty} = -\frac{1}{R} f(y) \quad (2.10)$$

Similarly,

$$\bar{w} = \frac{w^*}{W_\infty} = g(y) \quad (2.11)$$

where f and g are governed by the ordinary differential equations

$$f''' + ff'' + (1 - f'^2) = 0 \quad (2.12)$$

$$g'' + fg' = 0 \quad (2.13)$$

where primes denote differentiation with respect to y .

The mean flow derivatives needed in the stability analysis below can be written as

$$\bar{u}_y = \frac{x}{R} f'', \quad \bar{u}_{yy} = \frac{x}{R} f'''$$

$$\bar{v}_y = -\frac{1}{R} f', \quad \bar{v}_{yy} = -\frac{1}{R} f''$$

$$\bar{w}_y = g', \quad \bar{w}_{yy} = g''$$

$$\bar{u}_x = \frac{1}{R} f'$$

Numerical solution of (2.12) and (2.13) thus yields the mean flow and its derivatives without any additional approximation and the boundary-layer thickness does not vary with x .

3. PSE Analysis for 3D Boundary Layers

Parabolized stability equations (PSE) for linear and nonlinear disturbances in two-dimensional boundary layers have been used by Herbert (1991) and Bertolotti, Herbert & Spalart (1992) for incompressible flow where they used streamfunction formulation of the governing equations. In the present three-dimensional (3D) boundary-layer study, we follow the work of Chang *et al.* (1991) for compressible flow and formulate the incompressible stability problem using primitive variables in Cartesian coordinates x, y , and z . The basic flow is perturbed by fluctuations in the flow, i.e., the total field can be decomposed into a mean value (solution of (2.12-2.13)) and a perturbation quantity

$$u = \bar{u} + \tilde{u}, \quad v = \bar{v} + \tilde{v}, \quad w = \bar{w} + \tilde{w}, \quad p = \bar{p} + \tilde{p} \quad (3.1)$$

where p is the pressure. Substituting (3.1) into the incompressible Navier-Stokes equations and subtracting from it the steady mean flow, we obtain the nonlinear disturbance equations as

$$\Gamma \frac{\partial \phi}{\partial t} + A \frac{\partial \phi}{\partial x} + B \frac{\partial \phi}{\partial y} + C \frac{\partial \phi}{\partial z} + D \phi - \left[E_x \frac{\partial^2 \phi}{\partial x^2} + E_y \frac{\partial^2 \phi}{\partial y^2} + E_z \frac{\partial^2 \phi}{\partial z^2} \right] = F \quad (3.2)$$

where the left hand side contains only linear operators operating on the disturbance vector $\phi = (\tilde{u}, \tilde{v}, \tilde{w}, \tilde{p})$ and the right-hand-side forcing vector F is due to non-linear interaction and includes all non-linear terms associated with the disturbances. The right hand side is given as

$$F = -\tilde{A} \frac{\partial \phi}{\partial x} - \tilde{B} \frac{\partial \phi}{\partial y} - \tilde{C} \frac{\partial \phi}{\partial z} \quad (3.3)$$

In the above, Γ is the diagonal matrix $[1, 1, 1, 0]$ while A, B, C are given as

$$A = \begin{bmatrix} \bar{u} & 0 & 0 & 1 \\ 0 & \bar{u} & 0 & 0 \\ 0 & 0 & \bar{u} & 0 \\ 1 & 0 & 0 & 0 \end{bmatrix}, \quad B = \begin{bmatrix} \bar{v} & 0 & 0 & 0 \\ 0 & \bar{v} & 0 & 1 \\ 0 & 0 & \bar{v} & 0 \\ 0 & 1 & 0 & 0 \end{bmatrix}, \quad C = \begin{bmatrix} \bar{w} & 0 & 0 & 0 \\ 0 & \bar{w} & 0 & 0 \\ 0 & 0 & \bar{w} & 1 \\ 0 & 0 & 1 & 0 \end{bmatrix},$$

and $\tilde{A}, \tilde{B}, \tilde{C}$ are similar to A, B, C except that quantities with over bar are replaced with \sim and all ones are dropped. The coefficient matrices D, E_x, E_y, E_z are given as

$$D = \begin{bmatrix} \bar{u}_x & \bar{u}_y & 0 & 0 \\ \bar{v}_x & \bar{v}_y & 0 & 0 \\ \bar{w}_x & \bar{w}_y & 0 & 0 \\ 0 & 0 & 0 & 0 \end{bmatrix}$$

$$E_x = E_y = E_z = \begin{bmatrix} \frac{1}{R} & 0 & 0 & 0 \\ 0 & \frac{1}{R} & 0 & 0 \\ 0 & 0 & \frac{1}{R} & 0 \\ 0 & 0 & 0 & 0 \end{bmatrix}.$$

We assume that the given disturbance is periodic in time and in the spanwise direction; thus, the disturbance function ϕ can be expressed by the following Fourier series

$$\phi = \sum_{m=-\infty}^{\infty} \sum_{n=-\infty}^{\infty} \chi_{mn}(x, y) e^{i(n\beta z - m\alpha t)} \quad (3.4)$$

Here, the frequency ω and wave number β are chosen such that the longest period and wave length are $2\pi/\omega$ and $2\pi/\beta$ in the temporal and spanwise domains, respectively. For most stability problems of interest, it is sufficient to truncate (3.4) to only a finite number of modes

$$\phi = \sum_{m=-M}^{M-1} \sum_{n=-N}^{N-1} \chi_{mn}(x, y) e^{i(n\beta z - m\alpha t)} \quad (3.5)$$

where M and N represent one-half the number of modes kept in the truncated Fourier series. Substituting (3.5) in (3.2) we obtain governing equations for χ_{mn} which are elliptic. In order to facilitate the solution of these equations we decompose the disturbance into a fast varying wave-like part and a slowly varying shape function and write χ_{mn} as

$$\chi_{mn}(x, y) = \Psi_{mn}(x, y) \mathcal{A}_{mn}(x) \quad (3.6a)$$

$$\mathcal{A}_{mn}(x) = e^{i \int_{x_0}^x \alpha_{mn}(\xi) d\xi} \quad (3.6b)$$

where Ψ_{mn} is the shape function ($\hat{u}_{mn}, \hat{v}_{mn}$, etc.) for the Fourier mode (m, n, β) and α_{mn} is the associated streamwise (complex) wave number. With a proper choice of α_{mn} in (3.6b), the arbitrariness in (3.6a) can be removed and the equations for Ψ_{mn} can be parabolized. In other words, α_{mn} is chosen such that variation of Ψ_{mn} with x is minimized which allows the approximation $\partial^2 \Psi_{mn} / \partial x^2 = 0$. The parabolized stability equations (PSE) for the shape function of a single Fourier mode (m, n) can be written as

$$\bar{G}_{mn} \Psi_{mn} + \bar{A}_{mn} \frac{\partial \Psi_{mn}}{\partial x} + \bar{B}_{mn} \frac{\partial \Psi_{mn}}{\partial y} = E_y \frac{\partial^2 \Psi_{mn}}{\partial y^2} + F_{mn} / \mathcal{A}_{mn} \quad (3.7)$$

where matrices \bar{E}_{mn} , \bar{A}_{mn} and \bar{B}_{mn} are given by

$$\bar{G}_{mn} = -im\omega\Gamma + i\alpha_{mn}A + in\beta C + D - E_x \left(i \frac{d\alpha_{mn}}{dx} - \alpha_{mn}^2 \right) + n^2 \beta^2 E_z$$

$$\bar{A}_{mn} = A - 2i\alpha_{mn}E_x$$

$$\bar{B}_{mn} = B$$

The non-linear forcing function F_{mn} is the Fourier component of the total forcing, F , and can be evaluated by the Fourier series expansion

$$F(x, y, z, t) = \sum_{m=-M}^{M-1} \sum_{n=-N}^{N-1} F_{mn}(x, y) e^{i(n\beta z - m\alpha x)}. \quad (3.8)$$

The Fourier decomposition of (3.8) can be done by using the Fast Fourier Transform (FFT) of F , which is evaluated numerically in the physical space.

The PSE equations (3.7) can be used to study nonlinear interaction of various modes (e.g., cross-flow/crossflow, crossflow/TS, etc.) or one can study the onset of transition to turbulence provided appropriate initial conditions are prescribed. For small disturbances, F can be neglected and one obtains linear PSE equations (after dropping the subscript 11)

$$\bar{G}\Psi + \bar{A}\frac{\partial\Psi}{\partial x} + \bar{B}\frac{\partial\Psi}{\partial y} = E_y\frac{\partial^2\Psi}{\partial y^2} \quad (3.9)$$

which can be solved to study the effect of nonparallel flow or that of initial conditions. If nonparallel effect is ignored, then (3.9) essentially reduces to the Orr-Sommerfeld equation.

The streamwise wavenumber in (3.6b) needs to be determined in order to solve the equations by a marching scheme. This procedure is given in Chang et al. (1991). Here we briefly describe it for the linear equation (3.9). In this case, the evolution of the shape function is monitored during the process of marching and the wavenumber is updated by local iterations at a given x according to the change in Ψ . At a given location x_1 , let the streamwise wavenumber be given by α_1 and then express ϕ as

$$\phi(x, y, z, t) = \Psi(x, y) e^{i\left(\int_{x_1}^x \alpha_1 d\xi + \beta z - \alpha t\right)}. \quad (3.10)$$

The change of the shape function Ψ can be approximated by the following Taylor series expansion truncated to the first order

$$\Psi(x, y) = \Psi_1 + \frac{\partial\Psi_1}{\partial x}(x - x_1) + \dots$$

where Ψ_1 is the shape function at $x = x_1$. To an accuracy of $O(x - x_1)$, the above equation can be further expressed as

$$\Psi(x, y) = \Psi_1 e^{\int_{x_1}^x \frac{1}{\Psi_1} \frac{\partial\Psi_1}{\partial x} d\xi}. \quad (3.11)$$

Substituting (3.11) into (3.10), we have the "effective" wavenumber in the vicinity of x_1 given by

$$\alpha = \alpha_1 - i \frac{1}{\Psi_1} \frac{\partial \Psi_1}{\partial x} \quad (3.12)$$

The real part of this effective wavenumber represents the phase change of the disturbance while the imaginary part gives the growth rate. A disturbance is unstable if the imaginary part is less than zero. Since the shape function vector Ψ_1 depends upon y and contains four dependent variables (\hat{u}, \hat{v} , etc.), the value of α computed by (3.12) will be a function of the y coordinate and the selected dependent variable. One can, for example, use the shape function \hat{u} and the y location where \hat{u} reaches its local maximum to update the wavenumber at any given x station as the disturbance evolves downstream. An alternative which is used here is to consider the following integral condition,

$$\alpha_{\text{new}} = \alpha_{\text{old}} - \frac{i \int q^\dagger \cdot \frac{\partial q}{\partial x} dy}{\int |q|^2 dy} \quad (3.13)$$

which removes the dependence of α on y . If q is a particular component of Ψ_1 then the dependence of α on Ψ_1 is retained in (3.13). For three-dimensional boundary layers we choose q to be a vector with components $(\hat{u}, \hat{v}, \hat{w})$. Equation (3.13) is used in the iterative solution of (3.9) until the second term in (3.13) vanishes to a prescribed tolerance. An additional condition (Chang *et al.* 1991, Malik & Li 1993) needs to be satisfied in order to obtain solution of (3.7) by the space marching approach.

Numerical solution of the parabolized stability equations requires discretization in both x and y directions. We discretize the streamwise derivative by a backward Euler step and wall-normal derivatives by fourth-order accurate compact differences (see, Malik, Chuang & Hussaini (1982)). Homogeneous boundary conditions at the wall and in the free stream are imposed. The initial conditions are obtained by a local approximation to (3.9) and by solving the associated eigenvalue problem. Since the wave information is absorbed in the wavenumber α (3.6b), one needs to use a few marching steps per wavelength to obtain an accurate solution of the wave evolution. Calculations for two-dimensional boundary layers show that PSE results with only 3 steps per wave length agree quite well with very accurate Navier-Stokes computations using 60 grid points per wavelength (see, Joslin, Streett and Chang 1992).

4. Linear and Nonlinear Stability Analysis and Wave Interaction

4.1 Quasi-parallel linear stability

In order to determine the relevant physical parameter space, it is appropriate to first give some results from quasi-parallel linear stability theory. We consider two cases: $\bar{R} = 250$ and 500. Hall, Malik & Poll (1984) found that the attachment-line boundary-layer ($x = 0$) is stable to infinitesimal disturbances up to $\bar{R} = 583.1$. Thus, for the two cases considered here, the attachment-line

boundary-layer is stable. In the present study, we are interested in the crossflow disturbances which will become unstable away from the attachment-line ($x \gg 1$). Figure 1 shows the mean velocity profiles in directions tangential and across the inviscid stream at an R of 500 and $\bar{R} = 500$. The velocity profiles U_t and U_c are defined as

$$\begin{aligned} U_t &= \bar{u} \cos \theta + \bar{w} \sin \theta \\ U_c &= \bar{u} \sin \theta - \bar{w} \cos \theta \end{aligned}$$

where the streamline angle θ is defined in (2.6). These velocity profiles have been scaled with spanwise inviscid velocity W_∞ . It is clear from (2.6) that θ decreases with R or x as the flow turns away from the attachment-line towards the free-stream direction. This is depicted in figure 2 where the angle θ , along with the crossflow Reynolds number R_{cf} (defined below), is plotted for both $\bar{R} = 250$ and 500.

Crossflow instability is associated with the inflectional velocity profile U_c which, for swept wings, is positive towards the center of curvature of the streamline. The flow becomes unstable when crossflow Reynolds number $R_{cf} \geq 40$ where R_{cf} is defined by

$$R_{cf} = \frac{\bar{U}_c \delta_{.1}}{\nu} \quad (4.1)$$

where \bar{U}_c is the maximum value of the crossflow velocity U_c and $\delta_{.1}$ is the thickness where the crossflow velocity has dropped to 10% of \bar{U}_c . Distribution of the crossflow Reynolds number R_{cf} is given for the two cases in figure 2. The value of R_{cf} exceeds about 50 at $R = 200$ and, hence, the instability will onset at $R < 200$ for both cases. The maximum value of R_{cf} is about 150 for $\bar{R} = 250$ and about 270 for $\bar{R} = 500$. In swept-wing flows, transition usually occurs where R_{cf} becomes of $O(200)$.

Figure 3 presents results for integrated growth,

$$\ln(A/A_0) = \int_{R_0}^R \sigma_p dR \quad (4.2)$$

using the quasi-parallel growth rate $\sigma_p = -\alpha_i$. Calculations are performed for stationary as well as traveling disturbances with frequency $F = .75 \times 10^{-4}$ (where $F = 2\pi\nu f / W_\infty^2$, f being the frequency in hertz) at both \bar{R} . These calculations are performed for a fixed spanwise wavenumber of 0.4 which is close to, but no quite (see figure 4 below), the most amplified wave number for the flow under study. It is clear that traveling disturbances amplify more than the stationary disturbances according to linear theory. However, stationary disturbances are found to dominate when experiments are performed in low-disturbance wind tunnels. This is due to the lower initial amplitude of traveling modes (see the work of Choudhari & Streett (1990) on the receptivity of stationary and traveling disturbances).

The variation of spatial growth rate with wavenumber β is given in figure 4 for the two frequencies. There are two curves associated with $F = .75 \times 10^{-4}$, one with positive β and another with negative β , the latter with smaller growth rates. The stationary vortex and $\beta > 0$ traveling disturbance has peak growth rate at $\beta \approx .35$ as shown in the figure for $R = 300$. In the downstream, the peak shifts to higher wavenumbers and lies, for example, at $\beta \approx .45$, $R = 650$. The two families of unstable traveling disturbances are further shown in figure 5 where the growth rate of the most amplified (among various wave orientations) disturbance is plotted as a function of frequency. The family with high growth rates has its wave vector oriented at positive angles with respect to the inviscid flow streamline (angles measured from the convex side) while the family with lower growth rates has its wave vector oriented at negative angles. The relative sense of the two modes depends upon the direction of the crossflow with the more amplified mode always oriented opposite to the crossflow direction. In both cases, the direction of the group velocity lies at small angles to the inviscid streamline direction. Thus, the disturbance energy propagates downstream for both modes as also noted by Mack (1985). The traveling mode with lower growth rate may be important in the nonlinear stage and its interaction with the more amplified traveling mode may also induce stationary crossflow vortices when other stimuli, e.g., wall roughness, are absent. Furthermore, these two traveling modes along with stationary vortex mode constitute a possible resonant triad which may be relevant in the transition process.

4.2 Nonparallel effects

We now compare the quasi-parallel growth rate results with those obtained by solving linear PSE equations (Eq. (3.9)). Figure 6(a) shows the results for $\bar{R} = 250$ for stationary vortices while figure 6(b) shows the results for a frequency of $F = .75 \times 10^{-4}$. In case of PSE, different growth rate results are obtained for \hat{u} , \hat{v} and \hat{w} components of velocity. At low R (between 200 and 400) there is considerable difference between these growth rates with \hat{u} growth higher than \hat{v} and \hat{w} but the latter two approach the same value at higher Reynolds numbers. Figure 7 shows the growth rate results for $\bar{R} = 500$. In this case the qualitative trends are the same but there is less difference between the three growth rates. The quasi-parallel growth rate is, in general, close to the growth rate based upon \hat{w} component, except at lower Reynolds numbers where it lies somewhere in between the three growth rates. Thus, one can not make a strong statement about nonparallel effects except that they are more pronounced at lower \bar{R} and that they are destabilizing if measured by the chordwise velocity component. The growth rate can also be defined based upon the total disturbance energy which accounts for all the velocity components and growth rates based upon this definition suggests that nonparallel effect is usually destabilizing, but there may be some exceptions. Spalart (1989) pointed out that the growth rates from his simulation were very close to the quasi-parallel results and that the agreement was better at lower Reynolds numbers (R) than at higher

Reynolds numbers. Figure 7(a) shows that this is true for the case he ran ($\bar{R} = 500, F = 0$), but it is not a general statement as is evident from the comparison of Figs. 6 and 7.

Our results for $\beta = .4$ and $\bar{R} = 500$ are compared with linearized Navier-Stokes computation of Streett (1993) in figure 8. Streett performed spatial simulations and solved the full linearized system where the disturbances were introduced by spanwise periodic steady suction and blowing. After the initial transients die out, the agreement between the two calculations is excellent and it remains so for a large chordwise extent. Good agreement was also found with the results of Spalart (1989) (Malik & Li (1992)). The agreement with full Navier-Stokes solution shows that PSE approximation introduces negligible error in our study of the crossflow vortices as disturbance growth rate is a sensitive quantity and any error would have shown up in growth rate results.

4.3 Nonlinear development of stationary crossflow vortices

Navier-Stokes simulations by Malik (1986) for rotating-disk flow and by Meyer & Kleiser (1988) for a Falkner-Skan-Cooke boundary layer showed nonlinear saturation of crossflow vortices. Both these calculations employed temporal approach and, therefore, ignored nonparallel effects. Here we present spatial nonlinear calculations for $\bar{R} = 500$ using PSE. Initial conditions for the stationary vortex with $\beta = .4$ were prescribed at $R = 186$. It was assumed that the vortex shape is given by the linear eigenfunction at that Reynolds number and that the maximum disturbance amplitude ($\max(\hat{u}^2 + \hat{w}^2)^{1/2}$) is .001 W_∞ . Figure 9 gives the computed total perturbation wall vorticity distribution

$$\left(\sqrt{\left(\frac{\partial u}{\partial y}\right)^2 + \left(\frac{\partial w}{\partial y}\right)^2} - \sqrt{\left(\frac{\partial \bar{u}}{\partial y}\right)^2 + \left(\frac{\partial \bar{w}}{\partial y}\right)^2} \right)$$

which shows streamwise striations starting at $R = 350$. The green color indicates negative values while the red indicates positive. The perturbation wall vorticity values are very small initially and the signal becomes noticeable (strong) only at R of about 420. As we will show later, the disturbance amplitude at this location has already reached about 4 percent. Hence, when these vortices are observed in a flow visualization experiment it is almost certain that they have entered the nonlinear stage with growth rates somewhat smaller than that given by the linear theory. These striations are evident in almost all crossflow experiments (Gray (1952), Gregory, Stuart & Walker (1955), Poll (1985), Saric, Daganhart & Mousseux (1989)) and result due to variation in the wall shear caused by stationary vortices. These vortices make a small angle ($4-5^\circ$) with respect to the inviscid free stream.

Figure 10 shows the contours of u velocity in y - z plane at various Reynolds numbers ($R = 400, 500, 600$ and 650). Two spanwise wavelengths are shown and the y coordinate has been stretched for clarity. Crossflow vortices appear to result in a half-mushroom-like structure which is shown

exaggerated in the figure. The actual structure is much more flat as shown in figure 11 drawn to scale. Initially the boundary-layer thickness is constant in z ; however, as the crossflow instability rolls up into vortices, there appear regions of low and high velocity and, therefore, the boundary-layer thickness varies considerably in the span as, for example, seen for $R = 600$. In this case the variation is as much as by a factor of about 4.

There is a region near $z = 10$ and 25 (for $R = 600$) where the fluid is pushed towards the wall while it is pushed away from the wall near $z = 5$ and 20 . It is these low velocity regions at $z = 5$ and 20 where oil accumulates in a flow visualization experiment resulting in wall streaks such as those shown in figure 9. The half-mushroom structure observed in figure 10 is the result of the asymmetry induced by the crosswind. In two-dimensional flow over a concave wall which is subject to centrifugal instability, a full mushroom structure appears as experimentally observed by Swearingen & Blackwelder (1987) and Peerhossaini & Wesfreid (1988).

Figure 12 shows a velocity vector plot in the y - z plane at fixed R of 650. The velocities have been projected onto a cross-section normal to the vortex axis. An insight into the crossflow vortex structure may be achieved by releasing die particles at some location within the flow field and following their paths as they are carried through the fluid in the y - z plane. Two particles are injected at about $z = 22$ but one is released very near the wall while the other is released at $y = 1.7$. The latter particle rolls into a big vortex centered at about $y = 2.5$ and $z = 12$. This is the primary crossflow vortex. There is a second tiny vortex near the wall centered at about $y = 1$ and $z = 8$ to which the particle released near the wall is attracted. This second vortex which was much weaker at $R = 600$ has also been observed by R.-S. Lin (private communications, 1992) in his Navier-Stokes simulations of the crossflow vortex on a swept-wing. It should be stressed, however, that the actual flow is fully three-dimensional and varies along x . Hence, these particle traces do not depict the three-dimensional physical picture and have been used merely to facilitate the visualization of the crossflow vortices.

Contours in figure 10(c) show a second low velocity region near $z = 15$ and 30 ; a hot wire located at $y = 1$, for example, will show two velocity defects per wavelength when traversed in the spanwise direction. This is depicted in figure 13 which shows that the second defect, caused by the 2β mode and sometimes referred to as vortex doubling, is much smaller than that caused by the main vortex. In our simulations, the 2β mode is excited through nonlinear interaction and its amplitude remains smaller than the primary mode with wavenumber β as shown in figure 14 where the amplitude functions for the stationary vortex along with its harmonics and mean flow correction are plotted at $R = 600$. In a laboratory experiment, the 2β mode may be excited via surface imperfections and the relative amplitude of 1β and 2β modes may be different from the present case. The disturbance amplitude at $R = 600$ has reached to about 30 percent (when scaled with W_∞) with the maximum

meanflow correction of about 15 percent. In a laboratory experiment, this picture will be altered due to possible secondary instabilities and interaction with traveling modes.

Figure 15 shows the velocity profile along the crossflow vortex at 4 different locations across it for $R = 500$. The base flow given by the Hiemenz problem is also included. It can be seen that these profiles become strongly inflectional due to the motion within the crossflow vortex. Such profiles were also noted in the swept-wing experiments of Dagenhart *et al.* (1989) and Müller & Bippes (1988). These inflectional profiles as well as the inflectional profiles in z (figure 13) are subject to inviscid secondary instabilities which are most likely related to the high frequency disturbances observed by Kohama, Saric & Hoos (1991). We will investigate this aspect of the problem in a later section. Here, we first consider the interaction of traveling and stationary crossflow disturbances.

4.4 Stationary and traveling wave interaction

It was pointed out that the experiment of Müller & Bippes (1988) suggests an early nonlinear interaction between stationary and traveling waves. We now consider such interactions in the swept-Hiemenz flow. Our calculations are performed using $\beta = .4$ for both the stationary and traveling ($F = .75 \times 10^{-4}$) disturbances. The initial conditions were imposed at $R = 186$ and the amplitude of the stationary wave was the same as in § 4.3 above, i.e., .1 percent. For traveling waves, two different initial amplitudes were considered: .01 percent and .1 percent. Results for both the cases are discussed below.

Figure 16 gives the results of disturbance energy of various modes denoted as $(0,1)$, $(1,1)$, $(2,2)$, etc. Here, the first index refers to frequency ω and the second index to spanwise wavenumber β . Thus, mode $(2,2)$ is the harmonic with twice the frequency and twice the wavenumber of the traveling mode. For comparison, the case of stationary vortex only is also given. For the stationary vortex case, shown in figure 16(a), the energy cascades into 2β , 3β , 4β ... modes as earlier noted in the simulations by Malik (1986) and Meyer & Kleiser (1988). The energy in the mean flow correction mode is of the same order as the 2β mode. It is probable that the essential features of the nonlinear development of the stationary crossflow vortex can be captured by a model which considers 0 , β and 2β modes.

The interacting case with stationary vortex amplitude 10 times higher than traveling is shown in figure 16(b). This case is meant to simulate moderately low turbulence conditions where wall roughness will introduce dominant instability (i.e., stationary vortex) and the weak turbulence will introduce traveling disturbances with low amplitude. On the other hand, figure 15(a) can be thought of as the case with ultra-low turbulence with essentially no traveling modes induced. In contrast, figure 16(c) is the high-turbulence case where the initial amplitude of the traveling mode is equal to the stationary mode. Admittedly, these are all idealized cases, for in natural environment energy

input is into a broad band of frequencies and wavenumbers which we cannot attempt to tackle in the present framework.

Figure 16(b) shows that the energy in the stationary as well as the traveling mode saturates at about $R = 490$, the energy in the latter mode remains smaller except near the very end at about $R = 600$ where the two become the same. This is also where the energy in mode (1,-1) supersedes the two primary modes and becomes comparable to the mean flow correction mode. The mode (1,-1) is generated due to interaction between (1,1) and (0,2) mode and, apparently, the combination of the amplitudes is just about right to yield a resonance between the three modes as speculated in § 4.1 above.

The situation changes when the initial amplitude of the two waves become the same. The traveling mode has the higher energy all the way and it tends to suppress the growth of the stationary modes. Both the primary modes saturate earlier at about $R = 430$ as compared to 490 in figure 16(b). The higher modes gaining the dominant energy appear to be (2,2), (3,3), (4,4)... modes in this case. The suppression (also compare Figs. 17(a) and (c) below) of the stationary vortices by traveling modes is supported by the observation made in the DLR experiment.

The evolution of the maximum (in y) disturbance amplitude for the three cases is given in figure 17 on a natural log scale. Amplitudes of all the velocity components are given. Initially the spanwise velocity \hat{w} is higher than the chordwise velocity \hat{u} . Later the magnitude of the two switches as the inviscid streamline angle decreases (note that $\theta = 45^\circ$ when $R = 500$). The magnitude of the normal velocity \hat{v} is much lower than \hat{u} and \hat{w} for both waves at all R . From figure 17(a) for stationary vortices alone, it is clear that the nonlinear N factors ($\ln A/A_0$) at $R = 650$ are 7 and 5 for \hat{u} and \hat{w} . These are to be contrasted with the value of about 9 given by quasi-parallel linear calculations in figure 3.

The growth rates of the stationary and traveling waves for the above three cases, along with an additional case of traveling mode only (initial amplitude of 0.1 percent), are given in figure 18. For comparison, the growth rate from linear PSE calculations are also given. This plot more clearly shows the behavior of the two modes discussed with reference to figure 16. The growth rate of the stationary vortex (curve 2) begins to depart from linear theory at about $R = 420$. At this location the disturbance amplitude is only about 4 percent. At $R = 450$, the growth rate is lower than the linear theory result by about 9 percent, but it begins to decrease rapidly beyond that. The results are similar for the traveling mode alone (curve 2) with initial amplitude of .1 percent. Since the traveling mode amplifies more rapidly, it reaches saturation earlier and its growth rate begins to depart from the linear theory results at $R = 330$. For the wave interaction case with $A_i = .01$ percent, the growth rate of the two waves begins to depart from the linear theory result at about $R = 390$. At $R = 450$ the two growth rates differ from the linear results by about 18 percent. Subsequently, the two growth rates drop sharply and at $R = 500$, the stationary and traveling disturbance growth rates

are lower by about 70 and 76 percents with respect to their linear growth rates. Hence, the results indicate that even for the case with smaller initial traveling disturbance amplitude there is some interaction well before R of about 500. This interaction becomes stronger when the initial amplitudes of the two waves are the same ($A_s = A_t = .1$ percent). In this case the growth rates begin to depart from the linear theory results at $R = 330$ and by 410 the growth rates have dropped by 68 percent for the stationary vortex and by 39 percent for the traveling mode. A close examination of the results show that when $A_t = .1\%$, there is no direct effect of the stationary disturbance on the traveling wave (curves 3 and 5 collapse) but the growth of the stationary vortex is greatly suppressed due to the presence of higher amplitude traveling disturbance. It is clear that the two modes do interact depending upon the initial amplitude, as also inferred by Bippes (1991) from his experiments. The nonlinear growth rate behavior at large R indicates that the two primary modes reach a quasi-equilibrium state where the growth rate begins to oscillate around a small value.

In order to shed some more light on the stationary/traveling mode interaction, we consider the case with $A_s = .1$ percent, $A_t = .01$ percent, and plot \bar{u}_{rms} in the y - z plane at four different Reynolds numbers ($R = 431, 500$ and 600). Here \bar{u}_{rms} is defined as

$$u_{rms}(x, y, z) = \left[\frac{\omega}{2\pi} \int_0^{2\pi/\omega} u^2(x, y, z, t) dt - u_0^2 \right]^{1/2}.$$

The results are shown in figure 19 for the three locations. Due to nonlinearity and interaction with the stationary mode, traveling disturbances are modulated in the spanwise direction. An important observation is that the peak rms perturbation is near the wall at $y \approx 1$ with a second maximum (but with much lower amplitude) further away from the wall (see figure 19(b)). A comparison of Figs. 19(b) and 10(b), at $R = 500$, shows that the peak \bar{u}_{rms} occurs in the spanwise region where low-velocity fluid is pushed away from the wall. At higher Reynolds number ($R = 600$), there are two peaks in \bar{u}_{rms} near the wall, apparently associated with the emergence of 2β harmonic of the stationary mode. Michel, Arnal & Juillen (1985) also noted two maxima in the root mean-square value of the streamwise velocity within a spanwise wavelength in the ONERA/CERT swept-wing experiment. The magnitude of the maximum value was found to be up to about 20 percent of the resultant inviscid velocity. They also found that most of the turbulence energy is contained in the frequency range which is unstable according to the linear stability analysis.

Figure 20 is a plot of the stationary as well as rms velocity signal (u component) at $y = 1.048$. Modulation of the traveling disturbances due to the presence of stationary vortex is evident. The peak \bar{u}_{rms} is in the region where a velocity defect appears in the stationary signal and the minimum in \bar{u}_{rms} occurs where there is a velocity excess. However, there is a phase shift of about $\pi/4$ between the maximum in \bar{u}_{rms} and the minimum stationary velocity, as evident from results for $R = 500$. This

phase shift decreases at higher Reynolds numbers. Müller & Bippes (1988) reported experimental results qualitatively similar to those in figure 20.

We plot the variation of \tilde{u}_{rms} with Reynolds number at $y = 1.048$ in figure 21 which shows the maximum and minimum \tilde{u}_{rms} as well as \tilde{u}_{rms} along the path where stationary u velocity has a maximum and a minimum. The variation of the stationary u velocity with Reynolds number is also shown in the figure. The figure clearly shows that in high (stationary) velocity region the \tilde{u}_{rms} component gets saturated but it increases to higher amplitudes in the low (stationary) velocity region. At $R \approx 550$, the maximum \tilde{u}_{rms} reaches about 20 percent in the low-velocity region. Such high levels, although dependent upon the initial disturbance amplitude, are not unexpected in view of the experimental evidence provided by Michel, Arnal & Juillen (1985). Poll (1985) also observed a traveling disturbance with frequency close to the most amplified disturbance given by linear theory. He further noted that close to the surface the amplitude of these disturbances can exceed 20 percent of the local mean-flow velocity. However, the rms amplitudes measured by Dagenhart *et al.* (1989) are much lower which suggests that in their experiment the initial amplitude of traveling modes relative to the stationary mode was much lower than used here. Choudhari (1993) estimates that the initial amplitude of the traveling mode could be up to two orders of magnitude lower than the stationary modes for the receptivity mechanism considered in his study. This may possibly be the case in the experiment of Dagenhart *et al.*

4.5 Effect of nonlinear disturbances on skin-friction

Figure 22 gives the chordwise (C_{fu}) and spanwise (C_{fw}) skin-friction coefficients for all three cases. From figure 9 we know that skin-friction varies in the spanwise direction. However, figure 22 gives the spanwise averaged value, i.e., only the contribution from mean flow distortion is considered. Since \bar{w} is independent of R , laminar spanwise skin-friction remains constant. Similarly, since \bar{u} increases linearly with R , so does the chordwise skin-friction when scaled with W_∞^2 . At some location both C_{fu} and C_{fw} begin to depart from their respective laminar values. For case (a) and (b) of figure 16, this location is at about $R = 450$ and from thereon it rises significantly. The skin friction rise from stationary vortex alone is about 19 percent for C_{fu} and 58 percent for C_{fw} at $R = 600$. The skin-friction for case (b) is slightly higher in the beginning but later on it drops below case (a). Computations for case (a) were made using $N = 2, 9$ and 16 in (3.5). While there was considerable difference in the skin-friction distribution for $N = 2$ and 9, essentially no difference was found between the two higher resolution cases. For cases (b) and (c) $M = N = 9$ was used in (3.5).

In case (c), with higher initial amplitude of the traveling mode, skin friction begins to rise much earlier at about $R = 375$ as would be expected from the comparison of figure 16(b) and (c) which shows that the mean flow distortion is higher in the latter case. Hence, a stronger interaction of the traveling and stationary modes leads to higher skin-friction coefficient. Our results indicate that the

angle between wall shear and inviscid free stream decreases as the disturbed flow enters highly nonlinear stage in the three-dimensional boundary layer.

5. High Frequency Secondary Instability

A hot-wire placed in a three-dimensional boundary layer, subject to crossflow instability, sees two types of unsteady disturbances. First, it captures an unsteady signal with a peak at a frequency f_1 which coincides with the most amplified frequency given by the linear stability theory. In the present case, e.g., $f_1 \approx 1.2 \times 10^{-4}$ at $R = 300$ (see, figure 5). The dimensional value of this frequency depends upon the flow parameters (unit Reynolds number, sweep, etc.). Poll (1985), for his swept cylinder experiment, found f_1 to be 1500 Hz for the chord Reynolds number of 1.2×10^6 and sweep angle of 63° . In Kohama, Saric & Hoos (1991), f_1 was close to 180 Hz and in Michel, Arnal & Juillen (1985) $f_1 < 200$. In these experiments, the hot-wire also captures a second frequency f_2 which is an order of magnitude larger than f_1 . For example, f_2 was 17500 Hz, 3500 Hz and 1000 Hz in the experiments of Poll (1985), Kohama, Saric & Hoos (1991) and Michel, Arnal & Juillen (1985), respectively. In this section, we investigate this high frequency instability in the present three-dimensional boundary layer. The problem is modeled here as the secondary instability of the new mean flow which is set up by the presence of a large-amplitude stationary crossflow vortex.

We perform secondary instability analysis locally, i.e., at a fixed Reynolds number and perform temporal stability analysis. In order to perform this analysis, we rotate the x - z coordinates to a new system, x_2, z_2 so that the x_2 coordinate aligns with the crossflow vortex. At a streamwise location designated by the Reynolds number R , we ignore the curvature of the vortex and use the quasi-parallel approximation (we will provide a posteriori justification for these assumptions later) which allows us to consider a harmonic disturbance of the type

$$\phi(x_2, y_2, z_2, t) = \phi_2(y_2, z_2, t)e^{i(\alpha_2 x_2 - \omega_2 t)}, \quad (5.1)$$

where α_2 and ω_2 are the wavenumber and frequency of the secondary disturbance and $y_2 = y$. Here, since we use temporal stability concept, α_2 is real and ω_2 is complex. If $\omega_{2i} > 0$ ($\omega_{2i} = \text{Imag}(\omega_2)$), then the secondary instability is present. Temporal stability approach has earlier been used by Herbert (1983) for secondary instability of TS waves and by Hall and Horseman (1991) for secondary instability of Görtler vortices. This approach can, at least, provide a qualitative picture of the secondary instability phenomenon.

We superimpose (5.1) on the meanflow computed in § 4.3 above, i.e., the meanflow constitutes the three-dimensional boundary layer as modulated by the presence of a nonlinear stationary crossflow vortex with initial amplitude of .1 percent. This meanflow, when represented in (x_2, y_2, z_2) coordinate system, is a strong function of y_2 and z_2 but a weak function of x_2 . Substituting the

meanflow and the disturbance wave (5.1) in incompressible Navier-Stokes equations, we obtain the following linearized equations

$$\left[i\alpha_2 U_2 + \alpha_2^2 / R + \frac{\partial U_2}{\partial x_2} \right] u_2 + \frac{\partial U_2}{\partial y_2} v_2 + \frac{\partial U_2}{\partial z_2} w_2 + i\alpha_2 p_2 + V_2 \frac{\partial u_2}{\partial y_2} + W_2 \frac{\partial u_2}{\partial z_2} - \frac{1}{R} \left[\frac{\partial^2 u_2}{\partial y_2^2} + \frac{\partial^2 u_2}{\partial z_2^2} \right] = i\omega_2 u_2 \quad (5.2)$$

$$\frac{\partial V_2}{\partial x_2} u_2 + \left[i\alpha_2 U_2 + \alpha_2^2 / R + \frac{\partial V_2}{\partial y_2} \right] v_2 + \frac{\partial V_2}{\partial z_2} w_2 + V_2 \frac{\partial v_2}{\partial y_2} + W_2 \frac{\partial v_2}{\partial z_2} + \frac{\partial p_2}{\partial y_2} - \frac{1}{R} \left[\frac{\partial^2 v_2}{\partial y_2^2} + \frac{\partial^2 v_2}{\partial z_2^2} \right] = i\omega_2 v_2 \quad (5.3)$$

$$\frac{\partial W_2}{\partial x_2} u_2 + \frac{\partial W_2}{\partial y_2} v_2 + \left[i\alpha_2 U_2 + \alpha_2^2 / R + \frac{\partial W_2}{\partial z_2} \right] w_2 + V_2 \frac{\partial w_2}{\partial y_2} + W_2 \frac{\partial w_2}{\partial z_2} + \frac{\partial p_2}{\partial z_2} - \frac{1}{R} \left[\frac{\partial^2 w_2}{\partial y_2^2} + \frac{\partial^2 w_2}{\partial z_2^2} \right] = i\omega_2 w_2 \quad (5.4)$$

$$i\alpha_2 u_2 + \frac{\partial v_2}{\partial y_2} + \frac{\partial w_2}{\partial z_2} = 0 \quad (5.5)$$

where U_2, V_2, W_2 are the mean velocity components in x_2, y_2, z_2 directions, respectively, and u_2, v_2, w_2 are the corresponding disturbance velocity components and p_2 is the pressure. In (5.2)–(5.4) terms $\partial U_2 / \partial x_2, \partial V_2 / \partial x_2, \partial W_2 / \partial x_2$ are small and can be neglected as numerical experiments indicate that they do not appreciably change the eigenvalue. However, $\partial V_2 / \partial y_2$ is of the same order as $\partial W_2 / \partial z_2$ and thus V_2 must not be set to zero. Dropping V_2 increases the growth rate by about 50 percent. Equations (5.2–5.5) are partial differential equations which are subject to homogeneous conditions at the wall and free-stream, i.e.,

$$u_2 = v_2 = w_2 = 0, \quad y_2 = 0 \quad (5.6a)$$

$$u_2 \rightarrow 0, \quad v_2 \rightarrow 0, \quad w_2 \rightarrow 0 \quad \text{as} \quad y_2 \rightarrow \infty \quad (5.6b)$$

The computational domain in z_2 direction covers one wavelength of the stationary vortex and periodic boundary conditions are imposed in the z_2 direction, i.e.,

$$u_2(z_2) = u_2(z_2 + \lambda_z) \quad (5.7a)$$

$$v_2(z_2) = v_2(z_2 + \lambda_z) \quad (5.7b)$$

$$w_2(z_2) = w_2(z_2 + \lambda_z), \quad (5.7c)$$

where $\lambda_z = 2\pi / (\alpha_s^2 + \beta_s^2)^{1/2}$, α_s and β_s being the x and z wavenumbers of the stationary vortex.

Equations (5.2–5.5) along with the boundary conditions (5.6–5.7) constitute an eigenvalue problem which we solve by using a Chebyshev collocation method in the y_2 direction and a Fourier collocation method in the z_2 direction. The physical domain $y_2 \in [0, y_{2\max}]$ is mapped on to a computational domain $\eta \in [-1, 1]$ such that the grid points are clustered near the wall and $y_2 = y_{2i}$, where y_{2i} is the location where the secondary structure is concentrated. Since we do not stagger the mesh in

y_2 direction, two additional boundary conditions are required which we prescribe by evaluating the normal momentum equation at $y_2 = 0$ and $y_{2_{\max}}$.

The eigenvalue problem can be represented in the form

$$\mathbf{A}\phi = \omega_2 \mathbf{B}\phi \quad (5.8)$$

where \mathbf{B} is a diagonal matrix and \mathbf{A} is a square matrix of size $(4N_y - 6)N_z$ where N_y and N_z are the number of collocation points in y_2 and z_2 directions, respectively. The above eigenvalue problem (5.8) is solved by the QR method which yields all the eigenvalues of the discretized system. We test the accuracy of these eigenvalues by using inverse Rayleigh iteration method. Among the computed eigenvalues, only a few have $\omega_{2i} > 0$. Here, we discuss only one of these eigenvalues.

Computations were first performed at $R = 450$ where the stationary crossflow disturbances had gained an amplitude of about 8 percent based upon the local inviscid velocity (see, figure 17(a)). No secondary instability was found, i.e., all $\omega_{2i} < 0$. The analysis was then repeated at $R = 500$ where the maximum \hat{u} amplitude is about 17 percent and the stationary vortex is on its way to saturation (compare with figure 18). At this location the secondary instability is found but the growth rate is about the same as that of the nonlinear crossflow vortex. Finally, calculations were performed at $R = 550$ where figure 18 shows that the stationary vortex has a growth rate which is close to zero. The local maximum amplitude of the stationary vortex is about 22 percent. Secondary instability results for this Reynolds number are discussed next.

The frequency (ω_{2r}) of the secondary instability and temporal growth rate (ω_{2i}) are plotted in figure 23. The peak growth rate of $\omega_{2i} \approx .02$ occurs at α_2 of about .6. At this location ω_{2r} is about .75 which amounts to an F_2 of 1.5×10^{-3} . We noted earlier that the most amplified traveling crossflow disturbance has a frequency of about $F_1 \approx 1.2 \times 10^{-4}$; hence, F_2 is an order of magnitude higher than F_1 which is in agreement with the experiments mentioned above. The wavenumber of the stationary disturbance along z_2 coordinate is about .5. Given that α_2 is .6, the angle of the secondary structure is about 50° with respect to the crossflow vortex. The secondary instability convects along the stationary vortex with the phase velocity of about $1.25 W_\infty$. The relatively high amplitude of the stationary vortex required for secondary instability is in agreement with the results of Balachandar, Streett & Malik (1992).

The above calculations were made with $N_y = 41$ and $N_z = 8$. Since 8 collocation points in the spanwise direction may be too few, we repeated some of the calculations with $N_z = 16$ and $N_y = 51$. These results are also given in figure 23. We note that although there is some movement in the eigenvalues, the results given in the figure with the lower resolution are qualitatively correct, at least at high α_2 . At lower values of the wavenumber α_2 , there appears to be an intricate mode structure which for its investigation would require the development of more efficient means of computing eigenvalues of very large matrices so that these calculations can be readily performed.

The quasi-parallel approximation used in the above analysis can be justified since our results show that, in the rotated coordinate system, variations of U_2, V_2, W_2 along x_2 is much smaller than the variation in y_2, z_2 and the x_2 -wavelength of the secondary instability is only about 3 times the boundary-layer thickness. In the nondimensional units, this wavelength for the most amplified secondary wave is about 10. The secondary instability analysis shown in Fig. 23 is performed at $R = 550$. It is clear from Fig. 9 that the curvature of the vortex in the range of $R = 550 \pm 5$ can be ignored.

The structure of the secondary instability is presented in figure 24 where the $|\mu_2|$ eigenfunction is plotted along with the U_2 component of the meanflow in $y_2 - z_2$ plane at $R = 550$. It is clear that this high-frequency instability resides on top of the stationary vortex with the maximum in $|\mu_2|$ located near $y_2 \approx 2.8$. In contrast, the lower frequency traveling crossflow disturbance is concentrated near the wall at $y_2 \approx 1$ (see figure 19). The high frequency instability is inviscid in nature and it can be captured by dropping viscous terms in (5.2-5.4); however, since the basic flow is three-dimensional and varies with y_2 and z_2 it is not possible to reduce the problem to a single partial differential equation. However, numerical experiments suggest that some qualitative features of the instability can be captured by considering just the U_2 component of the mean flow in which case a single partial differential equation can be used resulting in substantial savings in computer time.

The top view of the flow field that results by superimposing the secondary eigenstructure (with an amplitude of 5%) on the meanflow (U_2, V_2, W_2) is depicted in figure 25 where the x_2 -velocity component is plotted at $y_2 = 2.82$. Two periods in both x_2 and z_2 directions are shown. The dark patches in the picture correspond to the corotating structures which move in the x_2 direction. A hot wire placed near the boundary-layer edge will detect this high-frequency disturbance but if the hot-wire is located in the region between $z_2 = 5$ and 10, for example, this instability will not be captured. Therefore, extreme care is needed in order to detect this secondary structure in an experiment.

6. Conclusions

We have investigated crossflow instability in a model three-dimensional boundary layer which has an exact solution to the incompressible Navier-Stokes equations. This consists of the swept-Hiemenz flow which forms near an attachment-line. This flow is subject to Tollmien-Schlichting instability for small x , where x is the chordwise distance, provided the spanwise Reynolds number $\bar{R} > 583.1$. However, this boundary-layer becomes unstable to crossflow instability for $x \gg 1$ even for $\bar{R} < 583.1$. Here, we have considered $\bar{R} = 250$ and 500 for the linear stability and $\bar{R} = 500$ for the nonlinear case. Both the linear and nonlinear stability as well as the wave-interaction in this three-dimensional boundary layer is studied using parabolized stability equations (PSE). We also study

secondary instability in this boundary layer. We find that the various features of the swept-wing boundary-layer transition are captured in the study of this model boundary layer.

Our linear results show that nonparallel effects are destabilizing for crossflow disturbances. However, the magnitude of the effect depends upon \bar{R} (more destabilization at lower \bar{R}). Growth rate of stationary crossflow vortices computed from linear PSE are in agreement with the results obtained from Navier-Stokes simulation.

Nonlinear development of stationary crossflow vortex is also investigated for an initial amplitude of 0.1 percent. The computed wall vorticity distribution shows the familiar streamwise streaks, in agreement with the surface oil-flow visualizations in swept-wing experiments. Other features of the stationary vortex development observed in the experiments (half-mushroom structure, highly inflected velocity profiles, vortex doubling, etc.) are also captured in our nonlinear PSE computations.

Nonlinear interaction of stationary and traveling crossflow modes is also studied. When the initial amplitude of stationary vortex is large as compared to the traveling mode, the stationary vortex dominates most of the downstream development. Eventually, however, the traveling mode becomes of the same order as stationary mode. Interaction of the traveling mode with the harmonic of the stationary mode gives rise to another traveling mode with same frequency but negative spanwise wavenumber. Apparently, a triad resonance is set up at this stage. The situation changes when the initial amplitude of the traveling and stationary modes are the same. Owing to its higher growth rate, traveling mode dominates most of the downstream development and the growth of the stationary mode is suppressed. In this case, energy cascades into (2,2), (3,3) etc., modes which are harmonics of the primary (1,1) traveling mode.

Growth rates of the stationary and traveling modes begin to depart from their linear values when the disturbance amplitude reaches about 4 percent. As the amplitude increases, the primary modes reach quasi-equilibrium states. Large mean flow distortion caused by the nonlinear disturbances yields a skin-friction value which is significantly above the laminar value.

Finally, we use the two-dimensional eigenvalue approach to perform a secondary instability analysis of the three-dimensional boundary-layer flow modulated by the presence of a nonlinear stationary crossflow vortex. We find that this meanflow is subject to an instability whose frequency is an order of magnitude higher than the frequency of the most amplified traveling mode given by linear stability analysis of the boundary-layer profiles. A similar high frequency disturbance was also observed in the experiments of Poll (1985) and Kohama, Saric & Hoos (1991).

REFERENCES

- Arnal, D. & Juillen, J. C. 1987 *AIAA Paper* 87-1335.
Balachandar, S., Streett, C. L. & Malik, M. R. 1992 *J. Fluid Mech.* **242**, 323.

- Bertolotti, F. P., Herbert, Th. & Spalart, P. R. 1992 *J. Fluid Mech.* **242**, 441.
- Bippes, H. 1991 Royal Aeronautical Soc. Conf. on Boundary Layer Transition & Control, Cambridge, UK.
- Chang, C.-L., Malik, M. R., Erlebacher, G. & Hussaini, M. Y. 1991 *AIAA Paper* 91-1636.
- Choudhari, M. M. 1993 *TCFD* **5**, 487.
- Choudhari, M. M. & Streett, C. 1990 *AIAA Paper* 90-5258.
- Dagenhart, J. R., Saric, W. S., Mousseaux, M. C. & Stack, J. P. 1989 *AIAA Paper* 89-1892.
- Fischer, T. M. & Dallmann, U. 1991 *Phys. Fluids A* **3**, 2378.
- Gray, W. E. 1952 Royal Aeronautical Establishment Tech. Memo. (Aero) 256.
- Gregory, N., Stuart, J. T. & Walker, W. S. 1955 *Phil. Trans, Roy. Soc. A* **248**, 155.
- Hall, P., Malik, M. R. & Poll, D. I. A. 1984 *Proc. Roy. Soc. Lond. A* **395**, 229.
- Herbert, Th. 1991 *AIAA Paper* 91-0737.
- Joslin, R. D., Streett, C. L. & Chang, C.-L. 1992 *NASA TP*-3205.
- Kohama, Y. 1984 *Acta Mechanica* **50**, 193.
- Kohama, Y. 1987 *AIAA Paper* 87-1340.
- Kohama, Y., Saric, W. S. & Hoos, J. A. 1991 *Proc. Royal Aeronautical Soc. Conf. on Boundary Layer Transition & Control*, p. 4.1.
- Mack, L. M. 1985 *AIAA Paper* 85-0490.
- Malik, M. R. 1986 *10th International Conf. on Numerical Methods in Fluid Dynamics* (ed. F. G. Zhuang & Y. L. Zhu), p. 455, Springer-Verlag.
- Malik, M. R., Chuang, S. & Hussaini, M. Y. 1982 *ZAMP* **33**, 189.
- Malik, M. R. & Li, F. 1992 *SAE Paper* 921991.
- Malik, M. R. & Li, F. 1993 *AIAA Paper* 93-0077.
- Meyer, F. & Kleiser, L. 1988 *AGARD Conference Proceedings No. 438*, p. 16-1.
- Michel, Arnal & Juillen, R., Arnal, D. & Juillen, J. C. 1985 *Laminar Turbulent Transition* (ed. V. V. Kozlov), p. 553, Springer-Verlag.
- Müller, B. & Bippes, H. 1988 *AGARD Conference Proceedings No. 438*, p. 13-1.
- Müller, B. 1989 *Laminar-Turbulent Transition* (eds. D. Arnal & R. Michel, Arnal & Juillen), p. 489, Springer-Verlag.
- Peerhossaini, H. & Wesfreid, J. E. 1988 *Int. J. Heat Fluid Flow* **9**, p. 12.
- Poll, D. I. A. 1985 *J. Fluid Mech.* **150**, p. 329.
- Reed, H. L. 1987 *Phys. Fluids* **30**, 3419.
- Saric, W. S., Dagenhart, J. R. & Mousseux, M. C. 1989 *Numerical & Physical Aspects of Aerodynamic Flows* **4**, (ed. T. Cebeci) Springer-Verlag.

Saric, W. S. & Yeates, L. G. 1984 *Proc. IUTAM Symp. on Laminar-Turbulent Transition* Novosibirsk, USSR, Springer-Verlag.

Spalart, P. R. 1988 *AGARD Conf. Proc. No. 438*, p. 5-1.

Spalart, P. R. 1989 *Laminar-Turbulent Transition* (eds. D. Arnal & R. Michel, Arnal & Juillen), p. 622, Springer-Verlag.

Streett, C. 1993, private communications.

Swearingen, J. D. & Blackwelder, R. F. 1987 *J. Fluid Mech.* **182**, 255.

Wilson, S. D. R. & Gladwell, I. 1978 *J. Fluid Mech.* **84**, 517.

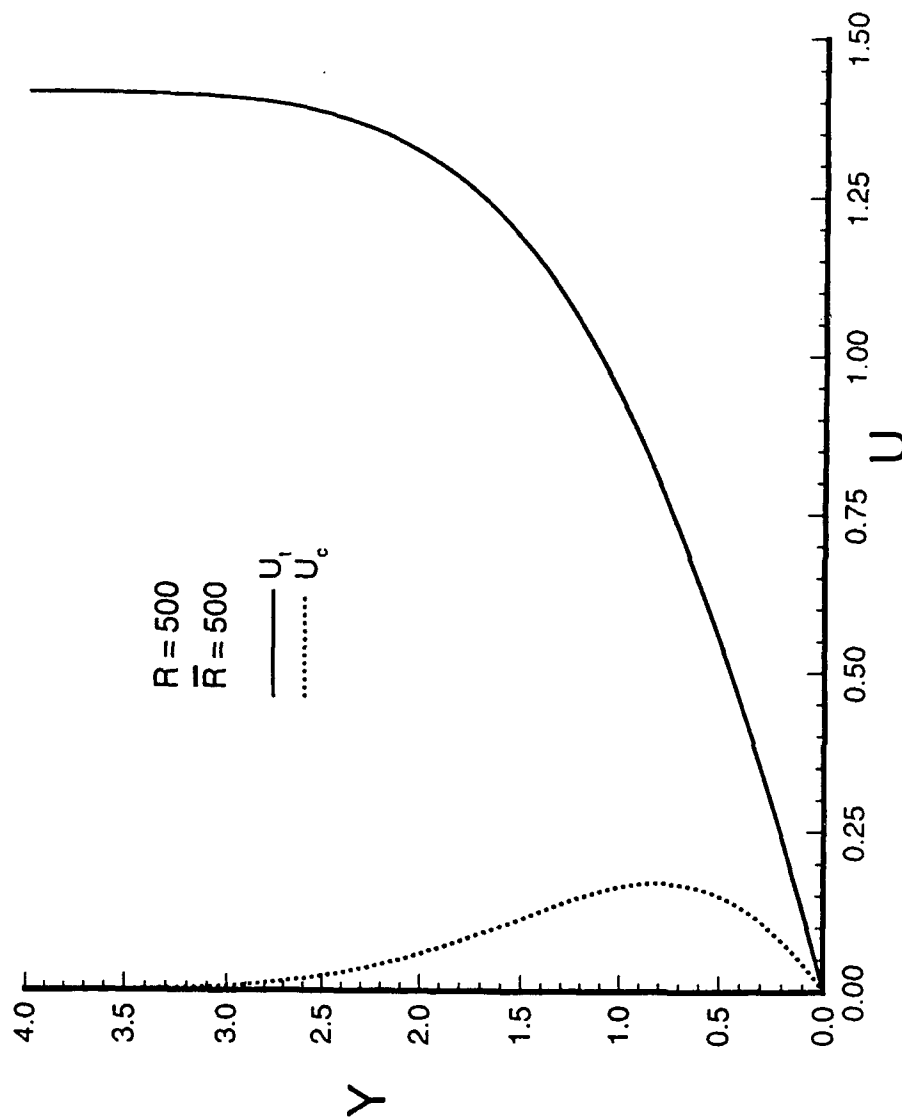


Figure 1. Streamwise (U_t) and crossflow (U_c) velocity profiles in the swept Hiemenz flow.

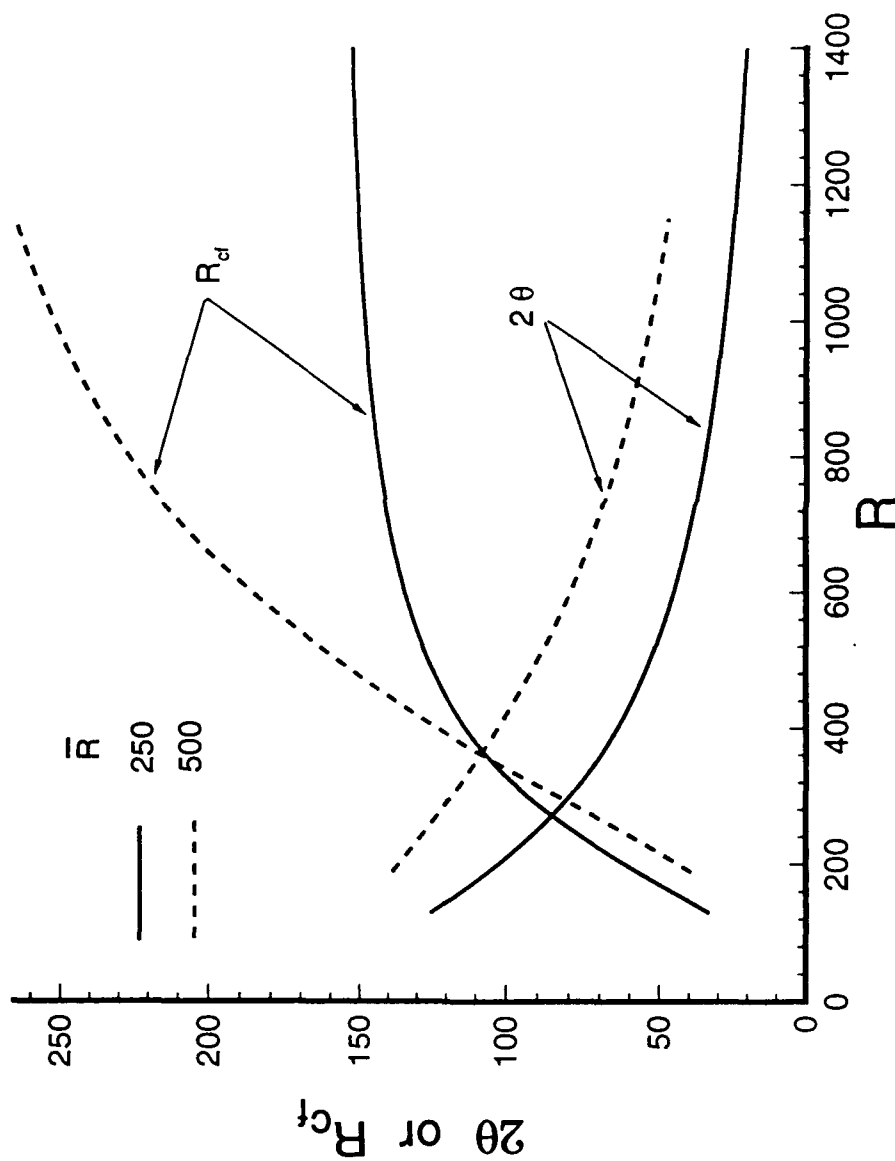


Figure 2. Variation of inviscid streamline angle (θ) and crossflow Reynolds number (R_{cf}).

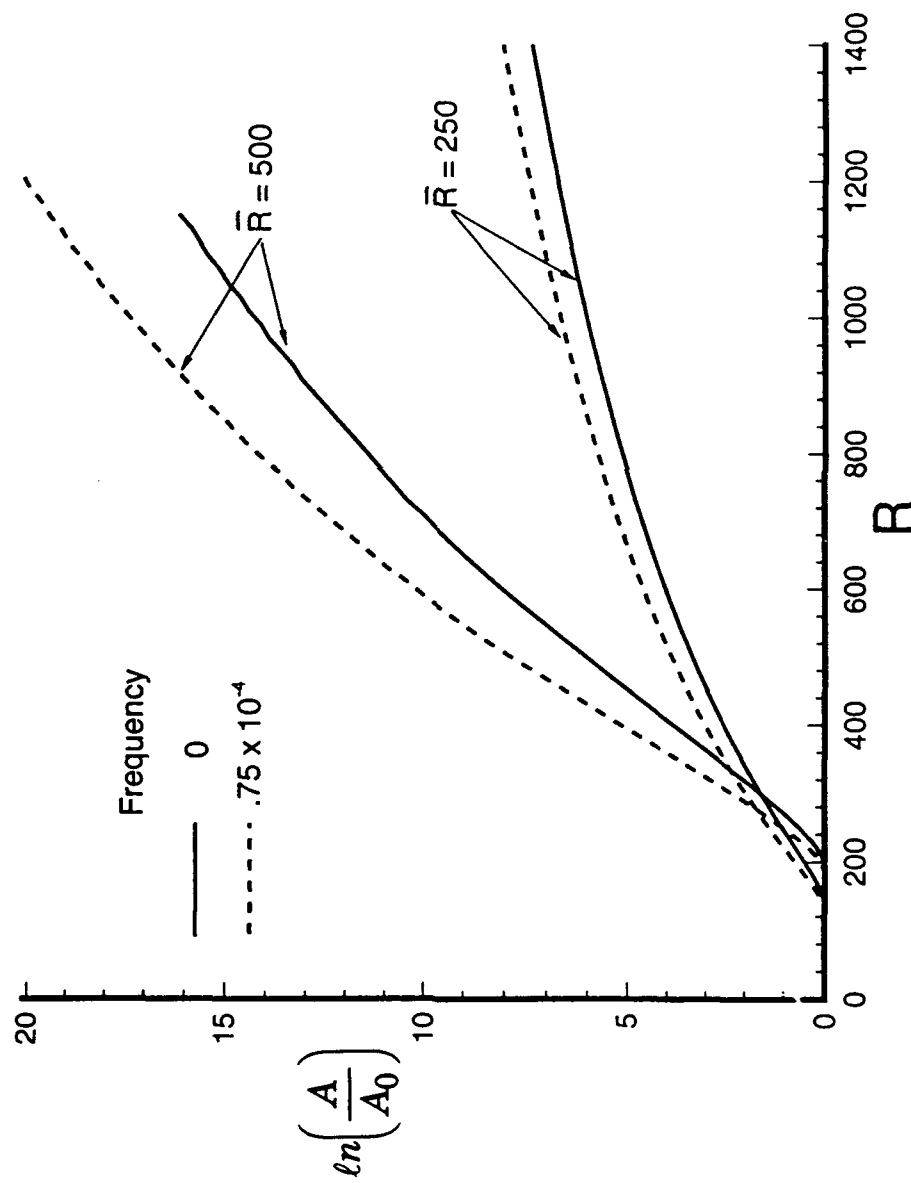


Figure 3. Integrated growth for fixed spanwise wavenumber $\beta = .4$.

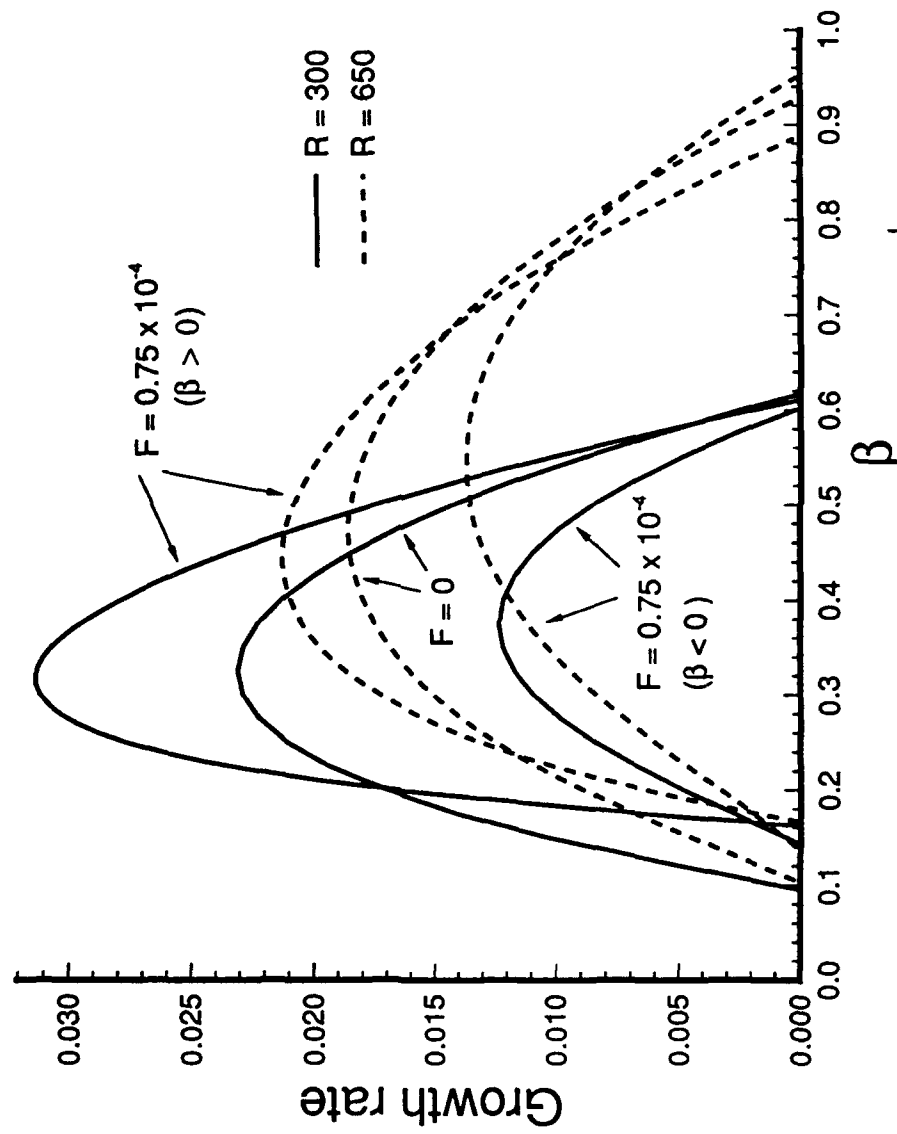


Figure 4. Quasi-parallel growth rate for positive and negative β at $\bar{R} = 500$.

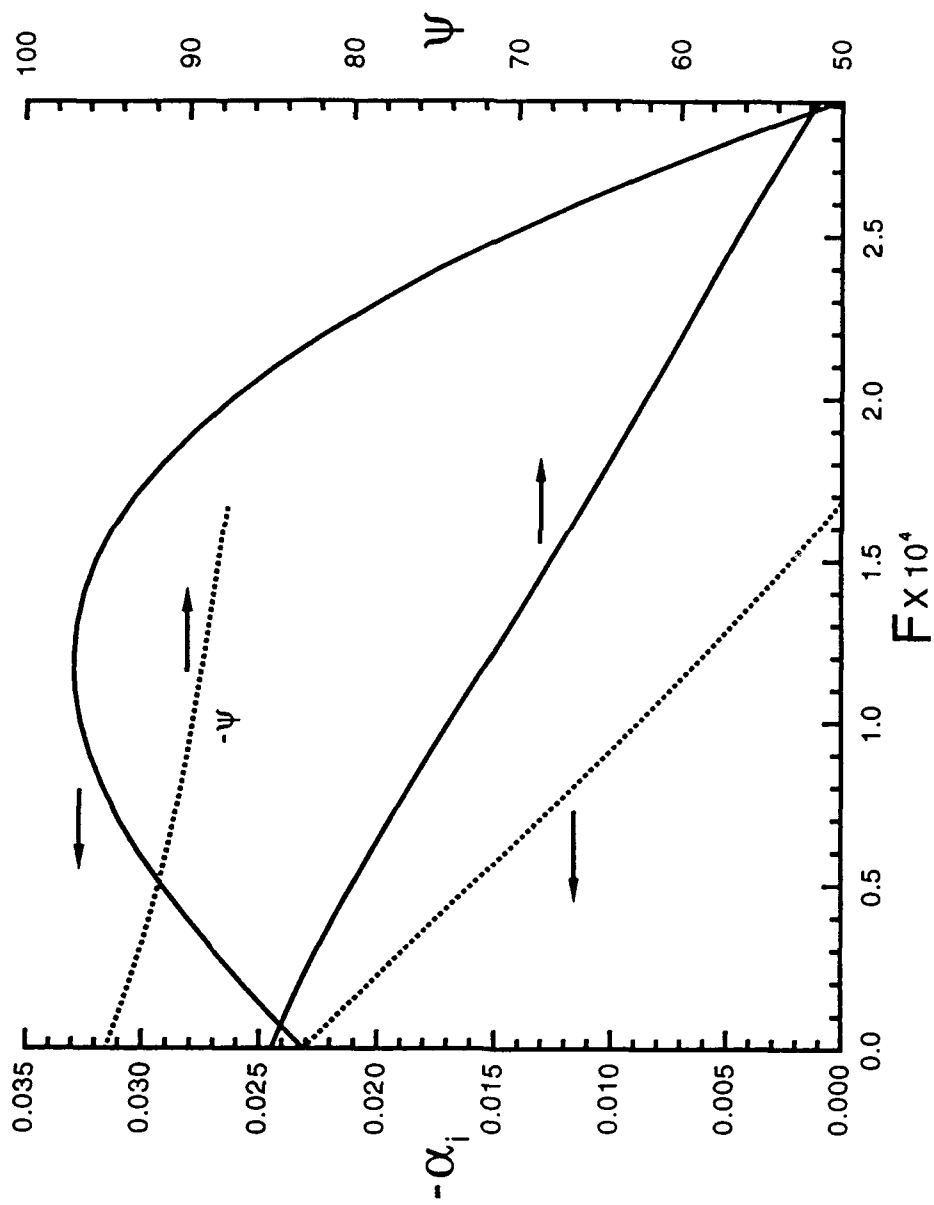
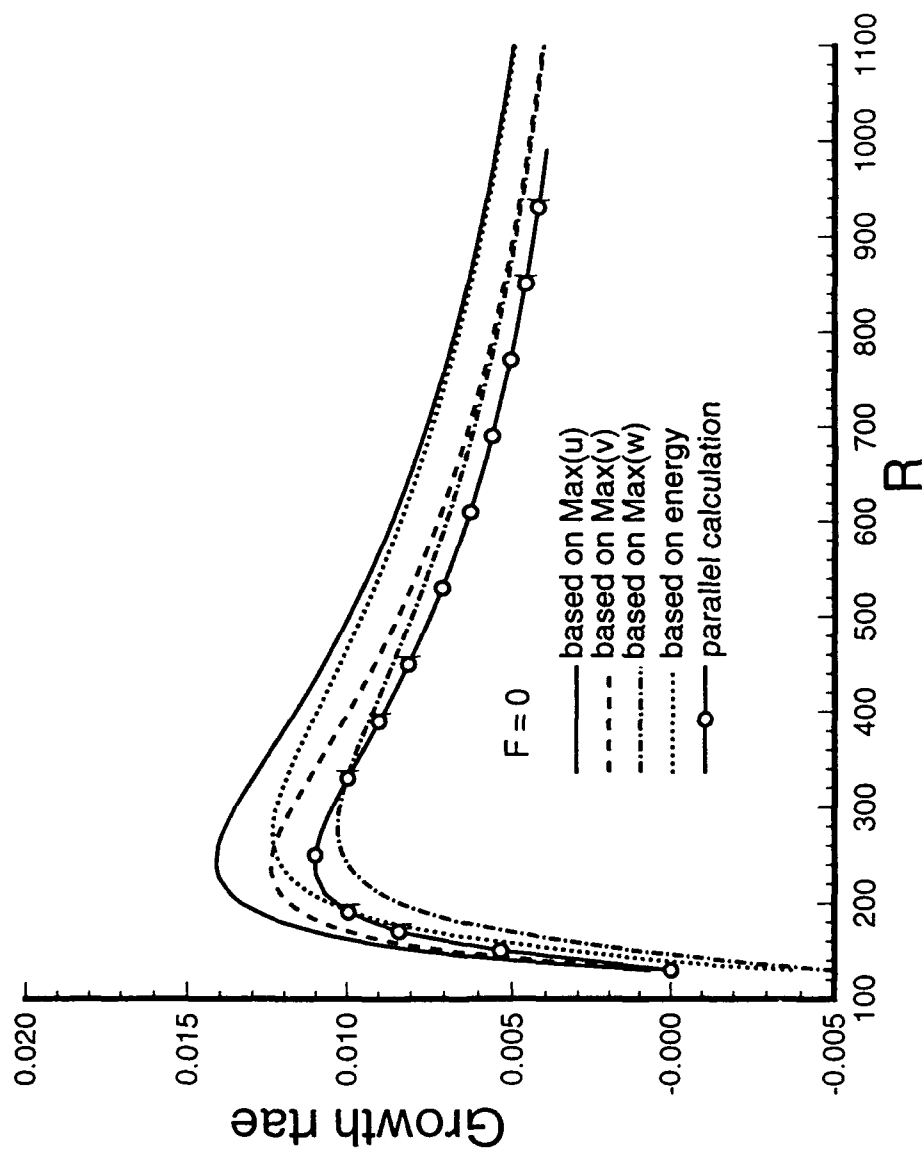
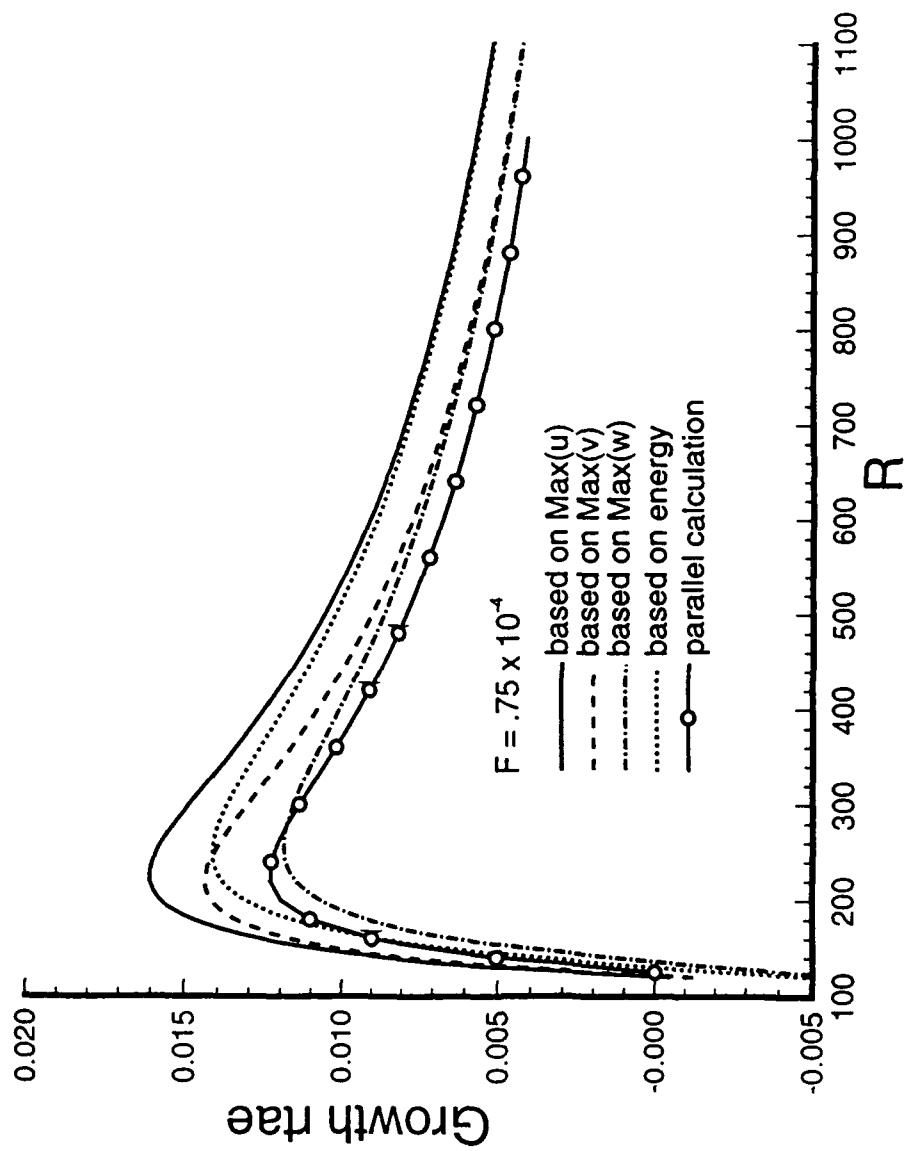


Figure 5. Growth rates (most amplified) and orientation (ψ) of the two families of unstable modes at $\bar{R} = 500$, $R = 300$.



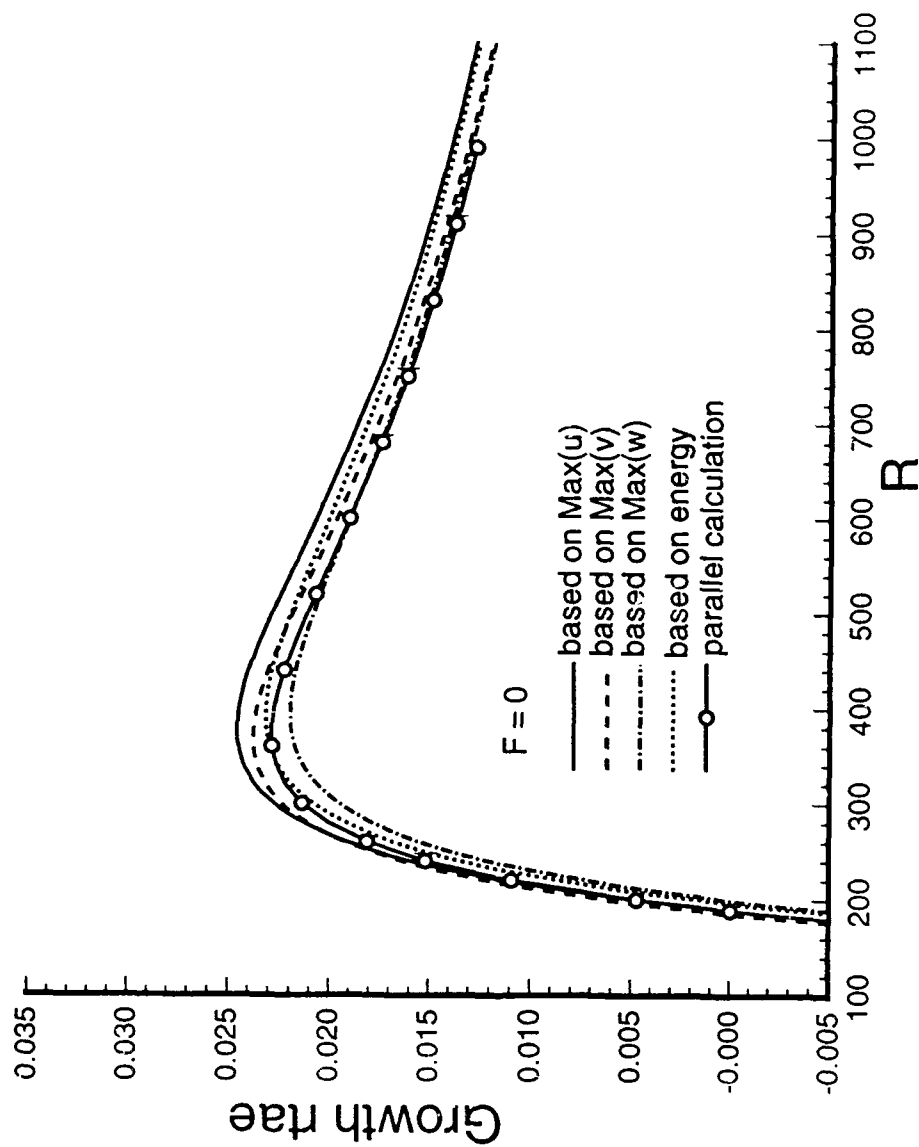
(a) stationary vortex

Figure 6. Disturbance growth rate for $\beta = .4$ and $\bar{R} = 250$.



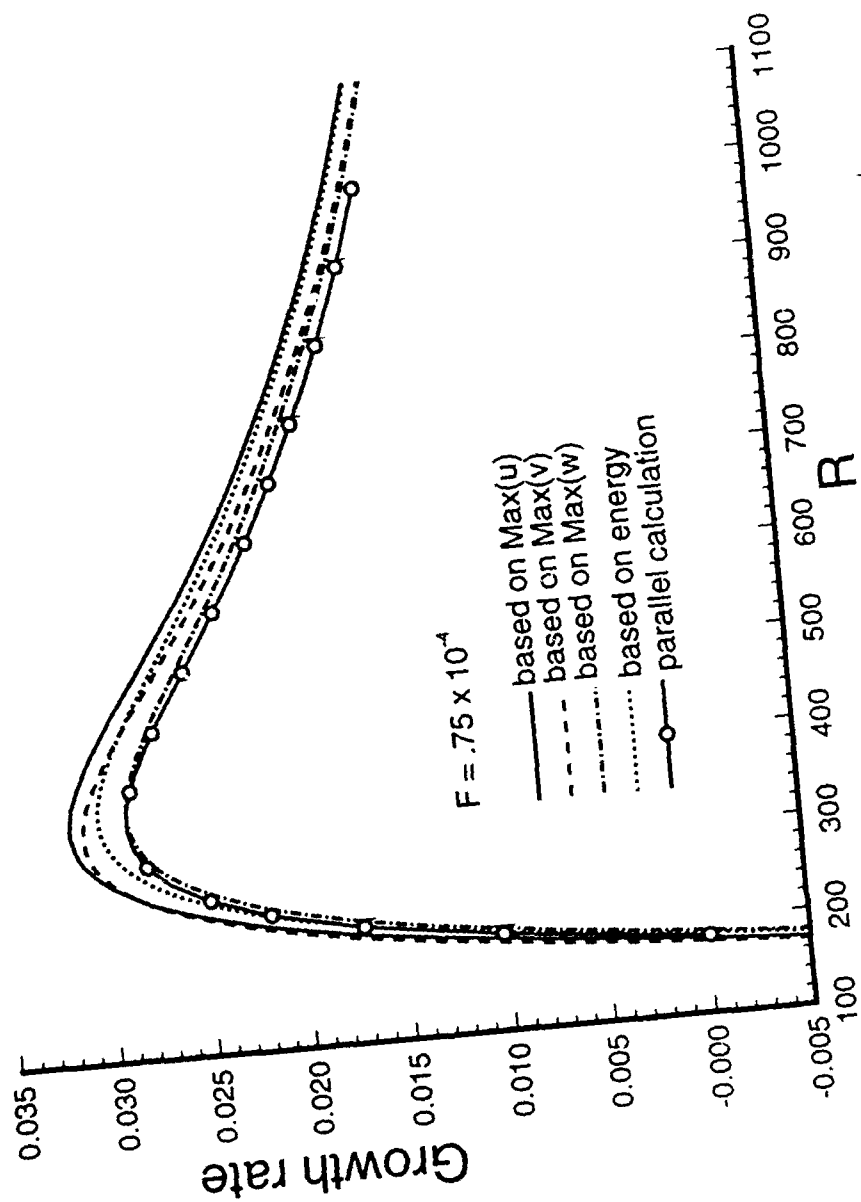
(b) traveling disturbance with frequency $F = .75 \times 10^{-4}$

Figure 6. Concluded.



(a) stationary vortex

Figure 7. Disturbance growth rate for $\beta = .4$ and $\bar{R} = 500$.



(b) traveling disturbance, $F = .75 \times 10^{-4}$
Figure 7. Concluded.

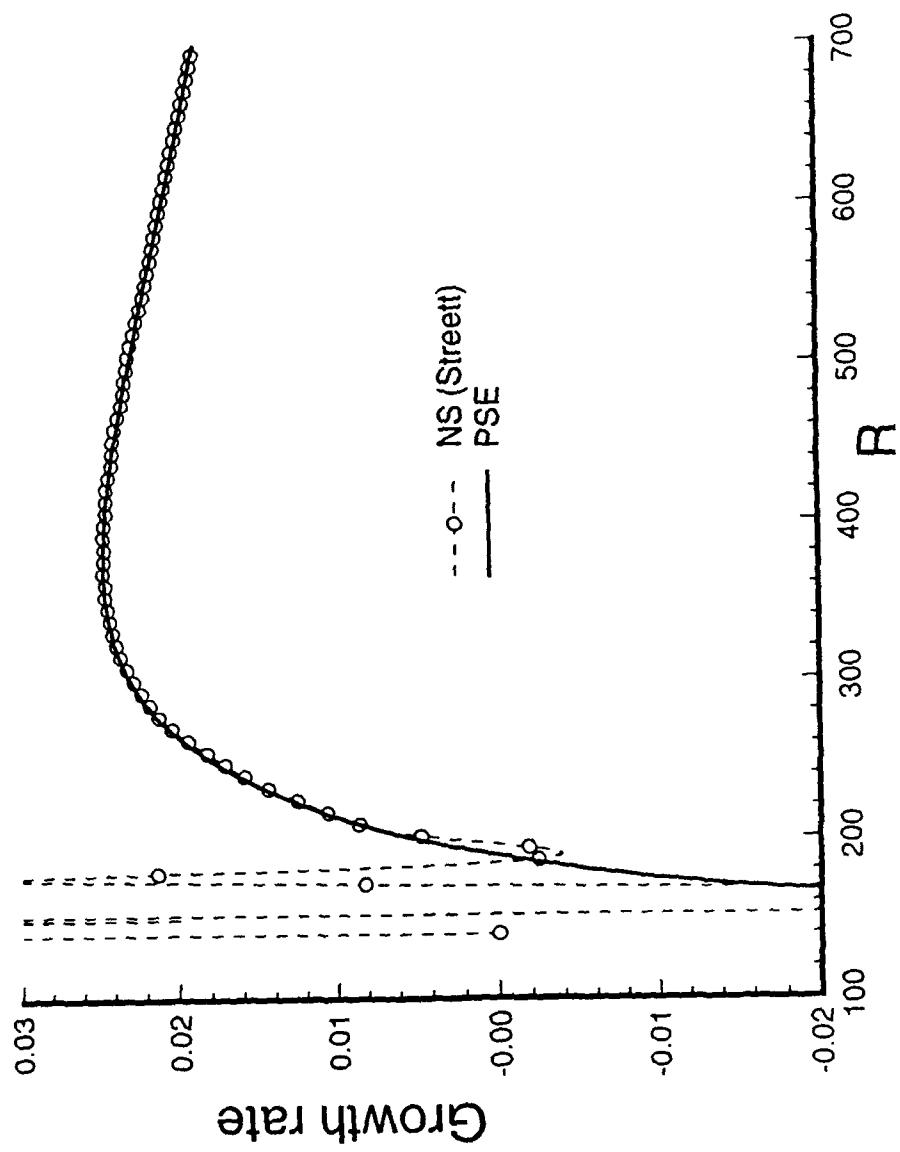


Figure 8. Comparison of linear PSE and Navier-Stokes simulations of Streett (1993) for stationary vortex. ($\bar{R} = 500$, $\beta = .4$, growth rate based on u).

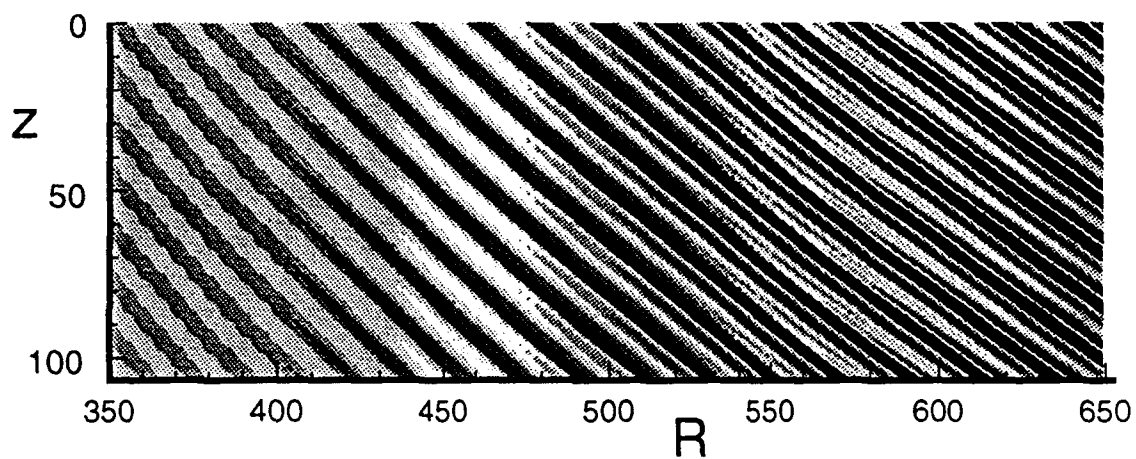
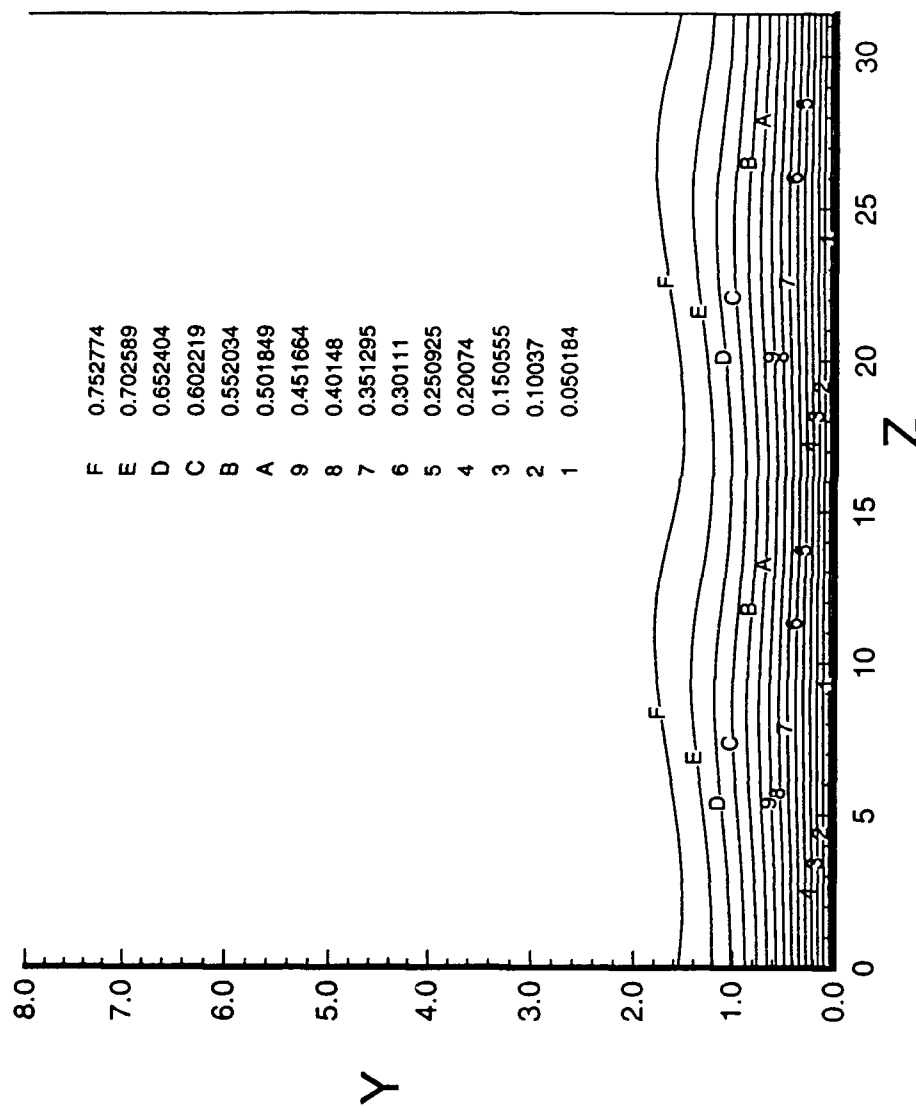
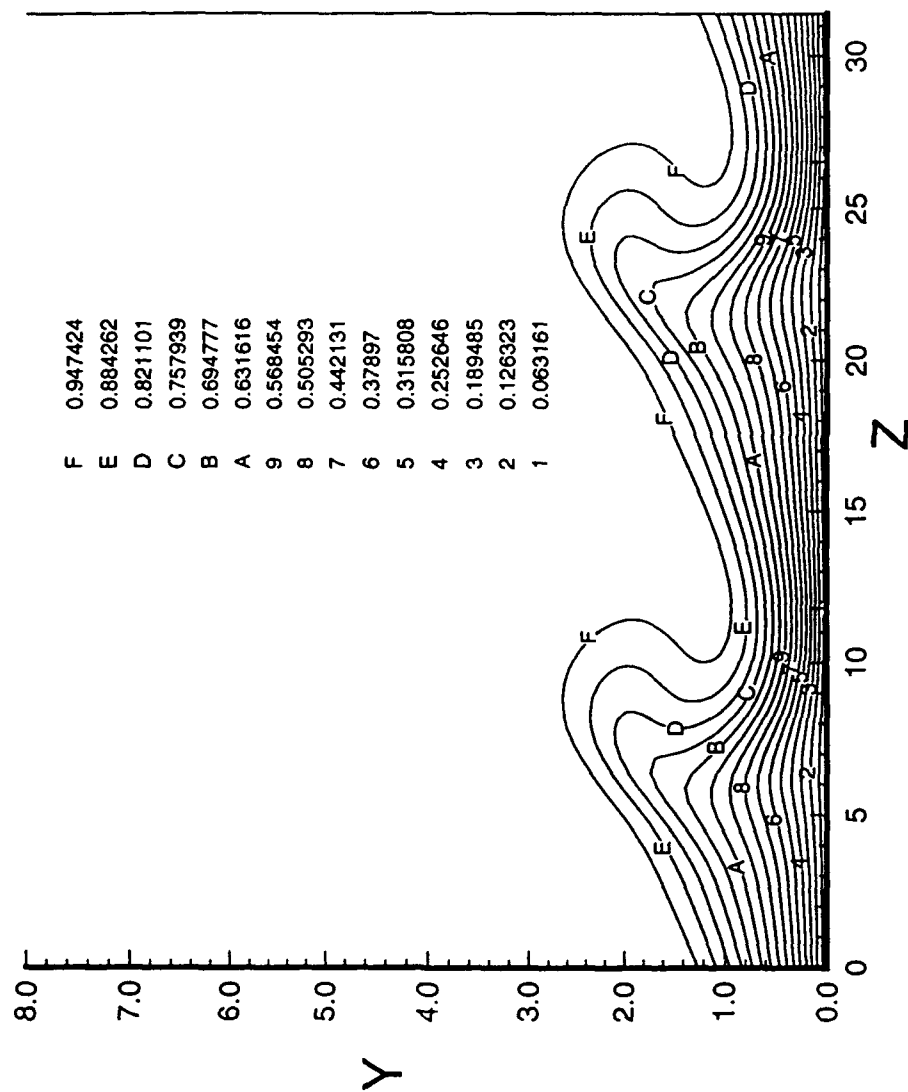


Figure 9. Computed wall vorticity distribution in the presence of nonlinear stationary vortices, $\beta = .4$, $\bar{R} = 500$.



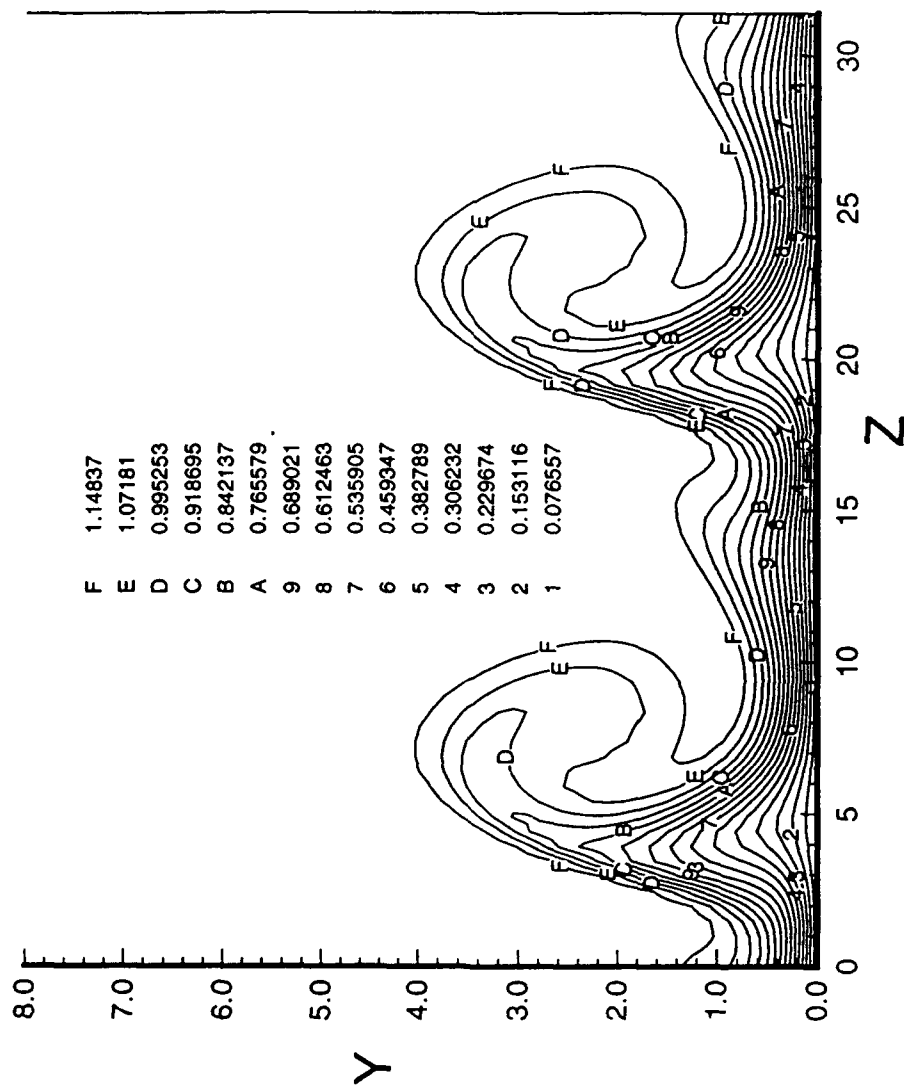
(a) $R = 400$

Figure 10. Variation of u velocity (for $\bar{R} = 500$) in y - z plane in the presence of stationary crossflow vortex. Two spanwise wavelengths are shown. The view is from upstream.



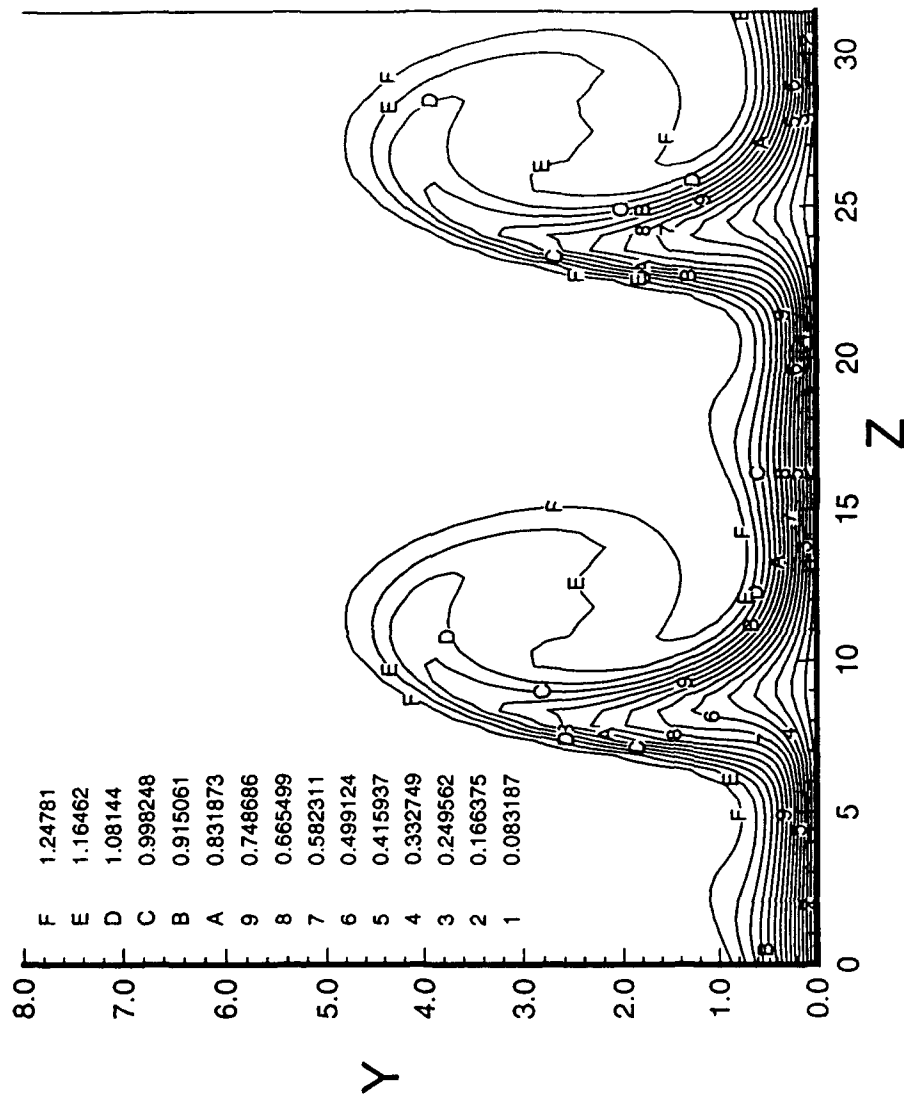
(b) $R = 500$

Figure 10. Continued.



(c) $R = 600$

Figure 10. Continued.



(d) $R = 650$

Figure 10. Concluded.

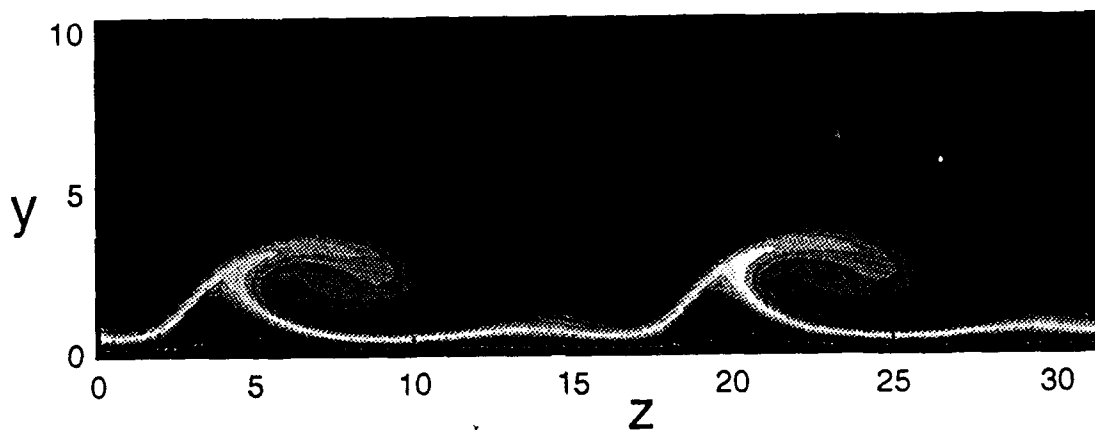


Figure 11. The structure of crossflow vortex as viewed from upstream.

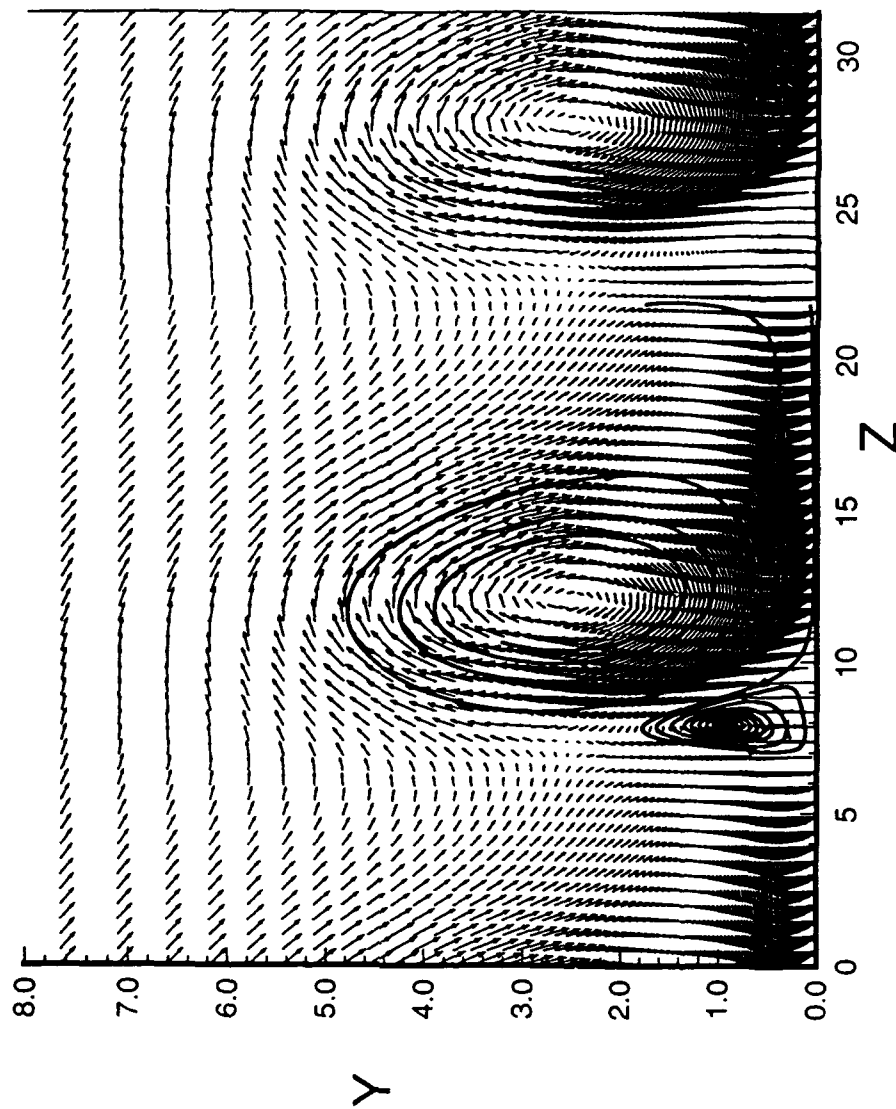


Figure 12. Velocity vector plot at $R = 650$ projected onto a plane perpendicular to the vortex axis.

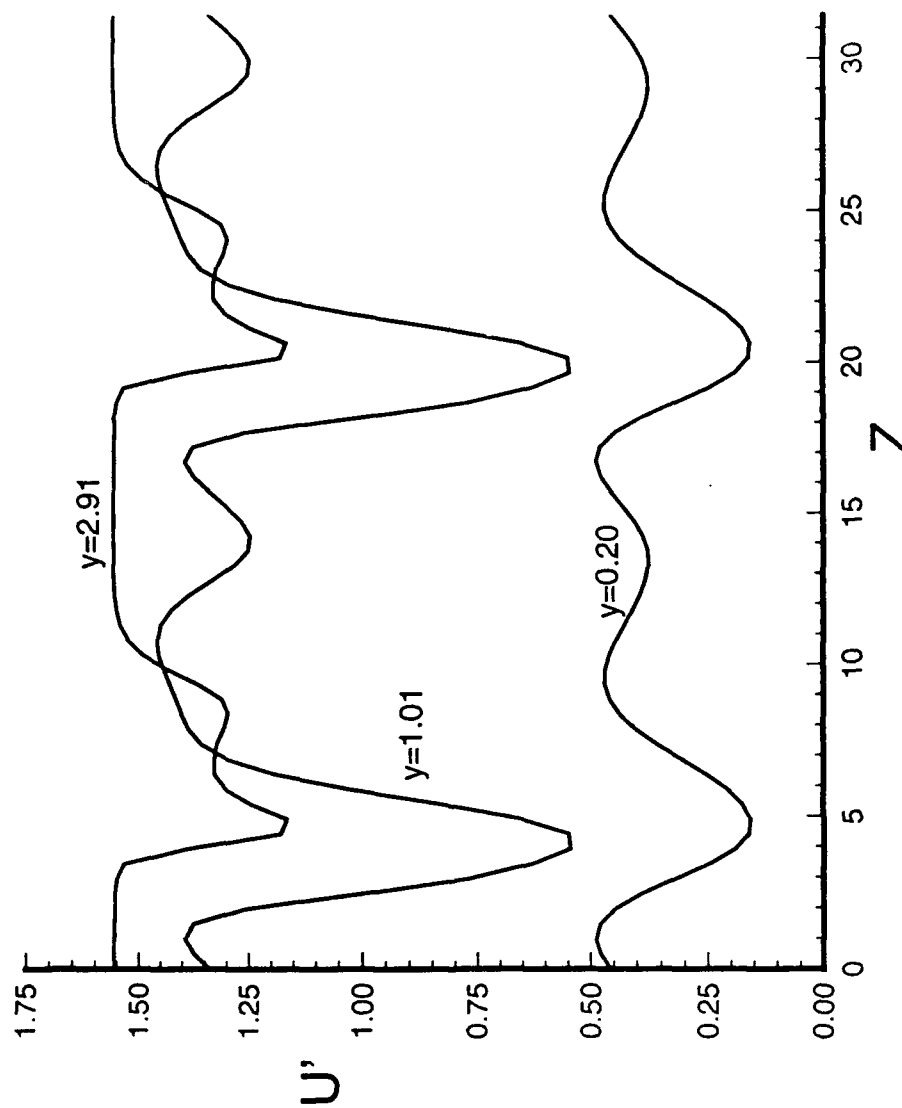
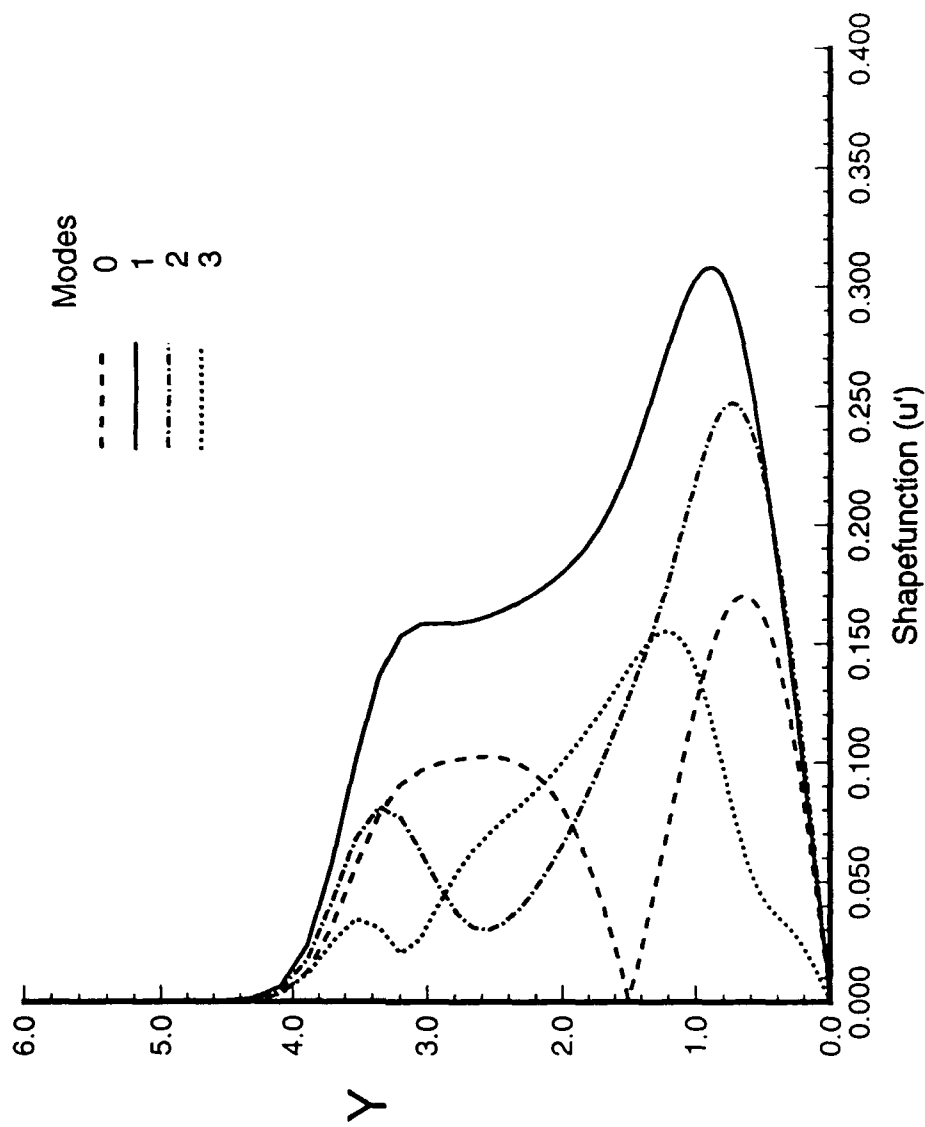
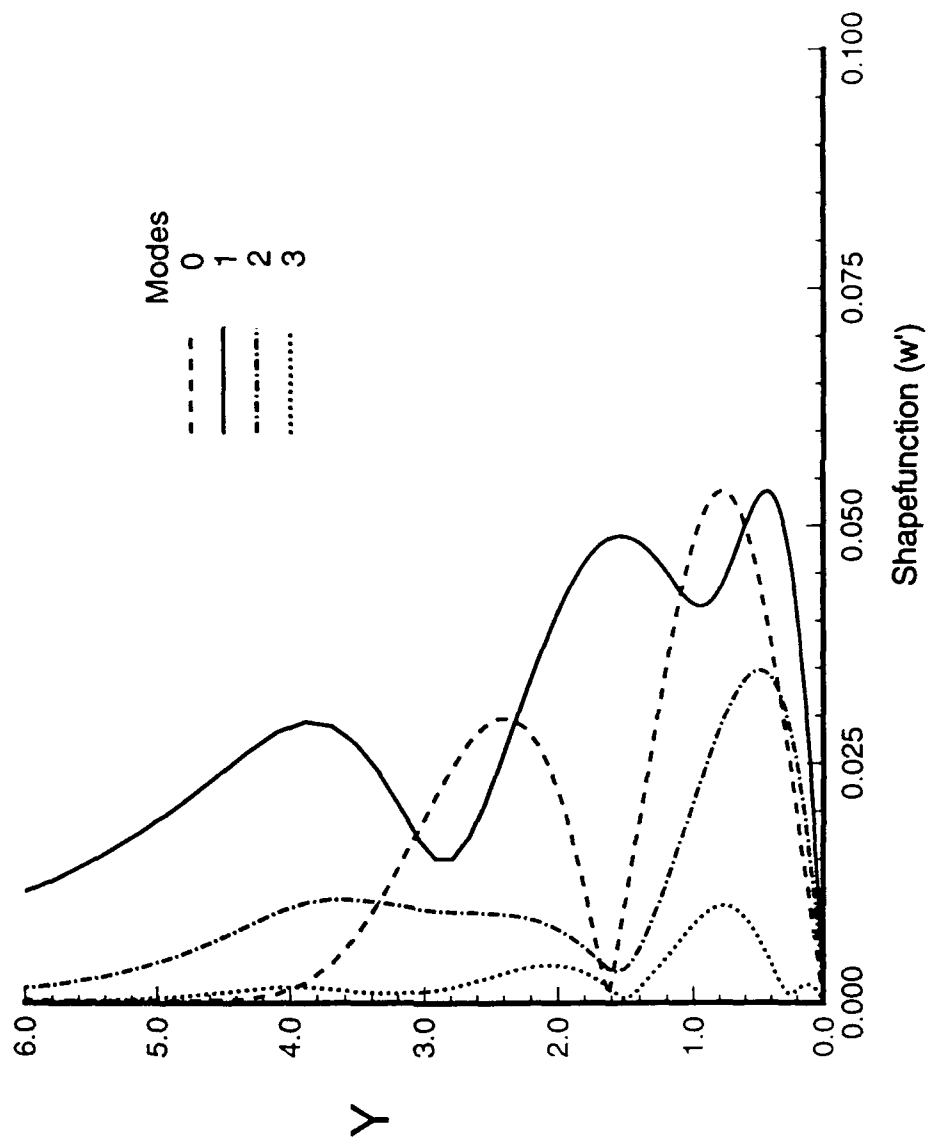


Figure 13. Variation of vortex axial velocity in the spanwise direction at $R = 600$.



(a) along the vortex

Figure 14. Disturbance amplitude functions for the stationary vortex (mode 1) and its harmonics, at $R = 600$.



(b) across the vortex

Figure 14. Concluded.

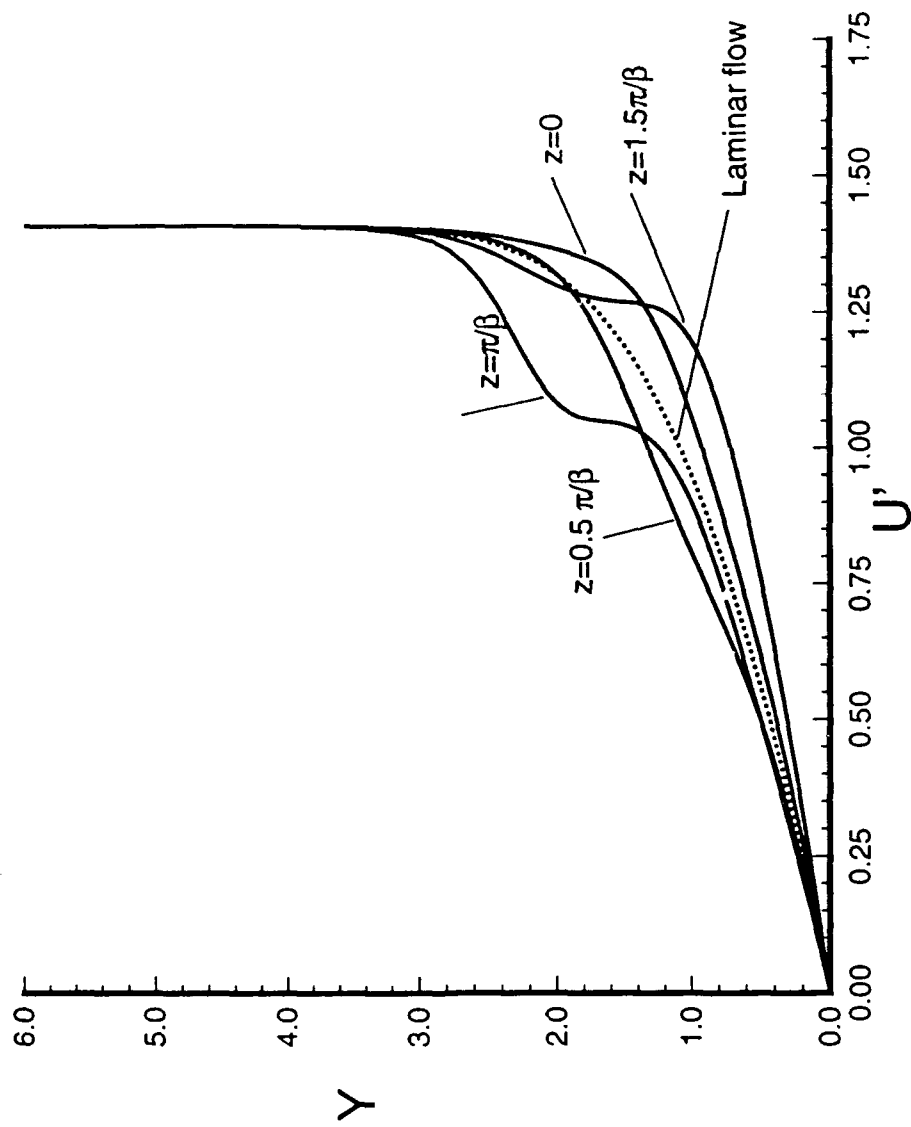
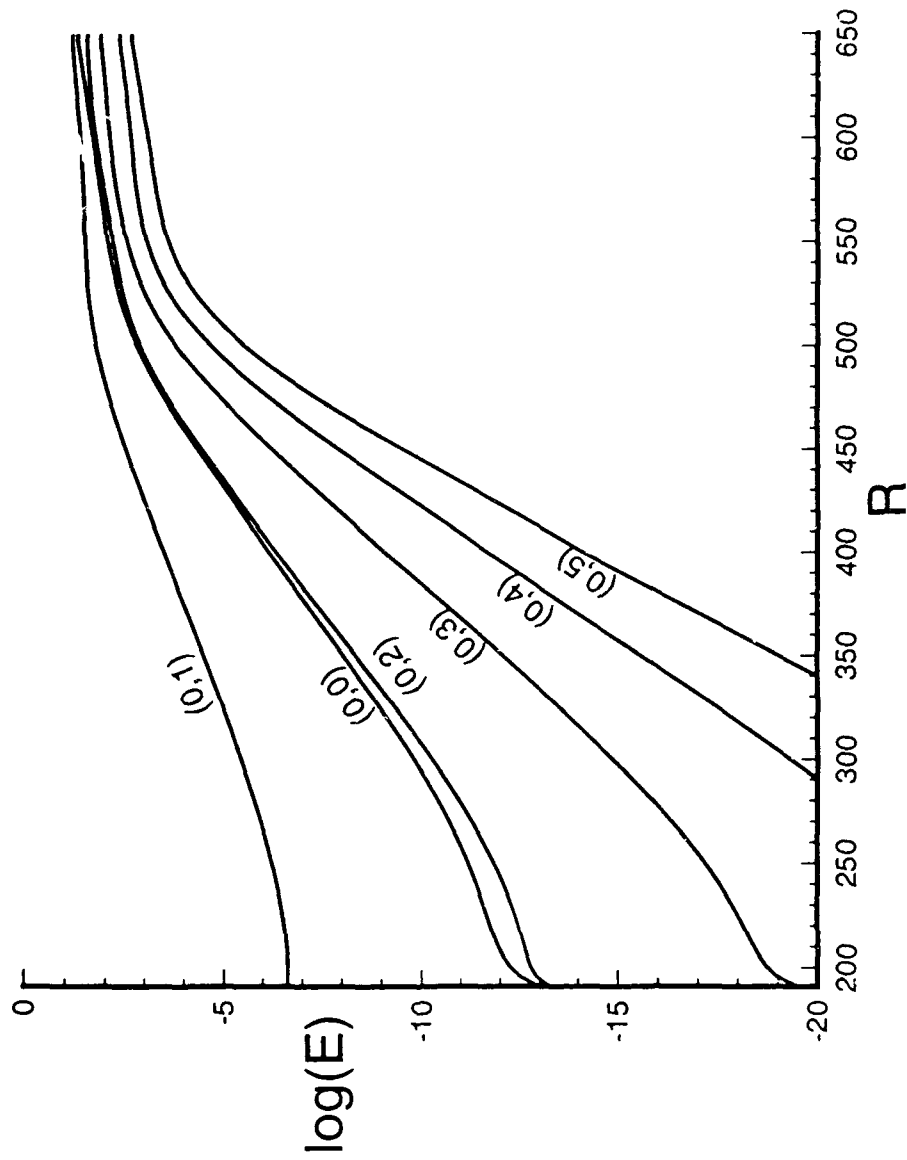
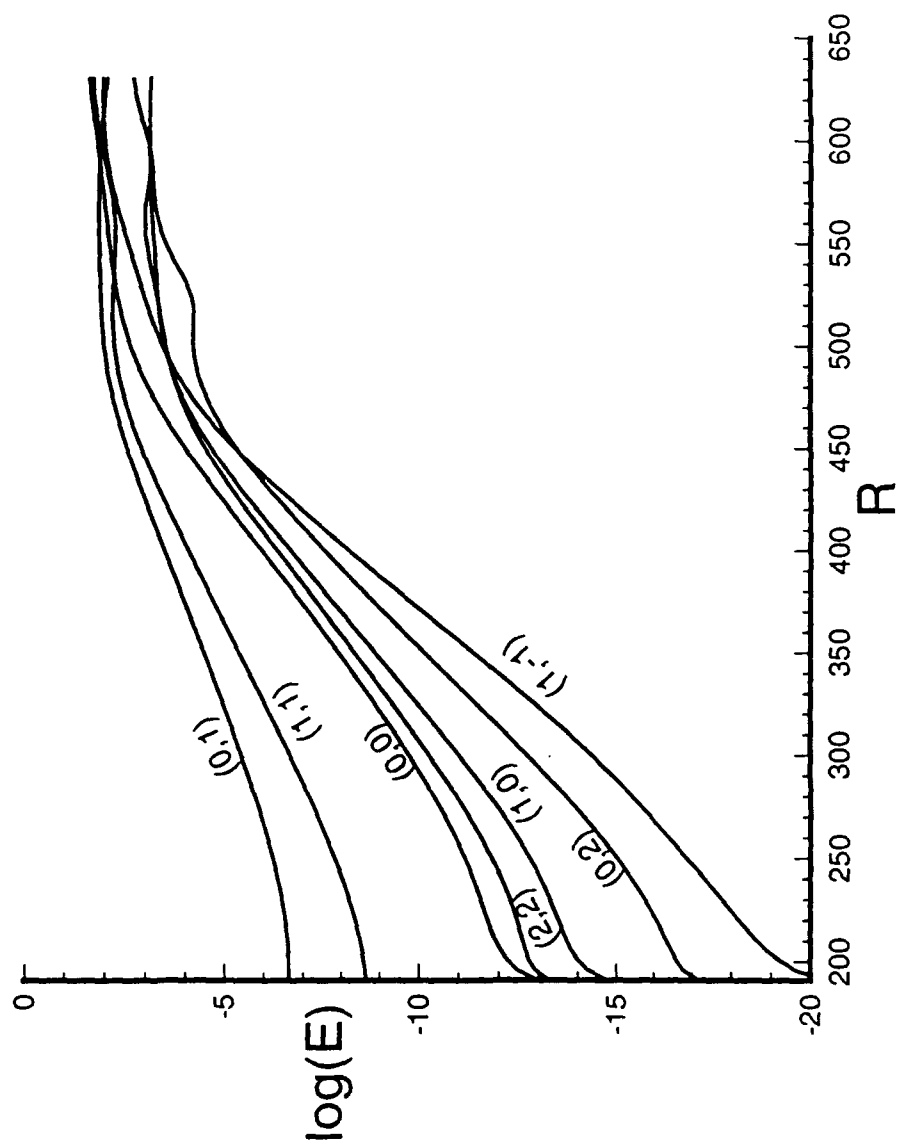


Figure 15. Velocity component along the vortex at different locations z across the vortex, $R = 500$.



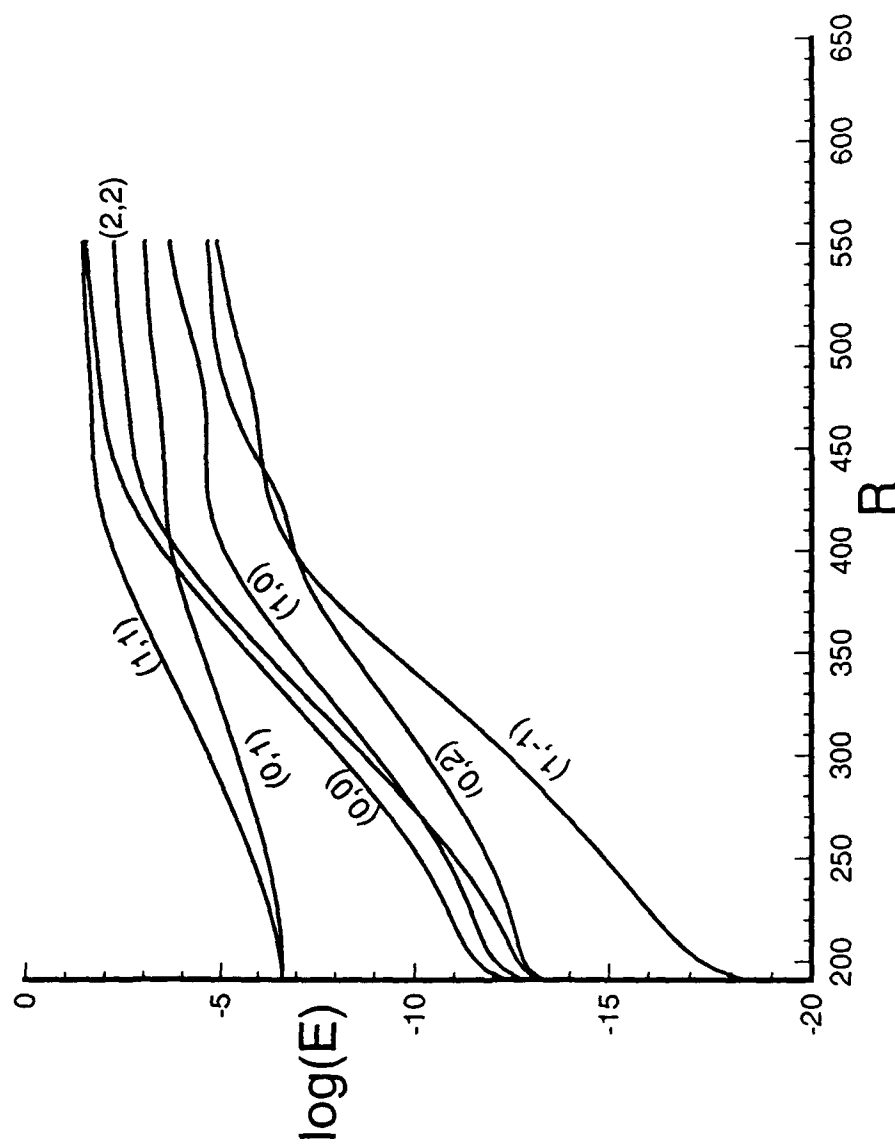
(a) $A_s = .1\%$, $A_t = 0$

Figure 16. Evolution of integrated (over y) disturbance energy for various modes at $\bar{R} = 500$; the first index refers to frequency and the second index refers to spanwise wavenumber.



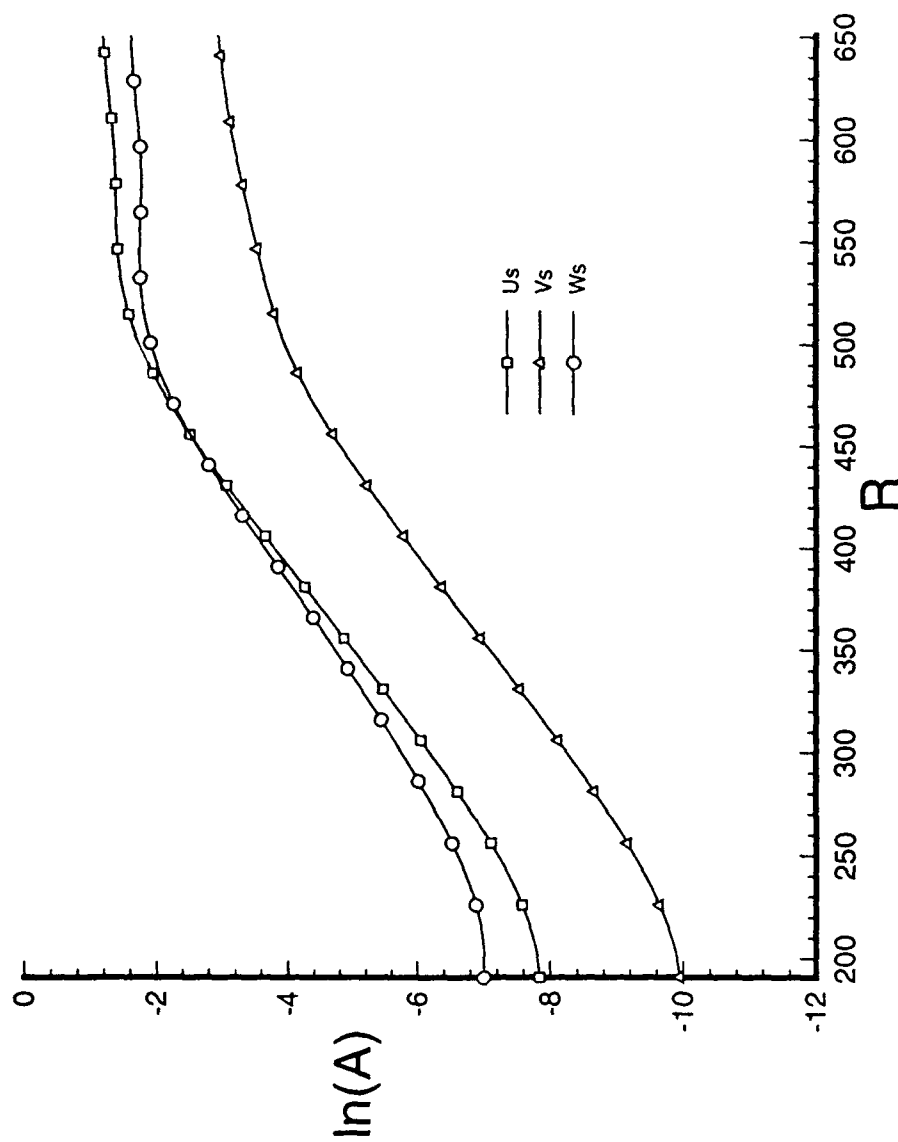
(b) $A_s = .1\%$, $A_t = .01\%$

Figure 16. Continued.



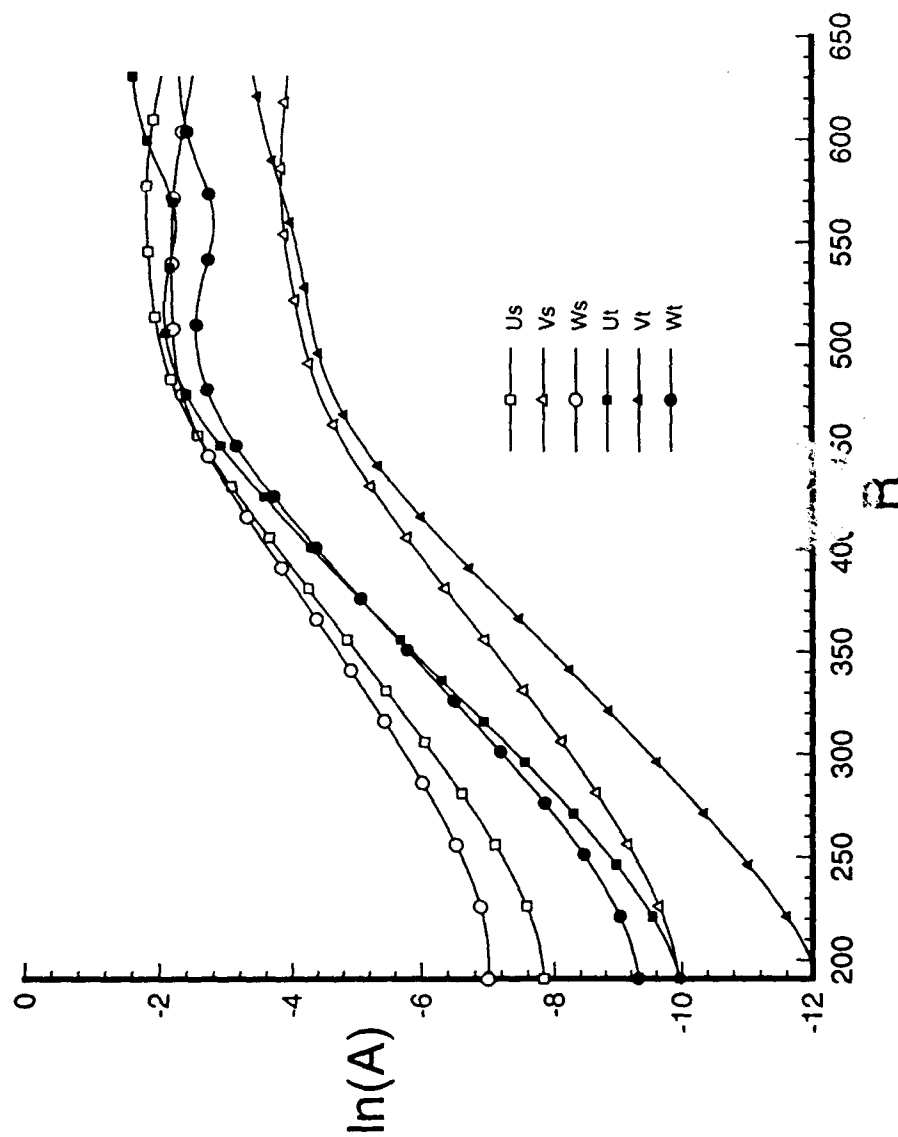
(c) $A_s = .1\%, A_t = .1\%$

Figure 16. Concluded.



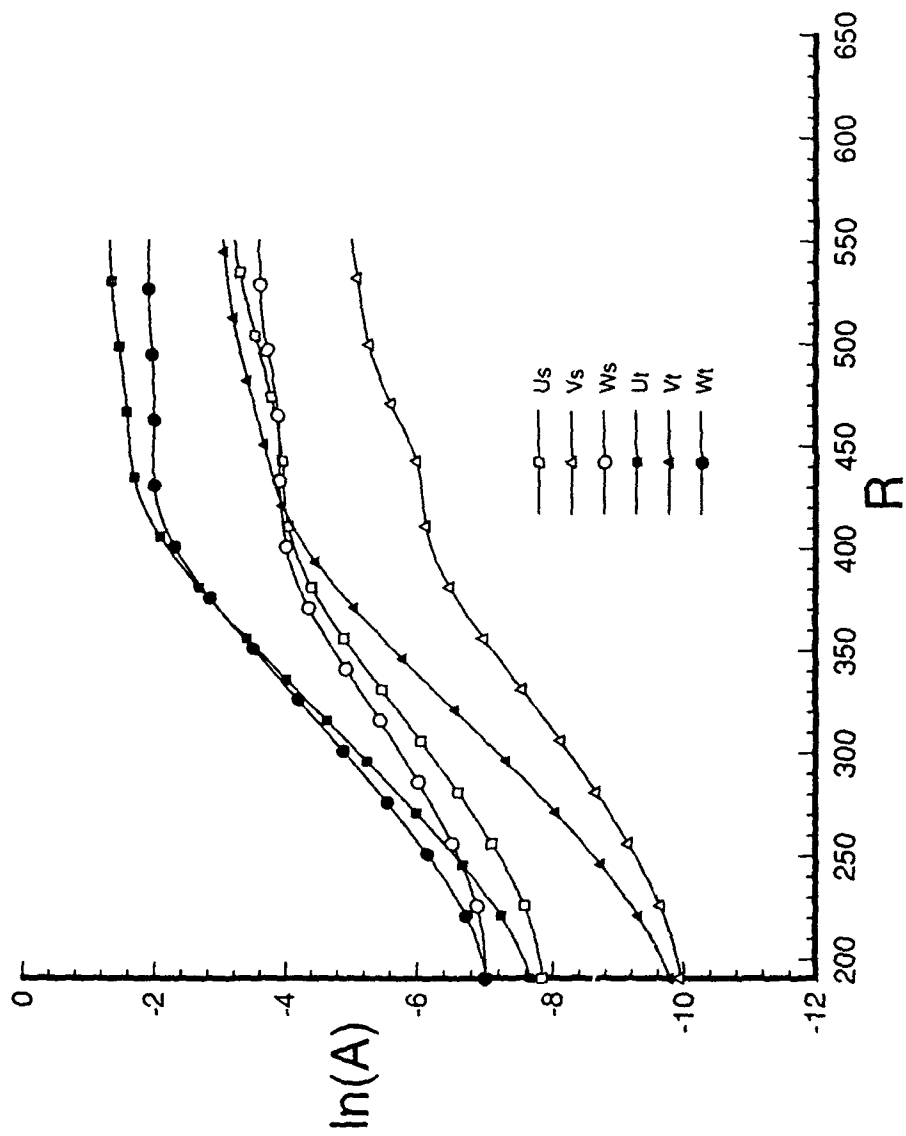
(a) $A_s = .1\%$, $A_t = 0$

Figure 17. Evolution of maximum (over y) amplitude of the disturbance velocity components $(\hat{u}, \hat{v}, \hat{w})$ for stationary and traveling modes.



(b) $A_s = .1\%$, $A_t = .01\%$

Figure 17. Continued.



(c) $A_s = .1\%$, $A_t = .1\%$

Figure 17. Concluded.

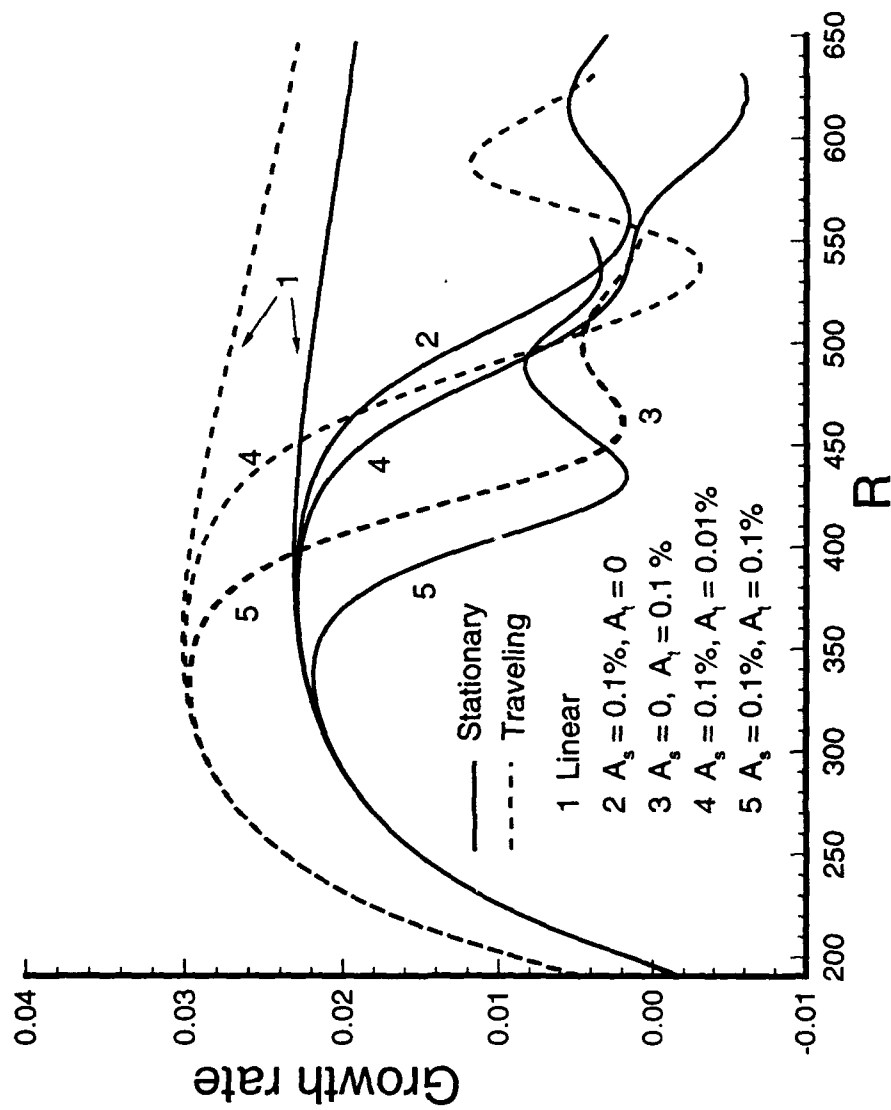
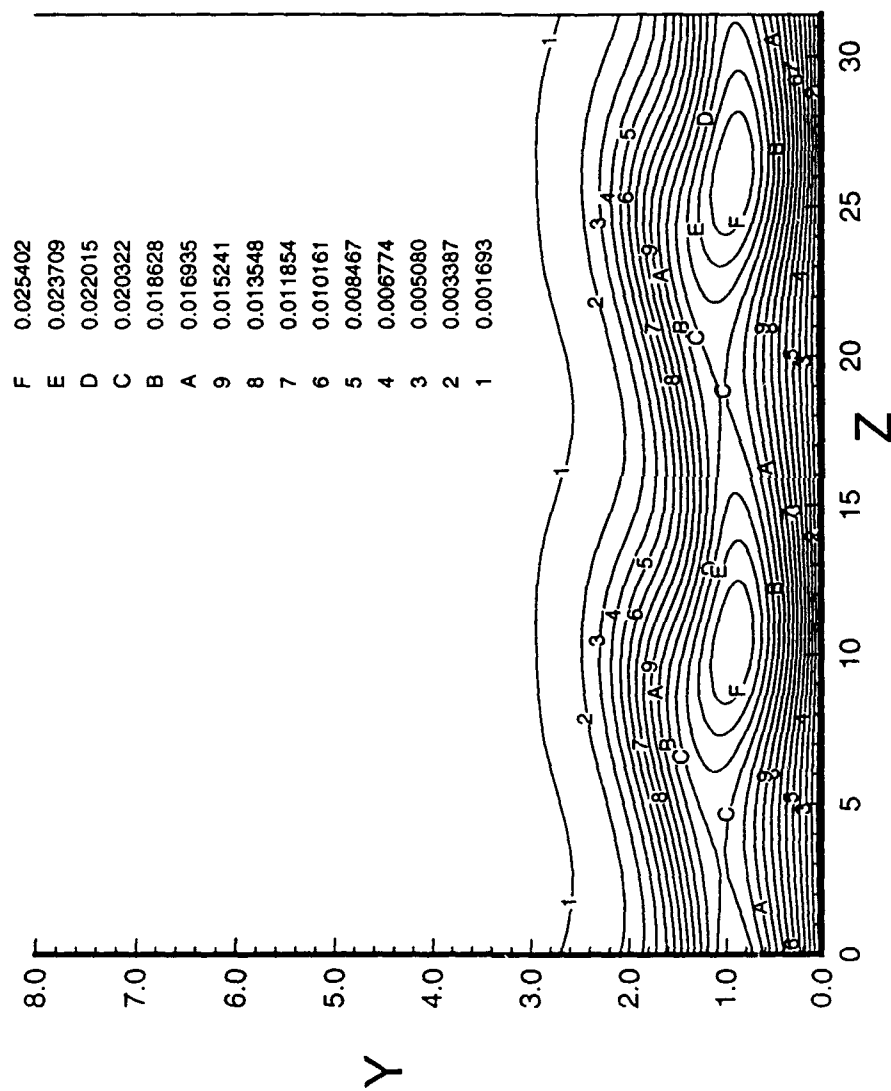
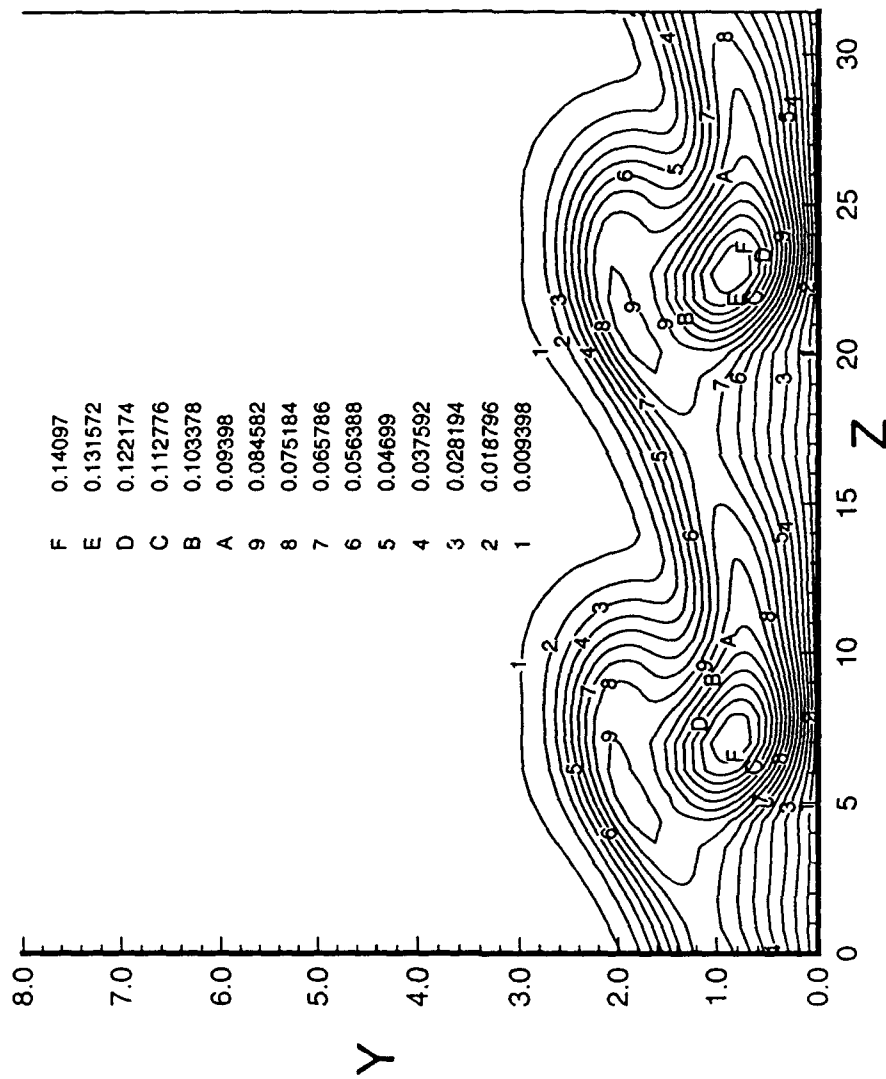


Figure 18. Growth rate of stationary and traveling modes with and without interaction.



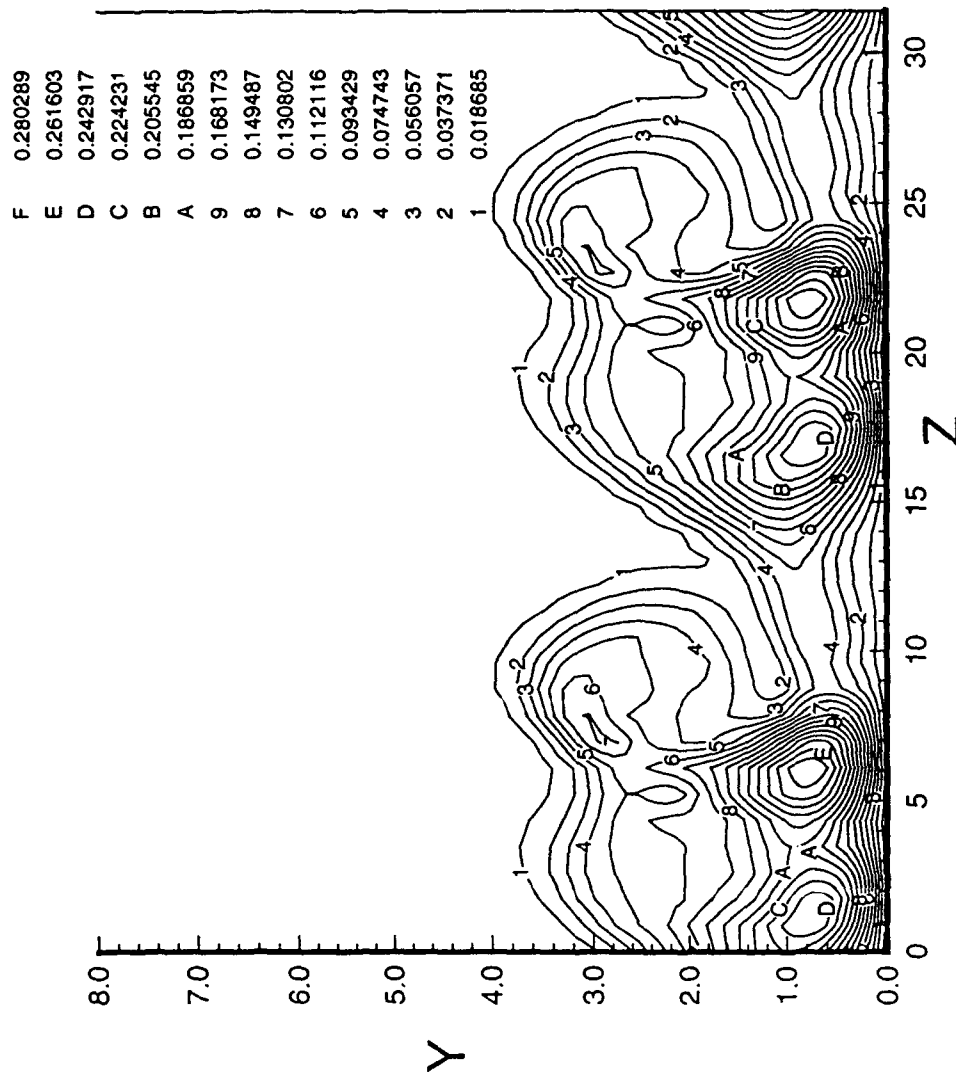
(a) $R = 431$

Figure 19. Variation of u_{rms} in the y - z plane for the wave interaction case with $A_1 = .01$ percent.



(b) $R = 500$

Figure 19. Continued.



(c) $R = 600$

Figure 19. Concluded.

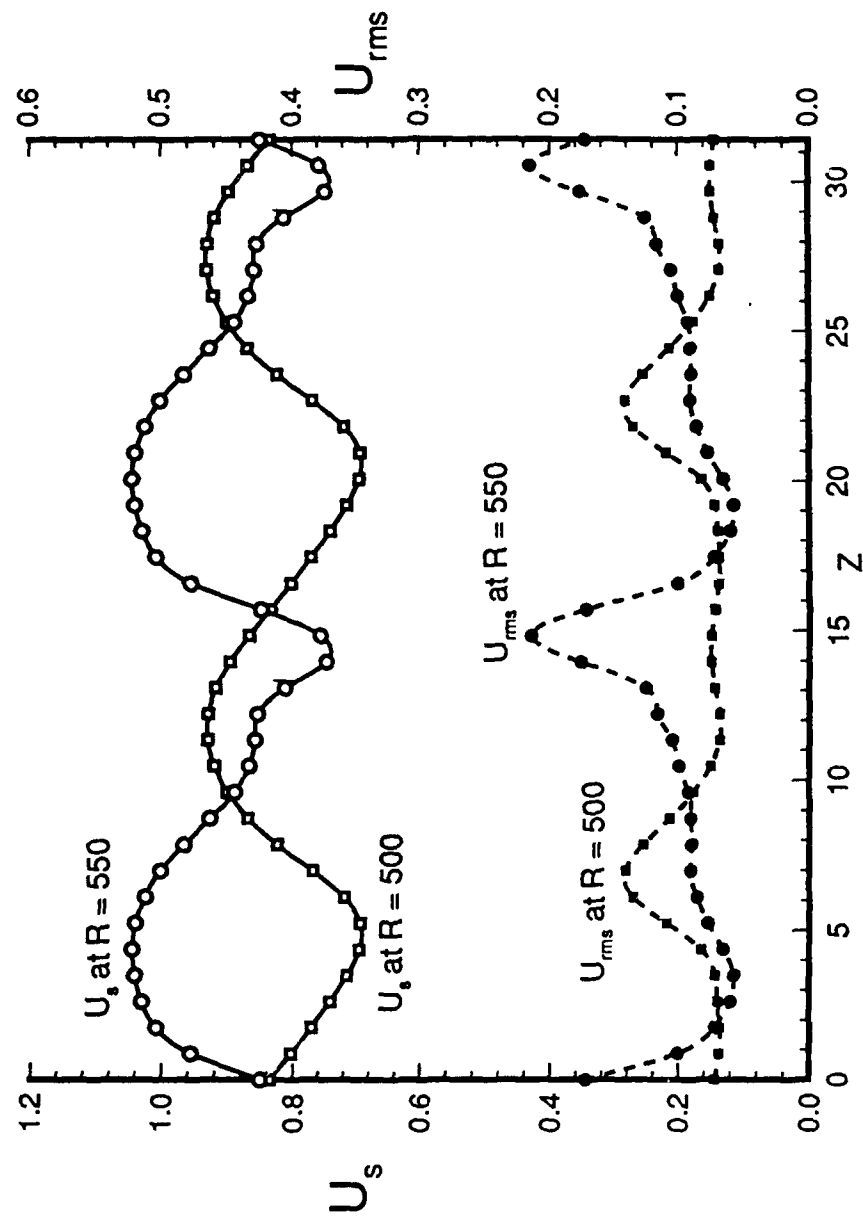


Figure 20. Spanwise variation of chordwise velocity ($U_{stationary}$ and \bar{U}_{rms}) at $y = 1.048$ for the wave interaction case with $A_t = .01$ percent.

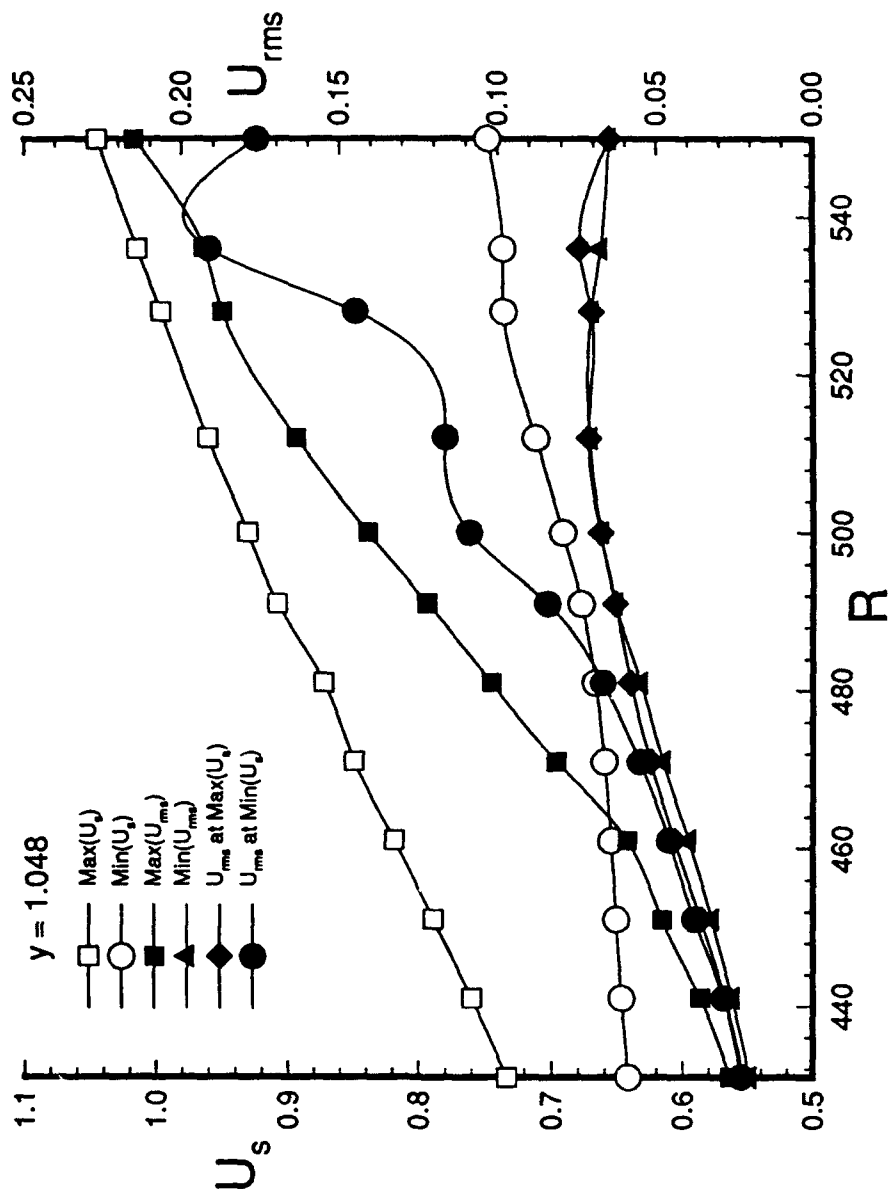


Figure 21. Variation of maximum and minimum $u_{stationary}$ and \bar{u}_{rms} at $y = 1.048$ with Reynolds number. \bar{u}_{rms} at locations where $u_{stationary}$ is maximum and minimum is also given.

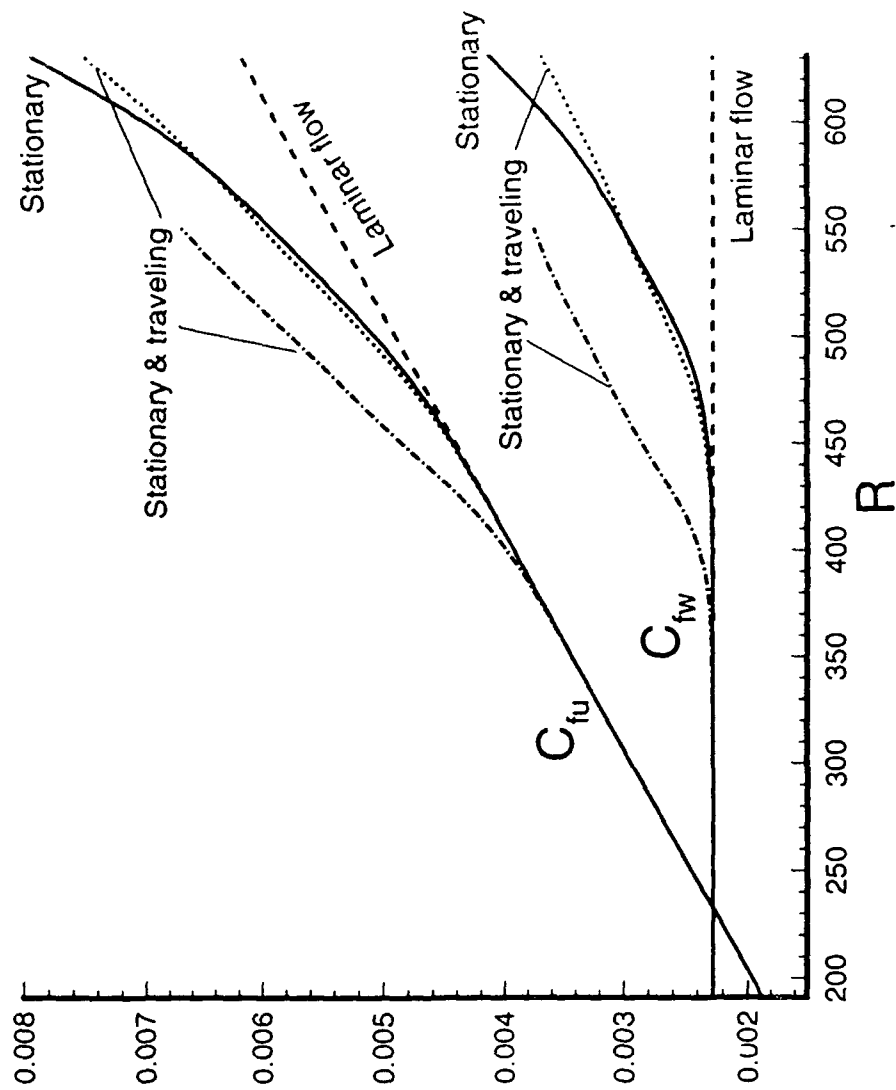


Figure 22. Chordwise (C_{fu}) and spanwise (C_{fw}) skin friction coefficients for cases (a), (b), (c) of figure 16.

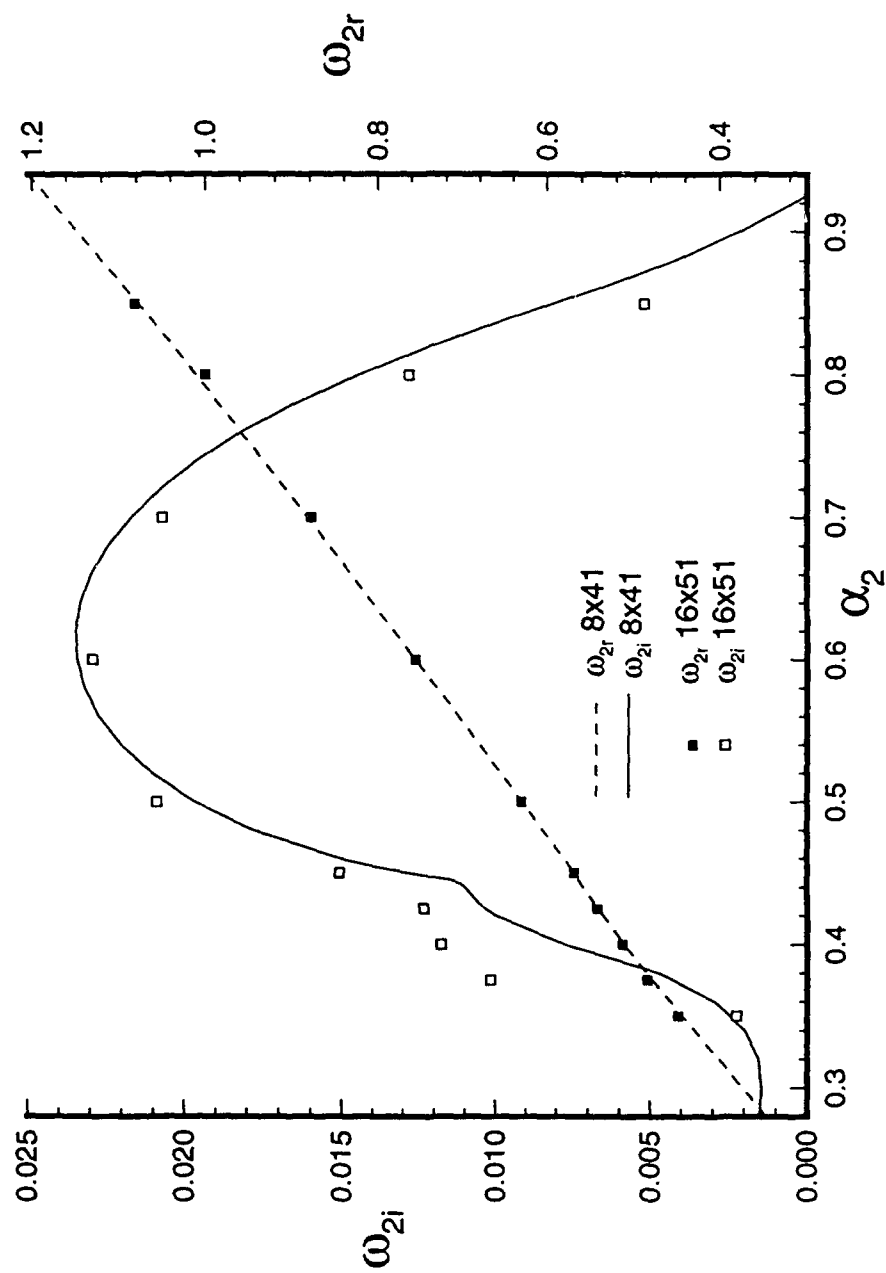


Figure 23. Temporal growth rate and frequency of the secondary instability in the 3D boundary layer at $R = 550$. Results from two different numerical resolutions are shown.

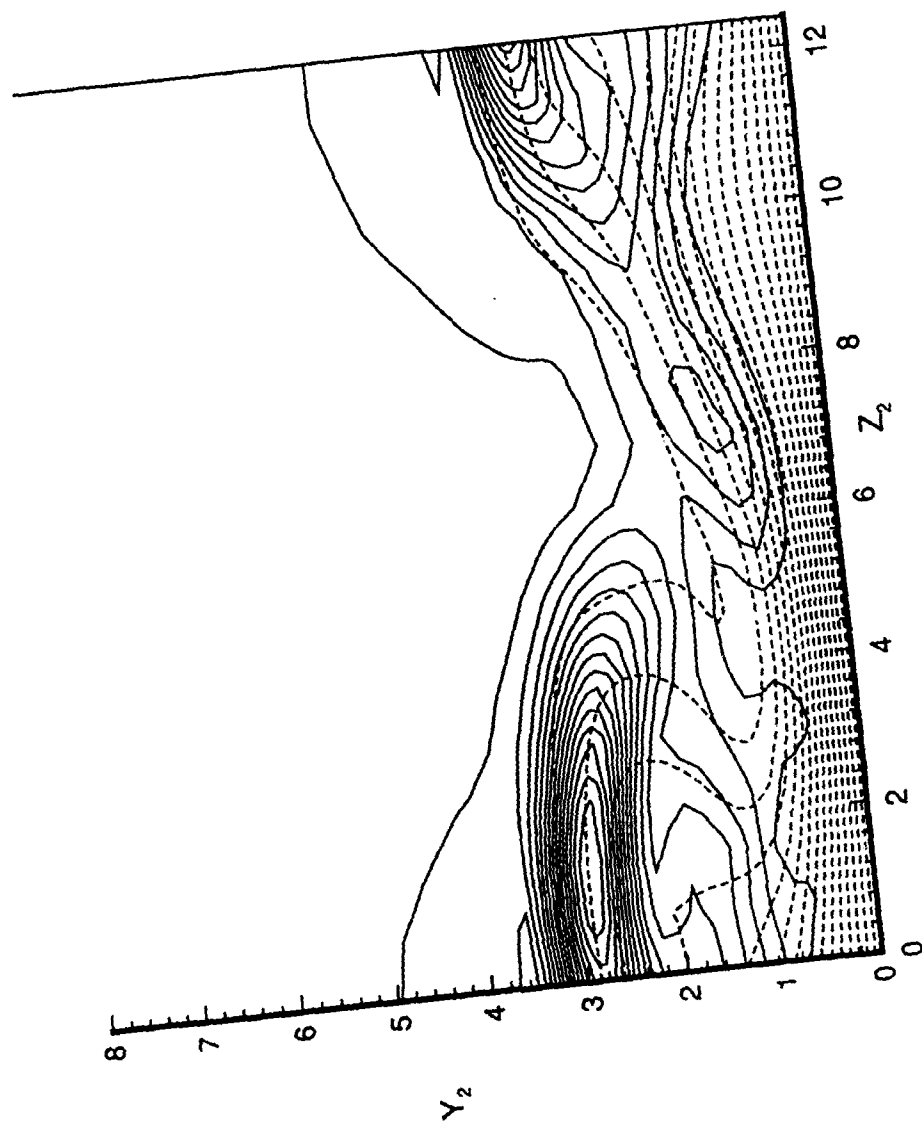


Figure 24. The x_2 -component of mean flow (dashed lines) and the $|u_2|$ eigenfunction (solid lines).

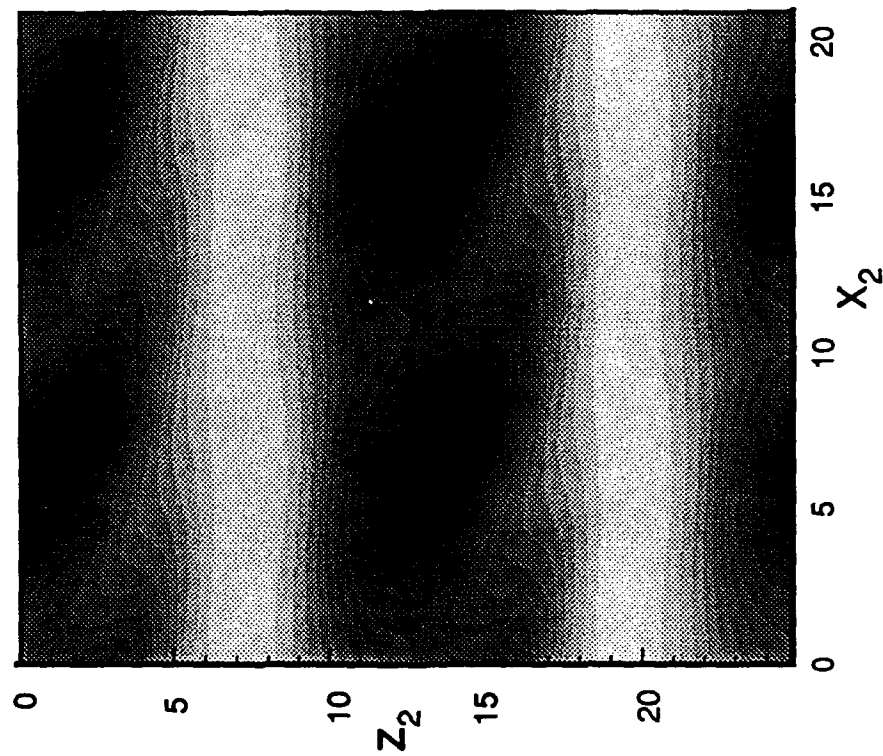


Figure 25. The distribution of x_2 -total velocity component in x_2 - z_2 plane at $y_2 = 2.82$. The $|\mu_2|$ eigenfunction was assigned an amplitude of 5 percent.

PART C

On the Nature of PSE Approximation

Abstract

The recently developed method of Parabolized Stability Equations (PSE) offers a fast and efficient way of analyzing the spatial growth of linear and nonlinear (convective) disturbances in shear layers. For incompressible flows, the governing equations may be represented either in primitive variables or by using other formulations obtained by eliminating the pressure gradient (e.g., vorticity/stream-function formulation). On the other hand, for compressible flows, primitive variables offer a natural and the only choice. We show that the primitive-variable formulation is not well-posed due to the ellipticity introduced by $\partial \hat{p} / \partial x$ term and marching solution usually blows up for sufficiently small step size. However, it is shown that this difficulty can be overcome if the minimum step size is greater than the inverse of the real part of the streamwise wavenumber, α_r . An alternative is to drop the $\partial \hat{p} / \partial x$ term, in which case the residual ellipticity is of no consequence for marching computations with much smaller step sizes.

1. Introduction

The laminar-turbulent transition process in a boundary layer is of great fundamental and practical interest in fluid mechanics. In many cases, transition occurs via the destabilization and subsequent growth of wave structures in the boundary layer. Classical theories concerning the amplification of these waves use quasi-parallel assumption and ignore the growth of the boundary layer. Other theories (Gaster 1974), including the multiple-scales method (Saric & Nayfeh 1975), can deal with the boundary-layer growth locally for given problems. Direct Navier-Stokes solutions (Fasel & Konzelmann 1990) could give very satisfactory results but at the cost of much more CPU time and larger memory size. The recently developed method of parabolized stability equations (PSE) (Herbert 1991, Chang et al. 1991, Bertolotti et al. 1992) offers a fast and efficient way to analyze the spatial growth of instabilities in the boundary layer. In order to briefly describe the PSE method, let us first consider linearized Navier-Stokes equations in primitive variable form:

$$\frac{\partial u}{\partial t} + U \frac{\partial u}{\partial x} + u \frac{\partial U}{\partial x} + V \frac{\partial u}{\partial y} + v \frac{\partial U}{\partial y} + W \frac{\partial u}{\partial z} + w \frac{\partial U}{\partial z} + \frac{\partial p}{\partial x} = \frac{1}{R} \left[\frac{\partial^2 u}{\partial x^2} + \frac{\partial^2 u}{\partial y^2} + \frac{\partial^2 u}{\partial z^2} \right] \quad (1a)$$

$$\frac{\partial v}{\partial t} + U \frac{\partial v}{\partial x} + u \frac{\partial V}{\partial x} + V \frac{\partial v}{\partial y} + v \frac{\partial V}{\partial y} + W \frac{\partial v}{\partial z} + w \frac{\partial V}{\partial z} + \frac{\partial p}{\partial y} = \frac{1}{R} \left[\frac{\partial^2 v}{\partial x^2} + \frac{\partial^2 v}{\partial y^2} + \frac{\partial^2 v}{\partial z^2} \right] \quad (1b)$$

$$\frac{\partial w}{\partial t} + U \frac{\partial w}{\partial x} + u \frac{\partial W}{\partial x} + V \frac{\partial w}{\partial y} + v \frac{\partial W}{\partial y} + W \frac{\partial w}{\partial z} + w \frac{\partial W}{\partial z} + \frac{\partial p}{\partial z} = \frac{1}{R} \left[\frac{\partial^2 w}{\partial x^2} + \frac{\partial^2 w}{\partial y^2} + \frac{\partial^2 w}{\partial z^2} \right] \quad (1c)$$

$$\frac{\partial u}{\partial x} + \frac{\partial v}{\partial y} + \frac{\partial w}{\partial z} = 0 \quad (1d)$$

where x , y and z are the streamwise, wall-normal and spanwise coordinates, respectively, and U , V , W are the corresponding mean velocity components while u , v , w are the disturbance velocity

components. Furthermore, p is the pressure and R is the Reynolds number, $R = U_\infty L / \nu$, where U_∞ , L are the reference scales for velocity and length and ν is the kinematic viscosity.

In the linear PSE method, a wave-like disturbance, ϕ , representing velocity, pressure or vorticity, etc., is assumed to be of the form

$$\phi(x, y, z, t) = \hat{\phi}(x, y)E \quad (2a)$$

$$E = \exp \left(i \left(\int_{x_0}^x \alpha(\xi) d\xi + \beta z - \omega t \right) \right). \quad (2b)$$

Here α and β are the x and z wave numbers, ω is the disturbance frequency and $\hat{\phi}(x, y)$ is the shape function. The physical quantities (u, v , etc.) can be obtained by adding the complex conjugate component. In the above decomposition it has been assumed that the mean flow is independent of the spanwise coordinate z . The first and second derivatives of ϕ can be written as

$$\phi_x = (i\alpha\hat{\phi} + \hat{\phi}_x)E \quad (2c)$$

$$\phi_{xx} = (-\alpha^2\hat{\phi} + i\alpha_x\hat{\phi} + 2i\alpha\hat{\phi}_x + \hat{\phi}_{xx})E \quad (2d)$$

$$\phi_y = \hat{\phi}_y E \quad (2e)$$

$$\phi_{yy} = \hat{\phi}_{yy} E \quad (2f)$$

Substituting (2 and 3) into the linearized Navier-Stokes equations, which could be in primitive variable form, stream-function/vorticity form or other forms, we obtain a set of equations with the $\hat{\phi}(x, y)$'s and α as unknowns. Since there is now one more unknown (namely, $\alpha(x)$) than the equations, another condition is needed for the closure of the system. We take advantage of the slow variation of the mean flow in the streamwise direction and impose a condition on $\alpha(x)$ such that "most" of the waviness and growth of the disturbance are absorbed into the exponential function E , making the shape function $\hat{\phi}(x, y)$ slowly varying with x . Hence, the term containing $\hat{\phi}_{xx}$ (in (3b)) can be dropped and we arrive at a set of new equations in which the only second-order derivatives are those with respect to y . We will call these equations parabolized stability equations (PSE) and ask the question whether these equations are indeed parabolic, i.e., given appropriate initial data can one find a solution by marching along the streamwise direction?

When the basic flow is two-dimensional, the pressure term can be eliminated and the governing equations can be represented in stream function and normal vorticity formulations. When the basic flow is three-dimensional it becomes difficult, particularly for nonlinear disturbances, to reduce the equations to a form other than primitive variable form. In any case, for compressible flows, primitive variables offer a natural and the only choice. Since our ultimate goal is to study the

stability of compressible flow, we can learn about the low Mach number behavior of the compressible PSE equations by studying the numerical stability of incompressible PSE equations in primitive variable formulation. These equations can be derived by using (1) and (2) and can be written in the following form

$$L_0 \hat{\phi} + L_1 \frac{\partial \hat{\phi}}{\partial x} + L_2 \frac{\partial \hat{\phi}}{\partial y} + L_3 \frac{\partial^2 \hat{\phi}}{\partial y^2} = 0 \quad (3a)$$

where $\hat{\phi} = (\hat{u}, \hat{v}, \hat{w}, \hat{p})^T$ and L_0-L_4 are square matrices given in Appendix I. Equation (3a) is to be solved subject to the constraint (imposing the condition that the shape function varies slowly with x)

$$F(\alpha, \hat{\phi}) = 0 \quad (3b)$$

We will show that when the primitive-variables are used, the equations are only partially parabolized. The gradient $\partial \hat{p} / \partial x$ represents the dominant part of the residual ellipticity. For easy reference, we call this term as the pressure gradient. (We should stress here that $\partial \hat{p} / \partial x$ represents only a small part of the physical pressure gradient $\partial p / \partial x$. Most of the physical pressure gradient is carried by the term $i\alpha \hat{p}$, see Eq. (2c)). This ellipticity will cause the marching procedure to fail. The same difficulties are encountered in the Parabolized Navier-Stokes equations (PNS) (Rubin, 1981).

By suitable substitutions, the PSE can also be written in the form of a set of first-order partial differential equations and an additional functional F as

$$\mathcal{A} \hat{\psi} + \mathcal{B} \frac{\partial \hat{\psi}}{\partial x} + I \frac{\partial \hat{\psi}}{\partial y} = 0 \quad (4a)$$

$$F(\alpha, \hat{\psi}) = 0 \quad (4b)$$

where $\mathcal{A} = \mathcal{A}(x, y, \alpha)$ and $\mathcal{B} = \mathcal{B}(x, y, \alpha)$ are square matrices, I is the identity matrix and $\hat{\psi}$ is a vector. If quasi-parallel flow is assumed, then (4) can be reduced to the well-known Orr-Sommerfeld equation. Equation (4a) is solved numerically by marching from the initial station at $x = x_0$ with some initial condition, $\hat{\psi}(x_0, y)$. The solution at $x = x_0 + \Delta x$ is computed with $\alpha(x_0 + \Delta x) = \alpha(x_0)$ as a first approximation, then a new α is calculated using Eq. (4b). Equation (4a) is solved again with the new value of α . This process continues until the solution converges. The marching is then carried to the next x -station. The stability of the marching procedure depends on the discretization scheme, the iterative process for evaluating α and, most importantly, the mathematical nature of PSE.

In the primitive-variable form, the matrices in Eq. (4a) for a flat geometry are given as follows

$$\mathcal{A} = \begin{bmatrix} 0 & 0 & 0 & 0 & -1 & 0 \\ i\alpha & 0 & i\beta & 0 & 0 & 0 \\ 0 & 0 & 0 & 0 & 0 & -1 \\ -i\alpha V + Vx & \Delta + V_y & -i\beta V & 0 & \frac{i\alpha}{R} & \frac{i\beta}{R} \\ -(\Delta + U_x)R & U_y R & 0 & -i\alpha R & -VR & 0 \\ -W_x R & -W_y R & -\Delta R & -i\beta R & 0 & -VR \end{bmatrix} \quad (5)$$

where $\Delta = -i\omega + i\alpha U + i\beta W + \frac{\alpha^2 + \beta^2 - i \frac{d\alpha}{dx}}{R}$.

$$\mathcal{B} = \begin{bmatrix} 0 & 0 & 0 & 0 & 0 & 0 \\ 1 & 0 & 0 & 0 & 0 & 0 \\ 0 & 0 & 0 & 0 & 0 & 0 \\ -V & \Gamma & 0 & 0 & \frac{1}{R} & 0 \\ -\Gamma R & 0 & 0 & -R & 0 & 0 \\ 0 & 0 & \Gamma R & 0 & 0 & 0 \end{bmatrix} \quad (6)$$

where $\Gamma = U - \frac{2i\alpha}{R}$, U , V and W are the three velocity components of the basic flow, α and β are the wave numbers in the x and y - directions respectively, and

$$\bar{\psi} = (\hat{u}, \hat{v}, \hat{w}, \hat{p}, \partial \hat{u} / \partial y, \partial \hat{w} / \partial y)^T \quad (7)$$

The functional $F(\alpha, \bar{\psi}) = 0$, can be chosen in several ways. For example, we can impose the condition that the maximum of the velocity component, \hat{u} , is constant or that

$$\frac{\int_0^{\infty} q^* \frac{\partial q}{\partial x} dy}{\int_0^{\infty} |q|^2 dy} = 0 \quad (8)$$

where $q = (\hat{u}, \hat{v}, \hat{w})$ and $*$ represents the complex conjugate. An iterative procedure for α based on Eq. (8) is given as follows,

$$\alpha_{n+1} = \alpha_n - i \frac{\int_0^\infty q_n^* \frac{\partial q_n}{\partial x} dy}{\int_0^\infty |q_n|^2 dy} \quad (9)$$

We note that, since α is complex, Eq. (9) represents a two-dimensional iterative map.

2. Mathematical Nature of PSE

For an initial value problem

$$\frac{\partial u}{\partial x} = A \frac{\partial u}{\partial y} + Bu \quad (10)$$

$$u(0, y) = f(y) \quad (11)$$

where $f, u \in C^n$, $A, B \in C^{n \times n}$ and $y \in \mathfrak{R}$, the solutions can be obtained by Fourier transform. In Fourier space, Eq. (10) and (11) become

$$\frac{d\tilde{u}}{dx} = (i\eta A + B)\tilde{u} \quad (12)$$

$$\tilde{u}(0) = \tilde{f}(\eta) \quad (13)$$

where \tilde{u} and \tilde{f} are Fourier transforms of u and f , respectively, and η is the wavenumber in y -direction. The solution to (12) and (13) is of the form

$$\tilde{u} = g(\eta)e^{\lambda x} \quad (14)$$

where $g(\eta) \in C^n$. Substitution of (14) into (12) yields an algebraic equation for the eigenvalue $\lambda = \lambda(\eta)$,

$$[i\eta A + B - \lambda I] = 0 \quad (15)$$

Assuming that all n eigenvalues of Eq. (15) have distinct corresponding eigenvectors, $g_j(\eta)$, then

$$\tilde{u} = \sum_{j=1}^n A_j g_j(\eta) e^{\lambda_j x}$$

The constants $A_j \in \mathfrak{R}$ can be determined by solving the $n \times n$ linear system

$$\sum_{j=1}^n g_j(\eta) A_j = \tilde{f}(\eta)$$

Hence, we obtain the solution to Eq. (10) and (11)

$$u(x, y) = \sum_{j=1}^n \frac{1}{2\pi} \int_{-\infty}^{\infty} A_j e^{i\eta y} g_j(\eta) e^{\lambda_j x} d\eta. \quad (16)$$

If $|e^{\lambda_j x}|$ is unbounded for $|\eta| \rightarrow \infty$, the integral in Eq. (16) may not exist, and the initial value problem defined by Eqs. (10) and (11) are said to be ill-posed (Kreiss & Lorenz (1989)).

In finding the eigenvalues $\lambda_j(\eta)$, both matrices A and B are used in Eq. (15). In fact, subject to the condition that the eigenvalues of A are non-zero and distinct, the well-posedness of Eq. (10) is determined by the eigenvalues of A only. This can be easily verified. We decompose A such that $A = P\Lambda P^{-1}$, where P is a matrix whose columns consist of the eigenvectors of A , and Λ is a diagonal matrix whose elements are eigenvalues of A . Multiplying Eq. (15) by $|P^{-1}|P|$, we obtain

$$|i\eta\Lambda + P^{-1}BP - \lambda I| = 0$$

As $|\eta| \rightarrow \infty$, the matrix $i\eta\Lambda + P^{-1}BP$ becomes diagonally-dominant. Applying the Gershgorin Circle Theorem (see Golub & Van Loan, 1983), we find that the eigenvalue, λ_j , approaches $\eta\sigma_j$, where σ_j is the j th eigenvalue of A . Therefore, the eigenvalues of A determine the well-posedness of Eq. (10). This is reminiscent of the classification of partial differential equations with one dependent variable where only the "principal part" is required. However, we must stress that, if some of the eigenvalues of A are zero, then all matrices in Eq. (15) must be used to obtain the correct result.

For various PSE formulations, the equations cannot always be written in the form of Eq. (10), e.g., when matrix B in Eq. (4) is singular. Here, we adopt the approach whereby Eq. (14) is substituted into the given form of PSE and all matrices are kept for determining the well-posedness.

We now consider and analyze the well-posedness of the initial value problem associated with the PSE equations. The system consisting of Eqs. (3a) and (3b) (or the corresponding system 4(a) and 4(b)) is nonlinear since α appears in the coefficient matrices. In order to simplify the numerical stability analysis of the marching procedure, we will assume that α is known a priori. We choose a simple two-dimensional basic flow ($W = 0$, $\partial/\partial z = 0$) with constant velocity-components and apply Fourier transform in y -direction, i.e., let $\hat{u}(x, y) = \tilde{u}(x)\exp(i\eta y)$. After some algebra, we can write Eq. (3a) as follows,

$$\frac{d}{dx} \begin{pmatrix} \tilde{u} \\ \tilde{v} \\ \tilde{p} \end{pmatrix} = \begin{bmatrix} -i\alpha & -i\eta & 0 \\ 0 & -\frac{C}{D} & -i\frac{\eta}{D} \\ -C+i\alpha D & i\eta D & -i\alpha \end{bmatrix} \begin{pmatrix} \tilde{u} \\ \tilde{v} \\ \tilde{p} \end{pmatrix} \quad (17)$$

where $C = i\alpha U - i\omega - i\frac{d\alpha}{dx} + \frac{\alpha^2}{R} + i\eta V + \frac{\eta^2}{R}$ and $D = U - 2i\frac{\alpha}{R}$. The three eigenvalues of the matrix in Eq. (17) are given by

$$\lambda_1 = \eta - i\alpha, \quad \lambda_2 = -\eta - i\alpha, \quad \lambda_3 = -\frac{C}{D}, \quad (18)$$

For a well-posed initial value problem, it is required that $\text{Real } \lambda_j < 0$ for $|\eta| \rightarrow \infty$. Since η can take any value for general initial conditions, λ_1 and λ_2 have positive real parts for some η . Therefore, Eq. (17) is not well-posed for initial value problem and some approximation must be made for a stable marching solution. We will discuss it in the next section.

Due to the complicated nature of λ_3 , it is not easy to find the sign of its real part. However, in order to determine the well-posedness, we only need to know the behavior of λ_3 as $|\eta| \rightarrow \infty$, provided that the coefficient of the highest order term in η is not purely imaginary. In this limit, we have

$$\lambda_3 \rightarrow -\frac{\eta^2}{R} \frac{1}{(U - 2i\alpha/R)} = -\frac{\eta^2}{R} \frac{(U + 2\alpha_i/R) + 2i\alpha_r/R}{(U + 2\alpha_i/R)^2 + 4\alpha_r^2/R^2} \quad (19)$$

Therefore,

$$\text{Real}(\lambda_3) \rightarrow -\frac{\eta^2}{R} \frac{U + 2\alpha_i/R}{(U + 2\alpha_i/R)^2 + 4\alpha_r^2/R^2} \quad (20)$$

Hence, for growing waves ($\alpha_i < 0$), real $\lambda_3 > 0$ for sufficiently small U , i.e.,

$$U < \frac{-2\alpha_i}{R} \quad (21)$$

For large Reynolds number and small α_i (typically $O(10^2)$ and $O(10^{-2})$, respectively), condition (21) is satisfied only in a very small neighborhood of the wall. As we will show later, difficulties in numerical solution never arise from λ_3 .

3. Stability of the Marching Procedure

We will now show that marching procedure can be made stable by using a sufficiently large step size, δx , as in PNS for mean flow, and we will derive a condition for stability. We note that, since the eigenvalues are distinct, the matrix in Eq. (12) is diagonalizable, and therefore, Eq. (17) can be written as

$$\frac{d\bar{\phi}}{dx} = \begin{bmatrix} \lambda_1 & 0 & 0 \\ 0 & \lambda_2 & 0 \\ 0 & 0 & \lambda_3 \end{bmatrix} \bar{\phi} \quad (22)$$

where $\bar{\phi}$ is a vector whose components are linear combinations of \tilde{u} , \tilde{v} and \tilde{p} . These are three decoupled equations, each of which is of the form

$$\frac{d\phi}{dx} = \lambda\phi \quad (23)$$

If this equation is solved with backward difference with step-size δx , von Neumann analysis leads to an amplification factor given by

$$\gamma = \frac{1}{1 - \delta x \lambda} \quad (24)$$

Numerical stability requires $|\gamma| < 1$, which can be satisfied if $(1 - \lambda_r \delta x)^2 + \lambda_i^2 \delta x^2 > 1$ and hence, $\delta x > 2\lambda_r / (\lambda_r^2 + \lambda_i^2)$. Since λ depends on η , then minimum step size is given by

$$\delta x_{\min} = \sup_{\eta} \left(\frac{2\lambda_r}{\lambda_r^2 + \lambda_i^2} \right) \quad (25)$$

Equation (25) implies that there is no step-size restriction if $\lambda_r \leq 0$, otherwise the step size has to be greater than some finite value if the marching is to be stable. For example, von Neumann analysis of, say, the equation associated with λ_2 leads to an amplification factor given by

$$\gamma_2 = \frac{1}{(1 - (\eta - \alpha_i) \delta x) + i \alpha_r \delta x} \quad (26)$$

Numerical stability requires $|\gamma_2| < 1$ for all η . This can be achieved only if $\delta x > \frac{1}{|\alpha_r|}$. For smaller δx , numerical instability occurs for

$$\eta \in \left(\frac{1}{\delta x} - \alpha_i - \frac{\sqrt{1 - \alpha_r^2 \delta x^2}}{\delta x}, \frac{1}{\delta x} - \alpha_i + \frac{\sqrt{1 - \alpha_r^2 \delta x^2}}{\delta x} \right).$$

This is graphically depicted in Fig. 1 for real α .

If Eq. (4a) is discretized directly by using backward difference for x -derivatives and central difference for the y -derivatives, then Von Neumann analysis of numerical stability leads to the following

$$\begin{vmatrix} \sigma\lambda & 0 & 0 & 0 & -\lambda & 0 \\ \mu & \sigma\lambda & i\beta\lambda & 0 & 0 & 0 \\ 0 & 0 & \sigma\lambda & 0 & 0 & -\lambda \\ -V\mu & \kappa & -i\beta V\lambda & \sigma\lambda & \frac{\mu}{R} & i\frac{\beta}{R}\lambda \\ -\kappa R & 0 & 0 & -\mu R & (\sigma - VR)\lambda & 0 \\ 0 & 0 & -\kappa R & -i\beta R\lambda & 0 & (\sigma - VR)\lambda \end{vmatrix} = 0 \quad (27)$$

where γ is the amplification factor, $\lambda = \frac{\delta x \gamma}{\gamma - 1}$, $\sigma = \frac{i \sin(\delta y \eta)}{\delta y}$, $\eta \in \left[-\frac{\pi}{\delta y}, \frac{\pi}{\delta y} \right]$, $\kappa = \Gamma + \lambda \Delta$ and $\mu = 1 + i\alpha\lambda$. The six roots of Eq. (27) are

$$\lambda_1 = \lambda_2 = 0 \quad (28)$$

$$\lambda_3 = \lambda_4 = \frac{UR - 2i\alpha}{\sigma^2 - \sigma VR + \Delta R} \quad (29)$$

and

$$\lambda_6, \lambda_6 = \frac{-i\alpha \pm \sqrt{\beta^2 - \sigma^2}}{\sigma^2 - \alpha^2 - \beta^2} \quad (30)$$

The amplification factor associated with λ_6 is given by

$$\gamma_6 = \frac{1}{1 - \delta x \left(\sqrt{\beta^2 + \frac{\sin^2(\eta \delta y)}{\delta y^2}} + \alpha_i \right) + i\alpha_r \delta x} \quad (31)$$

which, again, leads to

$$\delta x_{\min} = \frac{1}{|\alpha_r|} \quad (32)$$

for numerical stability. The minimum step size as given by Eq. (32) implies that a maximum of 2π steps per disturbance wavelength are allowed for the marching. This is consistent with the behavior of the numerical solution first reported by Chang et al. (1991). We should note that, in PSE, we solve for the slow varying shape functions and so this step-size restriction does not cause problems in terms of accuracy; indeed, the numerical examples given in Joslin et al. (1993) show that the PSE solution obtained with 3 steps per wavelength for Tollmien-Schlichting waves in a Blasius boundary layer is in excellent agreement with very accurate direct simulation of Navier-Stokes equations using 60 grid points per TS wavelength.

When step-size smaller than $\delta x_{\min} = 1/|\alpha_r|$ is required for either higher resolution or for the convergence of nonlinear terms in an implicit numerical scheme, a further approximation is sometimes made, i.e., dropping the pressure gradient term $\partial \hat{p} / \partial x$ (see Chang et al. 1991). We point out, however, that most of the physical pressure gradient is absorbed into the term $i\alpha \hat{\phi}$, and that $\partial \hat{p} / \partial x$ is very small in comparison (refer to Eq. 2(c)). After $\partial \hat{p} / \partial x$ is dropped, Eq. (17) can be reduced to a set of 2 equations by eliminating \hat{p} . Carrying out the well-posedness analysis, we obtain two eigenvalues

$$\lambda_1 = -i \left(\alpha + \frac{\eta^2}{\alpha} \right), \quad \lambda_2 = -\frac{C}{D}$$

where C and D are the same as those in Eq. (18). Here, λ_2 gives rise to ill-posedness due to viscosity, which is insignificant as explained before. We note that λ_1 represents ill-posedness if $\alpha_r < 0$ (i.e., for growing waves). Using Eq. (25), we obtain the minimum step-size required for a stable marching scheme,

$$\delta\alpha_{\min} = \max_{\eta} \left[\frac{-2\alpha_i(1 - \eta^2/|\alpha|^2)}{\alpha_r^2(1 + \eta^2/|\alpha|^2)^2 + \alpha_i^2(1 - \eta^2/|\alpha|^2)^2} \right] = \frac{-4\alpha_i|\alpha_r|}{|\alpha| \left[\frac{4\alpha_i^2\alpha_r^2}{|\alpha|^2} + \alpha_r^2 \left(2 + \frac{2|\alpha_r|}{|\alpha|} \right)^2 \right]}$$

In a typical problem, α_i is an order of magnitude smaller than α_r . Therefore,

$$\delta\alpha_{\min} \approx \frac{-\alpha_i}{4|\alpha|} \cdot \frac{1}{|\alpha_r|} + O\left(\frac{\alpha_i^3}{\alpha_r^3}\right) \quad (33)$$

For a problem in which $\alpha_i/|\alpha|$ is small, we see that the restriction on step-size is relaxed by at least an order of magnitude in comparison with Eq. (32).

4. Application to Blasius Boundary Layer

The above analysis was simplified in that the mean flow (U, V) was considered constant. We now apply the results of the above analysis to a realistic problem, i.e., the boundary-layer flow on a flat-plate. The mean flow in this case is governed by the Blasius equation

$$\frac{d^3 f}{d\xi^3} + \frac{1}{2} f \frac{d^2 f}{d\xi^2} = 0$$

$$f(0) = f'(0) = 0; \quad f'(\xi) \rightarrow 1 \quad \text{as} \quad \xi \rightarrow \infty.$$

$$U = f'$$

$$V = \frac{1}{2} \sqrt{\frac{\nu U_e}{x_0}} \left(\xi \frac{df}{d\xi} - f \right)$$

where ν is the kinematic viscosity, U_e the boundary-layer edge velocity and ξ the similarity variable

$$\xi = y_0 \sqrt{\frac{U_e}{\nu x_0}},$$

and x_0 and y_0 being the dimensional values of x and y .

The Blasius boundary-layer is subject to Tollmien-Schlichting (TS) instability. We consider a disturbance of fixed frequency $F = 0.7 \times 10^{-4}$ where

$$F = \frac{2\pi\nu}{U_e^2} \bar{f}$$

\bar{f} being the dimensional frequency. For this disturbance, the initial wavenumber at $R = 500$ is $\alpha_r = .106$. As the wave travels downstream, the wavenumber gradually changes to approximately $\alpha_r = .103$.

Calculations were started at $R = U_e L / \nu = 500$, where $L = \sqrt{\nu x_0 / U_e}$. According to Eq. (32), the minimum step-size is $\Delta x_{\min} \approx 9.5$ based upon the length scale at $R = 500$. The fourth-order accurate compact difference scheme of Malik et al. (1982) was used for wall normal discretization and one step backward Euler discretization was employed in the streamwise direction. We ran our PSE code with $\partial \hat{p} / \partial x$ term included and $\Delta x = 11$ (greater than Δx_{\min}). The growth rate plotted in Figure 2(a) shows a smooth solution. The growth rate in this figure has been made nondimensional with local length scale which varies with x ; however, a constant length scale was used in the marching computations. Next we use $\Delta x = 8$ (smaller than Δx_{\min}), the solution blows up shortly after the marching starts. Now, we drop $\partial \hat{p} / \partial x$ and further reduce the step-size to 5, a smooth solution is again obtained. These calculations confirm the estimate for the minimum step-size and show that the dropping of $\partial \hat{p} / \partial x$ relaxed the step-size restriction. We present additional calculations in Figure 2(b) where $\Delta x = 10$ is used with $\partial \hat{p} / \partial x \neq 0$ and the solution is smooth. However, with $\Delta x = 9$, the solution blows up towards the end of the computation. This shows that the stability condition derived in the previous section provides a remarkably good prediction of the behavior of the PSE solution. With $\partial \hat{p} / \partial x = 0$, stable solution can be obtained for smaller Δx . The comparison of the solution with $\Delta x = 5$ and 10 shows that the approximation $\partial \hat{p} / \partial x = 0$ does not introduce any error, at least in this case.

Figure 3 shows the growth rate results for the same frequency disturbance and $\partial \hat{p} / \partial x = 0$. Three different step sizes were chosen: $\Delta x = .3, .25$ and $.2$. With $\Delta x = .3$, the solution is generally smooth but appears to develop some very slight wiggles near the end. However, with $\Delta x = .25$ and $.2$ solution blows up. The numerical instability occurs earlier for the smaller step size.

The $\Delta x = .2$ calculation is repeated with $i\alpha/R$ dropped to eliminate elliptic effect due to viscosity. The behavior of the solution is unaffected. This indicates that these oscillations are not caused by ellipticity due to the viscous terms. Finally, we eliminate the iteration for α , and do the calculation with fixed real α (the value at $R = 500$). The growth rate shown in Figure 3 is inaccurate, but the growth rate curve is smooth. This suggests that the oscillations may have been caused by the nonlinear iterative process for determination of α . However, one cannot be absolutely sure in view of the stability condition (33). For the present case of $(-\alpha_i)_{\max} \approx .0055$ and $\alpha_r \approx .1$, it follows from (33) that $\Delta x_{\min} \approx .13$ which is not far from the value of $.25$ or $.2$ used in Figs. 3(b) and (c), respectively. The fact that smooth solution was obtained in Fig. 3(c) with α fixed does not necessarily suggest that (33) is not operative since real (α) was used and with $\alpha_i = 0$ Eq. (33) gives $\Delta x_{\min} \approx 0$.

In order to clarify whether (33) is operative, we perform additional computations and report the results in Fig. 3(d) which contains the correct solution from Fig. 2(a) as well as the smooth solution from Fig. 3(c) with $\alpha_i = 0$ and $\Delta x = .2$. Also included are solutions using fixed $\alpha = .104 - i .001$ and $\alpha = .104 - i .004$ (\hat{p}_x and $i\alpha/R$ have been dropped). Equation (33) for $\alpha_i = 0$, $\alpha_i = -.001$ and $-.004$ yield minimum step size of 0, $.023$ and $.092$, respectively. In the first two cases, the step size of

$\Delta x = .2$ used in the computation is much larger than the critical value given by (33) and therefore the solution is smooth. Since initially the value of α_i is close to the correct solution given by (4b), the computed growth rate is close to the correct growth rate. However, further downstream the computed growth rate is in error since (4b) is not satisfied. With $\alpha_i = -.004$, the computational step size is not very far from the critical value and, therefore, solution becomes oscillatory and eventually blows up. In this case, since initially $\alpha_i = -.004$ is not close to the solution of (4b) the growth rate is in error at small Reynolds numbers. However, as the correct growth rate approaches the value of $-.004$, the solution with $\Delta x = .2$ and without imposition of (4b) approaches the correct solution even though it is oscillatory due to the numerical instability. This example clearly suggests that numerical instability observed with $\Delta x = .2$ is associated with the condition given by (33).

We point out that the values of $\Delta x = .3$ and $.2$ correspond to about 200 to 300 marching steps per TS wavelength. Clearly, in no linear or nonlinear applications one needs to take such a small step and, therefore, Eq. (33) is of no significance for most practical computations.

5. Conclusions

The mathematical nature of parabolized stability equations (PSE) is studied. It is shown that the primitive variable formulation is mathematically ill-posed due to the pressure-gradient term. The condition for the stable marching solution is derived. Examples from the linear stability of two-dimensional Blasius boundary-layer are given to show that this condition gives reasonable estimates of the numerical behavior of the parabolized equations. The results also show that the ellipticity associated with the viscous term is insignificant.

References

- Bertolotti, F. P., Herbert, Th. and Spalart, P. R., 1992 "Linear and Nonlinear Stability of the Blasius Boundary Layer," *J. Fluid Mech.*, Vol. 242, pp. 441-474.
- Chang, C.-L., Malik, M. R., Erlebacher, G. and Hussaini, M. Y., 1991 "Compressible Stability of Growing Boundary Layers Using Parabolized Stability Equations," AIAA Paper 91-1636.
- Fasel, H. F. and Konzelmann, U., 1990 "Non-parallel Stability of a Flat Plate Boundary Layer using the Complete Navier-Stokes Equations," *J. Fluid Mech.*, Vol. 221, pp. 311-347.
- Gaster, M., 1974 "On the Effects of Boundary Layer Growth on Flow Stability," *J. Fluid Mech.*, Vol. 66, pp. 465-480.
- Golub, G. H. and VanLoan, C. F., 1983 "Matrix Computations," The Johns Hopkins University Press, pp. 200.
- Herbert, Th., 1991 "Boundary-Layer Transition -- Analysis and Prediction Revisited," AIAA Paper 91-0737.

Joslin, R. D., Streett, C. L., and Chang, C.-I., 1992 "3-D Incompressible Spatial Direct Numerical Simulation Code Validation Study — A Comparison with Linear Stability & Parabolic Stability Equation Theories for Boundary-Layer Transition on a Flat Plate," NASA TP-3205.

Kreiss, H.-O. and Lorenz, J., 1989 "Initial-Boundary Value Problems and the Navier-Stokes Equations," Academic Press.

Malik, M. R., Chuang, S., and Hussaini, M. Y., 1982 "Accurate Numerical Solution of Compressible Stability Equations," *ZAMP*, Vol. 33, pp. 189-201.

Rubin, S. G., 1981 "A Review of Marching Procedures for Parabolized Navier-Stokes Equations," *Proceedings of Symposium on Numerical and Physical Aspects of Aerodynamic Flows*, Springer-Verlag, New York, pp. 171-186.

Saric, W. S. and Nayfeh, A. H., 1975 "Non-Parallel Stability of Boundary Layer Flows," *Phys. Fluids*, Vol. 18, pp. 945-950.

Appendix I

$$L_0 = \begin{bmatrix} \Delta + U_x & U_y & 0 & i\alpha \\ V_x & \Delta + V_y & 0 & 0 \\ W_x & W_y & \Delta & i\beta \\ i\alpha & 0 & i\beta & 0 \end{bmatrix}$$

$$L_1 = \begin{bmatrix} D & 0 & 0 & 1 \\ 0 & D & 0 & 0 \\ 0 & 0 & D & 0 \\ 1 & 0 & 0 & 0 \end{bmatrix}$$

$$L_2 = \begin{bmatrix} V & 0 & 0 & 0 \\ 0 & V & 0 & 1 \\ 0 & 0 & V & 0 \\ 0 & 1 & 0 & 0 \end{bmatrix}$$

$$L_3 = \begin{bmatrix} -\frac{1}{R} & 0 & 0 & 0 \\ 0 & -\frac{1}{R} & 0 & 0 \\ 0 & 0 & -\frac{1}{R} & 0 \\ 0 & 0 & 0 & 0 \end{bmatrix}$$

where

$$\Delta = -i\omega + i\alpha U + i\beta W + \frac{\alpha^2 + \beta^2 - i\frac{d\alpha}{dx}}{R}$$

and

$$D = U - \frac{2i\alpha}{R}$$

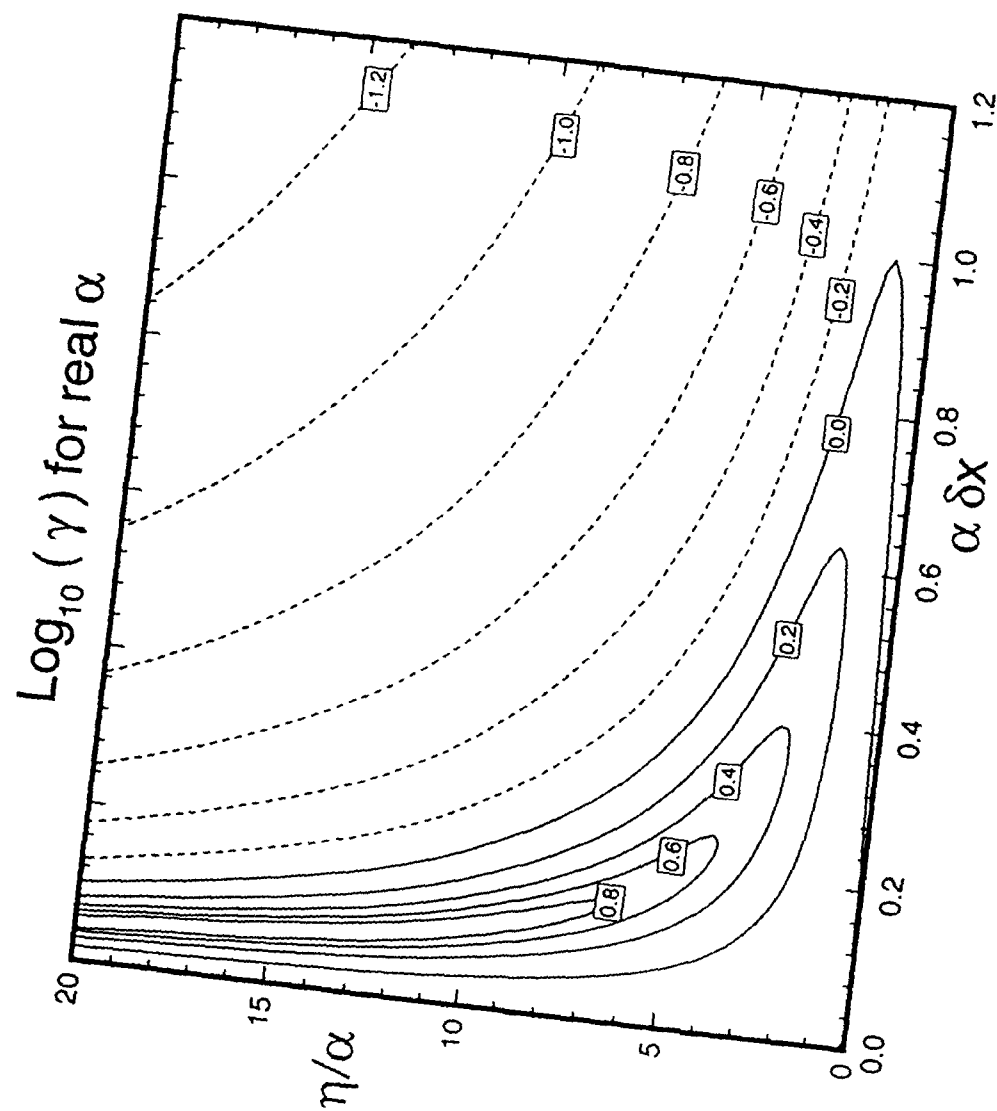


Figure 1. Logarithm of the amplification factor γ for real α . Solid lines represent numerical instability.

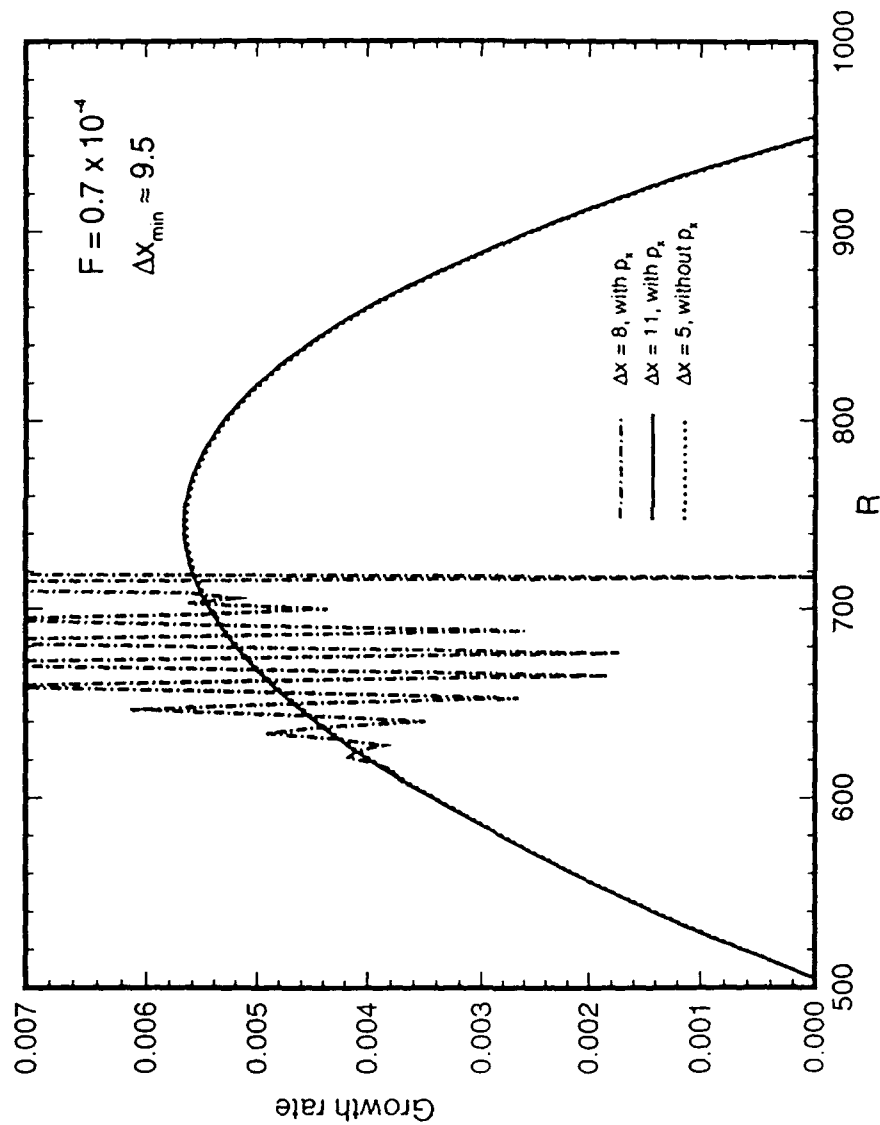


Fig. 2(a). Effect of marching step size on the growth rate of the TS disturbance of frequency $F = .7 \times 10^{-4}$. The critical step size for stable solution is $\Delta x \approx 9.5$.

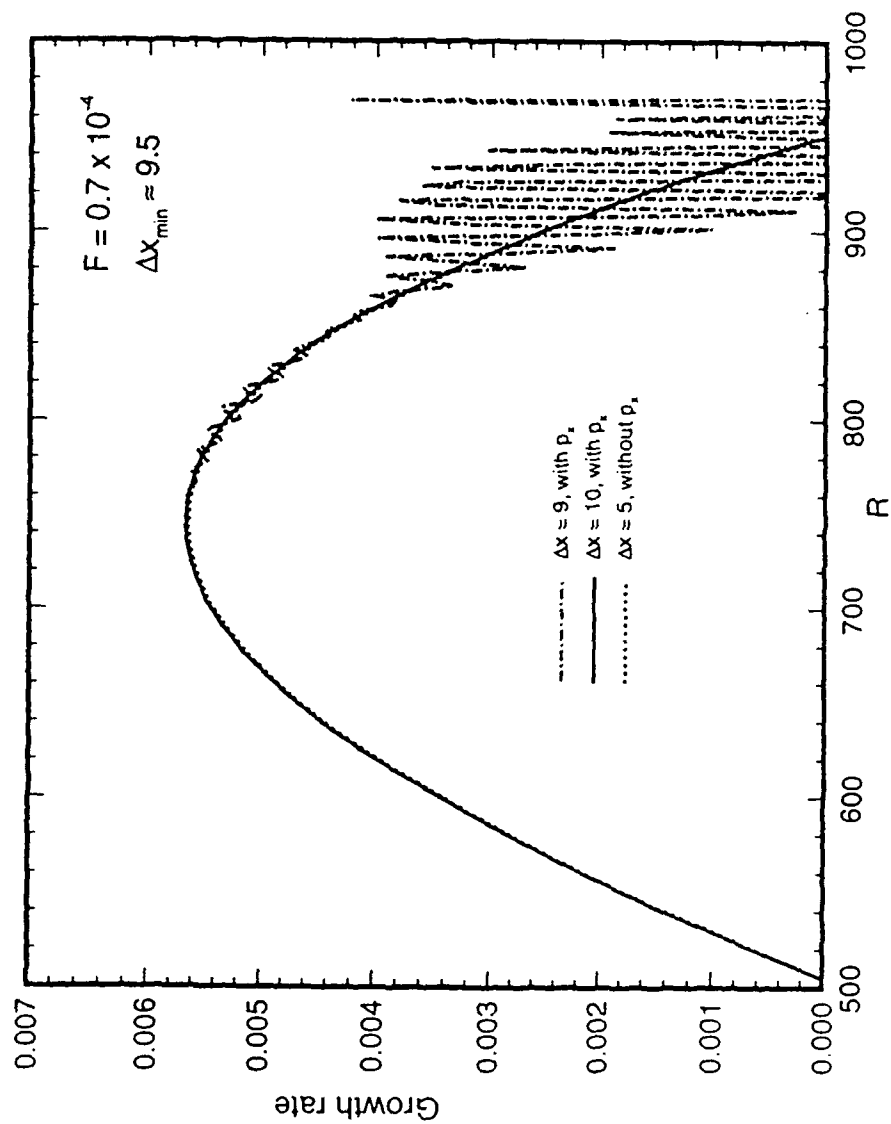


Fig. 2(b). Concluded.

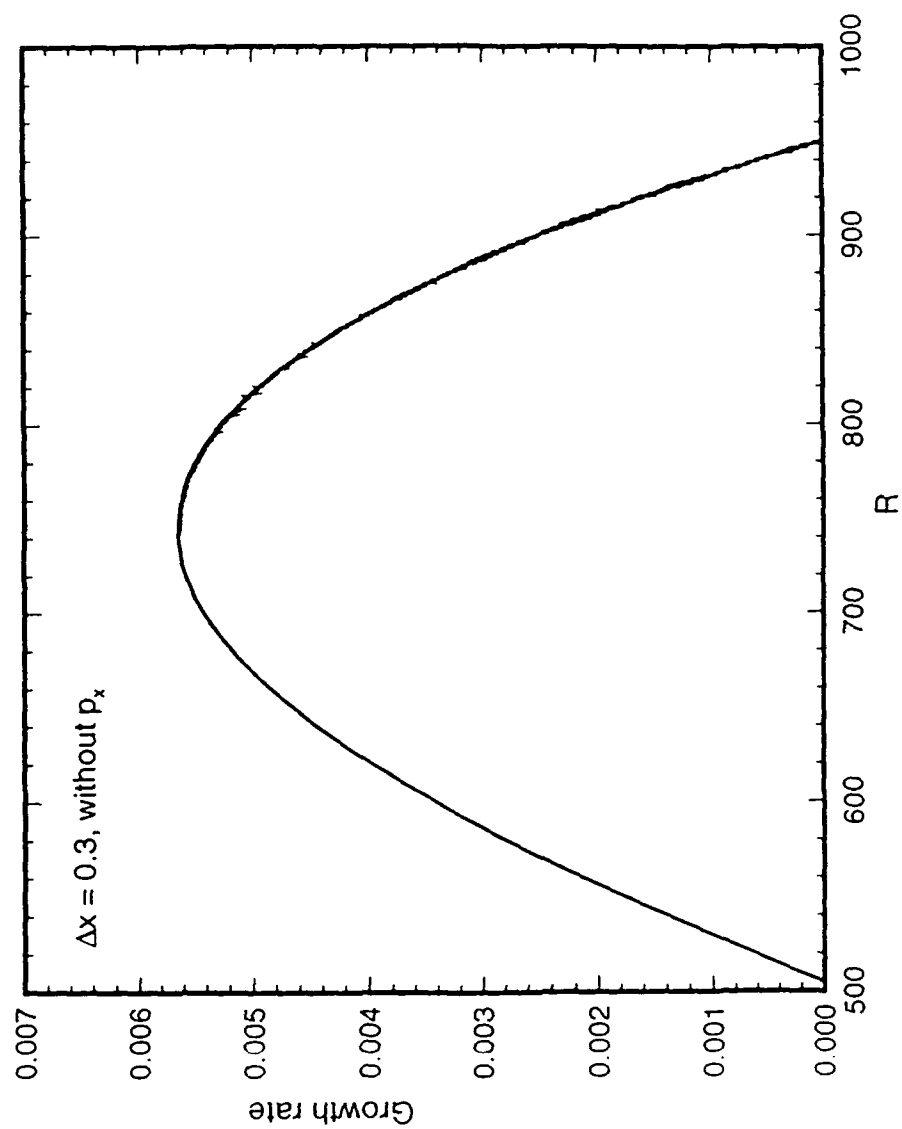


Fig. 3(a). Effect of step size on the growth rate of the TS disturbance ($F = 7 \times 10^{-4}$) with $\partial \bar{p} / \partial x = 0$.

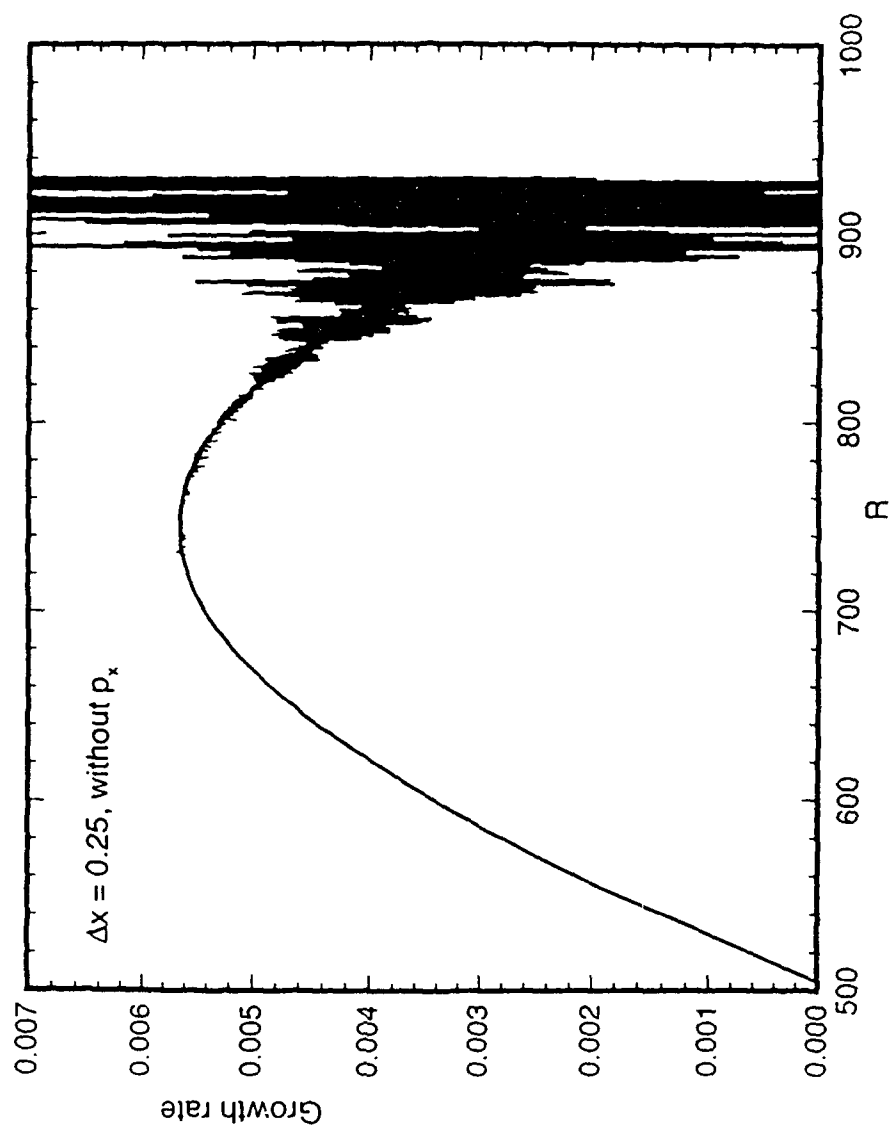


Fig. 3(b). Continued.

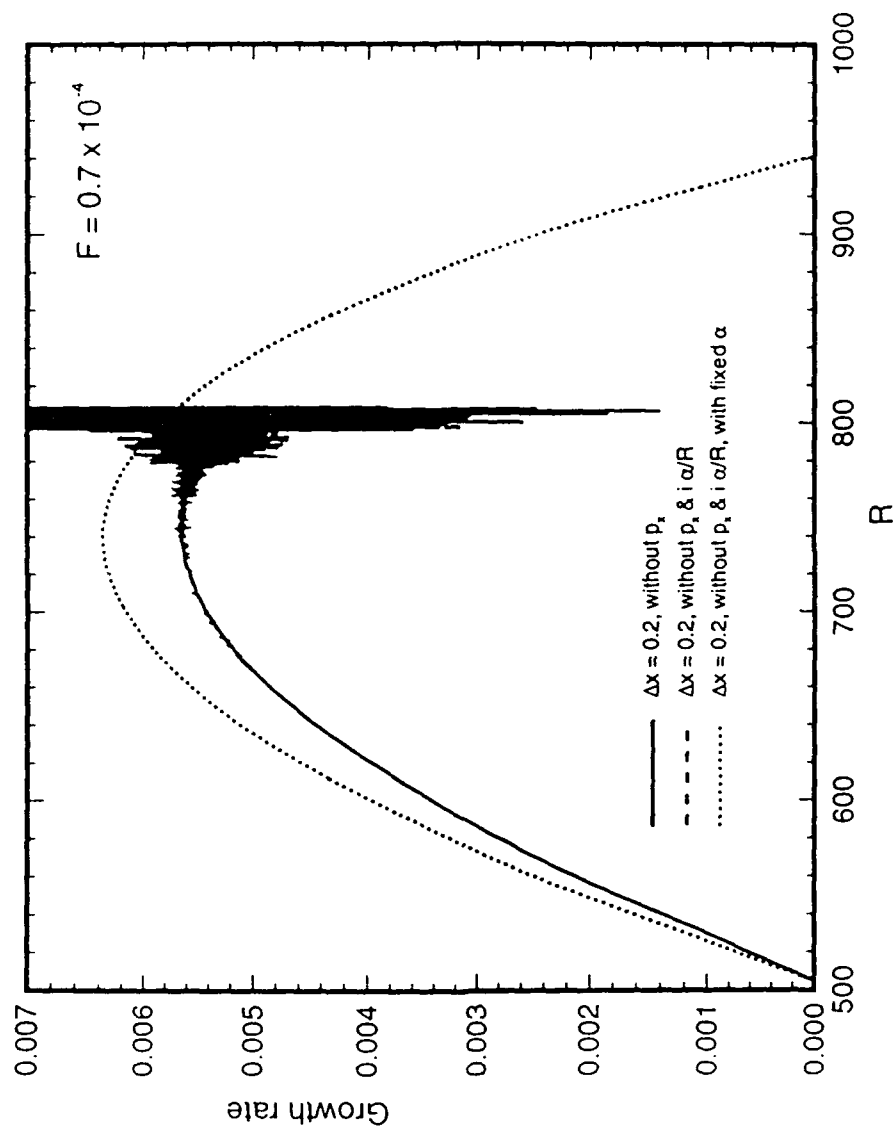


Fig. 3(c). Continued.

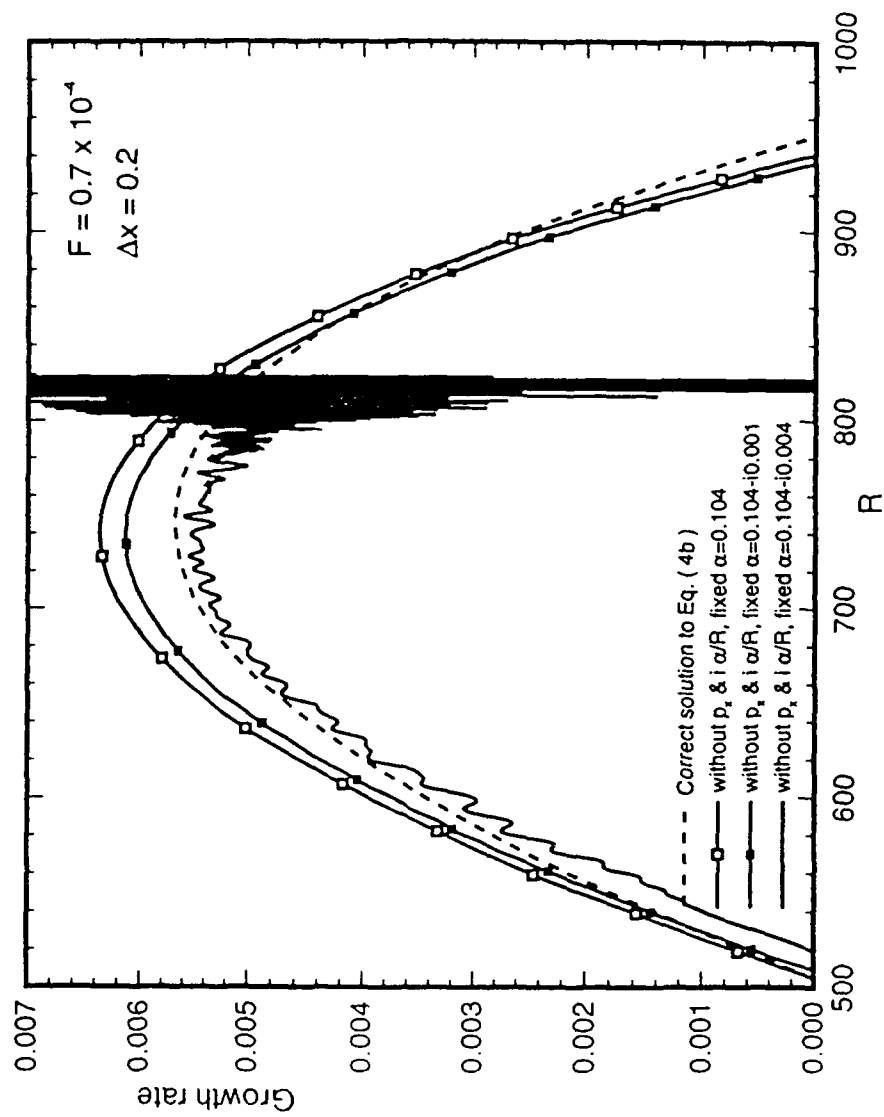


Fig. 3(d). Concluded.